PREVENTING FUEL FAILURE FOR A BEYOND DESIGN BASIS ACCIDENT IN A FLUORIDE SALT COOLED HIGH TEMPERATURE REACTOR

By
Matthew J. Minck
B.S., Mechanical Engineering (2006)
United States Naval Academy

SUBMITTED TO THE DEPARTMENT OF NUCLEAR SCIENCE
AND ENGINEERING
IN PARTIAL FULFILLMENT OF THE REQUIREMENTS FOR THE DEGREE OF

MASTER OF SCIENCE IN NUCLEAR SCIENCE AND ENGINEERING
AT THE
MASSACHUSETTS INSTITUTE OF TECHNOLOGY

SEPTEMBER 2013

Signature of Author: _____
Matthew J. Minck
Department of Nuclear Science and Engineering
20 August 2013

Certified by: _____
Dr. Charles Forsberg
Senior Research Scientist
Thesis Supervisor

Certified by: _____
Dr. Michael Driscoll
Professor Emeritus of Nuclear Engineering
Thesis Reader

Accepted by: _____
Dr. Mujid Kazimi
TEPCO Professor of Nuclear Engineering
Chair, Department Committee on Graduate Students

PREVENTING FUEL FAILURE FOR A BEYOND DESIGN BASIS ACCIDENT IN A FLUORIDE SALT COOLED HIGH TEMPERATURE REACTOR

by

Matthew J. Minck

Submitted to the Department of Nuclear Science and Engineering
on August 20, 2013 in Partial Fulfillment of the Requirements
for the Degree of Master of Science in Nuclear Science and Engineering

ABSTRACT

The fluoride salt-cooled high-temperature reactor (FHR) combines high-temperature coated-particle fuel with a high-temperature salt coolant for a reactor with unique market and safety characteristics. This combination can eliminate large-scale radionuclide releases by avoiding major fuel failure during a catastrophic Beyond Design Basis Accident (BDBA).

The high-temperature core contains liquid salt coolant surrounded by a liquid salt buffer; these salts limit core heatup while decay heat drops. The vessel insulation is designed to fail during a BDBA. The silo contains a frozen BDBA salt designed to melt and surround the reactor vessel during a major accident to accelerate heat transfer from the vessel. These features provide the required temperature gradient to drive decay heat from core to the vessel wall and to the environment below fuel failure temperatures.

A 1047 MW_{th} FHR was modeled using the STAR-CCM+ computational fluid dynamics package. Peak temperatures and heat transfer phenomena were calculated, focusing on feasibility of melting the BDBA salt that improves heat transfer from vessel to silo. A simplified wavelength-independent radiation model was examined to approximate the heat transfer capability with radiation heat transfer.

The FHR BDBA system kept peak temperatures below the fuel failure point in all cases. Reducing the reactor vessel–silo gap size minimized the time to melt the BDBA salt. Radiation heat transfer is a dominant factor in the high-temperature accident sequence. It keeps peak fuel temperatures hundreds of degrees lower than with convection and conduction only; it makes higher core powers feasible.

The FHR's atmospheric pressure design allows a thin reactor vessel, ensuring the high accident temperatures reach the vessel's outer surface, creating a large temperature difference from the vessel to the frozen salt. This greatly accelerates the heat transfer over current reactor designs with thick, relatively cool accident outer vessel temperatures. The frozen BDBA salt in the FHR places a limit on the upper temperature at the vessel outer boundary for significant time; it is a substantial heat sink for the accident duration. Finally, surrounding the FHR vessel, the convection of hot air, and circulating salt later in the accident, preferentially transports heat upward in the FHR; this provides a conduction path through the concrete silo to the atmosphere above the FHR.

Thesis Supervisor: Charles Forsberg
Title: Senior Research Scientist

Acknowledgements

I would like to thank the US Department of Energy (DOE) Nuclear Energy University Program (NEUP) for their support of this work. Within the Institute, I would like to thank Clare Egan and Heather Barry for their support while I was a student in the Nuclear Science and Engineering Department. Professor Baglietto provided invaluable instruction and patient counseling for my comprehension of many aspects of fluid dynamics and heat transfer. I would also like to thank Professor Kazimi for his instruction in engineering aspects of nuclear systems as well as structural mechanics and Dr. Michael Short for his guidance on test reactor design, vessel materials, and curie point phenomena. Finally, thank you Professor Forsberg and Professor Driscoll for your patience, wisdom, and guidance, all of which was invaluable.

Contents

ABSTRACT 3

Acknowledgements 5

1 Introduction 15
- 1.1 System Description . . . 16
- 1.2 Initiating Events . . . 17
- 1.3 Vessel Insulation Failure . . . 17
- 1.4 Silo Cooling System: First Accident Stop Point . . . 18
- 1.5 Silo Cooling System Failure . . . 19
- 1.6 Transfer of Decay Heat through the Silo . . . 20
- 1.7 Transfer of Decay Heat to Atmosphere . . . 20
- 1.8 Summary . . . 21

2 Salt Selection 22
- 2.1 Melting Point . . . 24
- 2.2 Heat Capacity . . . 25
- 2.3 Chemical Properties . . . 25
- 2.4 Salts Modeled . . . 26

3 Vessel and Silo Design 28
- 3.1 FHR Dimensions . . . 28
- 3.2 Vessel Material . . . 29
- 3.3 FHR Vessel Analysis . . . 33
- 3.4 General Pressure Vessel Design . . . 36

4 Silo Cooling System 40

5 Insulation Failure 42
- 5.1 Mirror Insulation . . . 43
- 5.2 Melting Point Insulation . . . 45

5.3 Fall-away Insulation 46
5.3.1 Curie-Point Magnetic Insulation 46
5.3.2 Fusible Link Insulation 47
5.3.3 Dynamic Property Insulation 48
5.4 Summary 49

6 Parts and Geometry Models **51**
6.1 FHR BDBA System Overall Geometry 51
6.2 Core Model 54
6.2.1 Core Power 55
6.3 BDBA Air Cavity 58
6.4 BDBA Salt Two-Phase Model 59
6.5 BDBA System Reduced Geometry 61
6.6 BDBA System Outer Elements 62

7 Initial Conditions **67**
7.1 Heat Input Boundary Condition 67
7.2 Maximum Salt Temperature Boundary Condition 70
7.3 Initiating FLiNaK Circulating Flow in the Air Cavity 71
7.4 Expected Temperatures and Pressure in the System 71

8 Physics Models **74**
8.1 Time Step and Unsteady Solver 74
8.1.1 Implicit Unsteady Modeling 75
8.1.2 Time Stepping and Inner Iterations 77
8.1.3 Coupled and Segregated Models 78
8.2 Capturing Thermophysical Property Variations 78
8.2.1 Turbulence 82
8.3 Buoyancy 83

9 Results: Base Case **85**
9.1 System Temperatures 92
9.2 Heat Transfer Outside the FHR Vessel 96
9.3 Maximum Temperatures and Energy Transfer 97
9.4 Validating the Solution 100

10 Effect of Reducing the Air Cavity Annular Gap **101**
10.1 Reduced Annular Gap Model 101
10.2 System Temperatures 104
10.3 Convective Currents 106
10.4 Total Energy Input and Circulating Salt 107

11 Radiation **113**
11.1 Thermal Radiation Model . . . 115
11.1.1 Gray Thermal Radiation Model . . . 115
11.2 Surface-to-Surface (S2S) Radiation Model . . . 116
11.2.1 Radiation Modeling with View Factors . . . 117
11.2.2 Modeling with the View Factors Model . . . 119
11.3 FHR Base Case with Radiation . . . 120
11.4 Optimizing Emissivity . . . 126
11.5 Limitations of Modeling with Radiation . . . 131

12 Sources of Error and Uncertainty **132**
12.1 Vessel Design . . . 132
12.2 Core Design . . . 133
12.3 Volumetric heat source/heat fluxes imposed . . . 134
12.4 Turbulence modeling . . . 134
12.4.1 High Rayleigh Number Convective Turbulence . . . 134
12.5 Salt Melting . . . 135
12.6 Radiation . . . 136

13 Conclusions **137**
13.1 Liquid Heat Sink . . . 137
13.2 Vessel Wall Temperature . . . 138
13.3 Radiation . . . 138
13.4 BDBA Heat Sink . . . 140
13.5 Upward Heat Transport to Atmosphere . . . 141
13.6 Concrete Temperatures and Behavior . . . 142
13.7 Design Space . . . 142

14 Future Work **143**
14.1 Radiation Heat Transport . . . 143
14.2 Convective Air Circulation . . . 144
14.3 BDBA Salt Selection . . . 145
14.4 BDBA Salt Melting: Two-Phase Interface Tracking . . . 145
14.5 Concrete Modeling and Selection . . . 146
14.6 Integrated Model . . . 146
14.7 Experimental Validation of Models . . . 146

A Validating the STAR-CCM+ Analysis with No Radiation **148**

B Validating the STAR-CCM+ Conduction Model **156**
B.1 Validating a 1-D Time-Varying Heat Conduction Case . . . 156

C Creating and Validating the Total Energy Input in STAR-CCM+ 163

D FHR Design Space 168
D.1 Silo Thickness . . . 168
D.2 Vessel Thicknesses and Materials . . . 169
D.3 Gas Cavity . . . 169
D.3.1 Size . . . 170
D.3.2 Contents . . . 170
D.4 BDBA Salt . . . 170
D.5 Radiation . . . 171
D.5.1 Emissivity Control . . . 171
D.5.2 Transmissivity of Buffer Salt and Gas . . . 172
D.6 Core . . . 172
D.6.1 Surface to Area Ratio . . . 172
D.6.2 Power Output . . . 173
D.7 Buffer . . . 173
D.7.1 Geometry . . . 173
D.7.2 Fluid . . . 173
D.8 Design Space Conclusions . . . 174

List of Figures

1.1 Beyond Design Basis Accident (BDBA) system. 16

2.1 Cylindrically Symmetric BDBA Heat Removal System Schematic. 23

3.1 FHR Alternative Designs. 28
3.2 FHR Loop Design. 29
3.3 Material Strength vs Temperature. 30
3.4 Vessel Shell Design. 36

4.1 Silo Cooling System. 40

6.1 FHR Geometry Modeling. 52
6.2 STAR-CCM+ Geometry View. 54
6.3 Axial and Radial Power Distribution Plots. 57
6.4 Volumetric Heat Source Distribution. 58
6.5 Reduced Geometry Modeling. 61
6.6 Outer Elements System Model. 63
6.7 Silo and Backfill Temperatures after 2 Months. 64
6.8 Outer FHR Component Temperatures vs Time. 65

7.1 Decay Heat Fraction vs Time. 68
7.2 Volumetric Heat Source Distribution in FHR. 70
7.3 Initial FHR Temperature Schematic. 73

8.1 Core Average Temperature vs Time Step Size. 76
8.2 Residuals for the base FHR Case. 77
8.3 FLiNaK Viscosity. 79

9.1 Base Case Model. 86
9.2 Base Case Average BDBA Salt Temperature vs Time. 87
9.3 Base Case Core and Buffer Temperature Profiles. 88
9.4 Base Case FHR System Temperatures. 89

9.5 Convective Currents in the Core and BDBA Salt. 90
9.6 Air/Vessel Interface Heat Transfer Coefficient. 91
9.7 Base Case System Temperatures vs Time. 92
9.8 Base Case Inner Component Temperatures vs Time Before 78 Hours. 93
9.9 Base Case BDBA Salt Heat Flux. 94
9.10 Base Case Component Temperatures vs Time After 78 Hours. 95
9.11 Base Case Overall System Temperatures vs Time. 96
9.12 Base Case Energy of Fusion Input Into BDBA Salt. 98

10.1 4m Air Cavity Models. 102
10.2 4m Air Cavity BDBA Average Salt Temperature vs Time. 103
10.3 4m Air Cavity Model Overall System Temperatures vs Time. 105
10.4 4m Air Cavity Convective Currents. 106
10.5 4m Air Cavity Heat Transfer Coefficient. 107
10.6 Model of 4m Air Cavity with Circulating Salt Immersing Vessel. 108
10.7 4m Air Cavity Energy of Fusion Into BDBA Salt. 109
10.8 4m Air Cavity After Vessel Immersion. 110
10.9 4m Air Cavity Immersed Vessel Temperature Distribution. 111
10.104m Air Cavity Immersed Vessel Heat Transfer Coefficient. 112

11.1 The View Factor Integral. 117
11.2 BDBA Salt Temperature vs Time with Radiation, $\epsilon = 0.3$. 121
11.3 Radiation Case System Temperatures vs Time. 123
11.4 BDBA System Temperatures at $t = 93375$ seconds (26 hours). 124
11.5 Radiation Effect on BDBA Salt Temperature Profiles. 125
11.6 Higher Emissivity BDBA Salt Temperature vs Time. 127
11.7 Higher Emissivity Overall System Temperatures vs Time. 128
11.8 Higher Emissivity BDBA Salt Energy of Fusion Input. 130

A.1 Convective Interface Boundaries. 151
A.2 BDBA Heat Flux in Base Case. 154

B.1 Temperatures in a Rod of length L [33]. 156
B.2 Temperature Distribution in a Thin Rod vs Position for Varying t. 161
B.3 Positional Temperature Distribution in a Thin Rod. 162

C.1 A 2 meter Cube. 164
C.2 Average Heat Flux and Rate in the $4m^2$ test case. 165
C.3 Total Energy Input for the Test Case. 167

List of Tables

2.1 Requirements of Frozen Salt for a BDBA. 26

3.1 Stainless Steel 316 Composition. 32
3.2 Stainless Steel 316 Properties. 32
3.3 Properties Used in Vessel Analysis. 33
3.4 Thick-Walled Vessel Principal Stresses. 37
3.5 ASME Vessel Design Requirements. 38
3.6 Allowable Stress, 760° C, Stainless Steel 316. 38
3.7 Minimum Design Criteria. 38
3.8 FHR Vessel Dimensions. 39

7.1 Volumetric Heat Source Energy Distribution in the Core. 69

8.1 Difference in 1 and 3 Second Time Steps on Core Temperature. 76
8.2 Properties of FLiNaK Salt. 80
8.3 Flibe Property Field Functions. 82

9.1 Base Case Component Temperatures. 86

10.1 4m Air Cavity Component Temperatures. 103
10.2 Component Temperatures After BDBA Salt Melts. 110

11.1 Component Temperatures with Radiation, $\epsilon = 0.3$. 121
11.2 Higher Emissivity Component Temperatures. 127

13.1 Peak System Temperatures at Critical Times with Varying Phenomena. . . 139

A.1 Surface Areas and Volumes of the Modeled FHR. 148
A.2 Heat Capacity of Salts. 149
A.3 Radii of and Heat Tlux Through FHR Components. 150
A.4 Thermophysical Properties of the FHR Fluids. 152
A.5 Free Convection Nusselt Numbers. 152

Chapter 1

Introduction

The fluoride-salt-cooled high-temperature reactor (FHR) is an advanced reactor that uses graphite-matrix coated-particle fuels (the same fuels used in high-temperature gas-cooled reactors) and low-pressure liquid-salt coolants [7]. The failure temperature of the fuel is 1650° C. The baseline coolant salt is a mixture of ^{7}LiF and BeF_2, more commonly referred to as flibe. The melting point is 460° C and the boiling point is 1433° C. The nominal peak coolant temperature is 700° C. For comparison, the melting point of iron is 1535° C. As long as there is coolant in the core, large-scale fuel failure is not expected to occur. High-temperature vessel failure would be expected to occur before large-scale fuel failure. No other reactor has this characteristic. The combination of (1) fuel properties, (2) coolant properties, and (3) the large temperature difference between the normal operating temperature and the boiling point of the coolant may allow design of a large reactor where there is no large-scale fuel failure even if all decay-heat removal capacity is destroyed and the plant is destroyed. If there is no large-scale fuel failure, there can not be large-scale radionuclide releases. This may be possible by locating the reactor in a specially-constructed silo. In a severe accident that destroys the reactor (but not the fuel), the decay heat is conducted directly to ground while peak temperatures are below the boiling point of the coolant and thus below those that cause large-scale fuel failure.

1.1 System Description

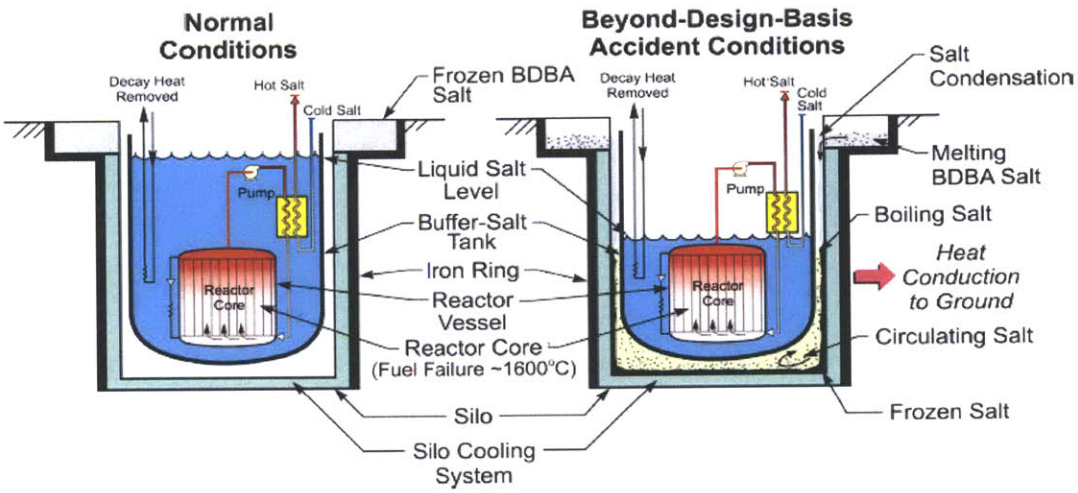

Figure 1.1: Beyond Design Basis Accident (BDBA) system.

The baseline design is a pebble-bed reactor with the reactor vessel and core (Figure 1.1) located in an underground silo. There are several alternative designs. One option has a single vessel and salt. The other option has the primary reactor system inside a larger vessel filled with a low-cost liquid buffer salt that provides a uniform temperature environment for the major reactor components: a mechanism to assure no risk of accidental freezing of the primary salt anywhere in the primary system. In either case the total salt inventory is such that if the vessel fails, the bottom of the silo fills with liquid salt and the final liquid level is above the top of the reactor core. Salt can't leak from the silo because it freezes when in contact with the colder silo wall. There are many alternative BDBA system alternatives. The description herein describes expected general system behavior and some of the design options. This is work in progress and a full model of system behavior does not yet exist.

1.2 Initiating Events

After loss of all decay-heat cooling, the initial event is heatup of the reactor vessel. The FHR has a larger effective thermal inertia per megawatt than a high-temperature gas-cooled reactor (HTGR); consequently, fuel temperatures increase at a slower rate after loss of all cooling. The large thermal inertia is a consequence of (1) the liquid salt circulation and radiation heat transfer through the transparent salt that ensures almost isothermal conditions within the reactor core and vessel and (2) the higher heat capacity of the salt relative to the fuel. The high heat capacity absorbs heat while the decay heat generation rate begins to decrease.

1.3 Vessel Insulation Failure

During normal operations, the vessel temperature is 600° C. The vessel insulation system is designed to minimize heat losses to the silo cooling system during normal operations but designed to fail as the vessel temperature rises. Insulation failure results in massive radiation and convective air heat transfer to the silo structure and may stop the rise of the vessel temperature over time and its subsequent failure. Several thermal insulation systems have been identified that insulate the reactor system at operating temperatures but allow efficient heat conduction to the silo at higher temperatures.

- *Radiation heat transport.* Radiation heat transport becomes significant at about 600° C. For mirror-type insulation, this results in greater heat losses as the temperature increases.
- *Melt Insulation.* The insulation can be designed to melt and flow to the bottom of the silo upon overheating. In solid form, the insulation contains gas spaces that are the primary barrier to heat flow. There are several candidate metals and salts within

the appropriate range of melt temperatures. Once the solid melts, liquid puddles at the bottom of the silo.

- *Fall-away insulation.* In the event of overheating, the insulation falls away so that heat from the reactor vessel can radiate directly to the silo wall. Several mechanisms that allow fall-away insulation are being examined. The insulation can be held in place with temperature-sensitive fusible links, much like the triggering mechanism in fire sprinkler systems. The insulation can be held in place with magnets where if their curie point is exceeded, they become non-magnetic and fail.

As discussed later, in all cases there is a requirement that the insulation allow efficient heat transfer if exposed to hot liquid salt. This can be accomplished by the insulation failing or insulation with appropriate channels to allow salt flow. An example of the latter is mirror insulation made of steel sheets with channels. The channels can be designed to allow liquid salt passage. *In all cases, the design objective is to reduce the temperature drop required to move heat from the reactor core to silo under accident conditions.*

Once the insulation fails, heat is transferred from the hot vessel to the cold silo wall. This is primarily by thermal radiation. Air convective heat transfer is much less important.

1.4 Silo Cooling System: First Accident Stop Point

During normal operations, the cooling system within the silo prevents heat damage to the concrete and equipment in the silo by circulating water via cooling channels in the wall to prevent concrete degradation. Cooling channels are located along the inner radius of the concrete silo. The same system is designed to provide cooling that may stop severe accident progression before vessel failure—depending upon reactor decay heat. The initial assessment is to use water cooling in a system where the temperature is controlled during

normal operation by cooling the water that cools the silo. In a BDBA, the water removes heat by boiling—a totally passive system where steam can be vented and added water can be provided by a passive water tank [6]. The basic design is from silo cooling systems for High Temperature Gas Reactors.

1.5 Silo Cooling System Failure

If the loss of vessel insulation and the silo cooling system are insufficient to stop the accident, the accident progresses to the next level. There are many alternative accident scenarios but all lead to operation of the final BDBA system and melting of a BDBA salt. As temperatures continue to rise, the vessel may fail. If it fails, it contains sufficient molten salt to fill the bottom of the silo with liquid salt while keeping the reactor core flooded. Heat is transferred between the reactor vessel and the silo by circulating salt.

Independent of vessel failure, as temperatures begin to rise in the silo, the heat begins to melt the solid BDBA salt located in standpipes connected to larger storage tanks of dry salt. The BDBA salt is a low cost salt that is thermodynamically stable and chosen such that its melting point is several hundred degrees Celsuis. The leading candidates are mixtures of chloride salts. The salt has two key functions:

1. *Constant Temperature Heat Sink.* The salt initially increases in temperature until the melting point is reached. The temperature then remains constant as the salt melts due to the latent heat of fusion. It provides a constant boundary temperature while decay heat decreases for some time.
2. *Heat Transfer Fluid.* As the BDBA salt melts, the level of molten salt between the vessel and the silo rises; this increases heat transfer to the silo wall by circulating molten salt. There is sufficient BDBA salt in the FHR silo to flood the reactor vessel.

The temperature drop required to move heat from the reactor core to silo is further reduced.

1.6 Transfer of Decay Heat through the Silo

The allowable peak temperature is determined by the fuel failure temperature. There is a fixed allowable total temperature drop from the fuel to the earth. The engineering features of the silo (insulation that fails at high temperature and the BDBA salt) reduce the temperature drop from reactor core to silo wall. This provides the required temperature drop to drive decay heat into the silo wall, through the soil and upper concrete structure, and ultimately to the atmosphere.

The silo concrete is an alumina-based concrete with a high-temperature aggregate (granite or basaltic rock) to retain some strength for limited periods of time at high temperatures. The concrete is designed to minimize gas generation during heatup and contains channels to allow steam escape. There is the option to include added cooling in the silo and surrounding soil by addition of devices such as heat pipes. Such devices have high reliability but the incorporation of such systems within the concrete or surrounding soil requires careful thought about how to demonstrate performance and conduct repairs if required sometime in the future.

1.7 Transfer of Decay Heat to Atmosphere

Heat is transferred via two routes. First, the circulating air and/or molten BDBA salt in the air cavity outside the vessel results in higher temperatures at the top of silo. This aids heat transport via conduction through the silo cover to the atmosphere—the ultimate heat sink.

Second, the backfill system exists outside the silo wall; it transports heat from the silo wall to the atmosphere via conduction. Thermal conductivity of the soil can be increased through the inclusion of specific backfill materials with favorable heat transfer properties such as graphite bars; this is likely to be a second-order effect.

1.8 Summary

The FHR has the unique combination of a high-temperature fuel, a high-temperature liquid coolant with a boiling point substantially above reactor vessel failure temperatures, and a large temperature margin between operating temperatures and the coolant boiling point. That combination provides nearly 1000° C to drive decay heat in a BDBA from the reactor vessel to the atmosphere. The initial assessment is that with appropriate choice of materials from the reactor vessel through the silo, it may be possible to prevent major fuel failure (thus no major radionuclide release) with a large reactor of over one thousand megawatts thermal even if all conventional decay heat removal systems fail and there are large-scale structural failures.

Significant work remains to determine if an economic fail-safe system can be designed to eliminate the potential for large-scale nuclear reactor accidents in large FHRs. This is the first analysis of this system using analytical and numerical methods to understand system behavior–what phenomena and design parameters are important and what are not as important. It must be followed by design studies to begin to optimize and create an economical design.

Chapter 2

Salt Selection

Under normal conditions, the frozen salt has no function. The salt is only functional under BDBA conditions where it serves primarily as a heat sink as it melts and then as a circulating fluid to move heat away from the reactor vessel to the silo wall so that the fuel does not reach failure temperature. Initial designs place a very large reservoir at the top of the reactor silo as in Figure 1.1. The analysis of this report shows that the maximum heat transfer to the outer elements of the BDBA system (silo concrete and the surrounding backfill) will occur if the BDBA salt is inserted as a part of the reactor structure between the steel liner and the reactor silo as in Figure 2.1.

Considerable research has been performed in the past with salt-based coolants. Most notable research arose from the molten salt reactor experiment of the the 1960s at Oak Ridge National Laboratory. In that reactor, the fuel was dissolved in the salt [8]. With the current focus on Generation IV nuclear power plants, recent studies at Oak Ridge National Lab have reviewed the properties of various salts to be used in different applications within the plant.

Many fluoride-based salts have been examined in detail since the late 1950s. Significant

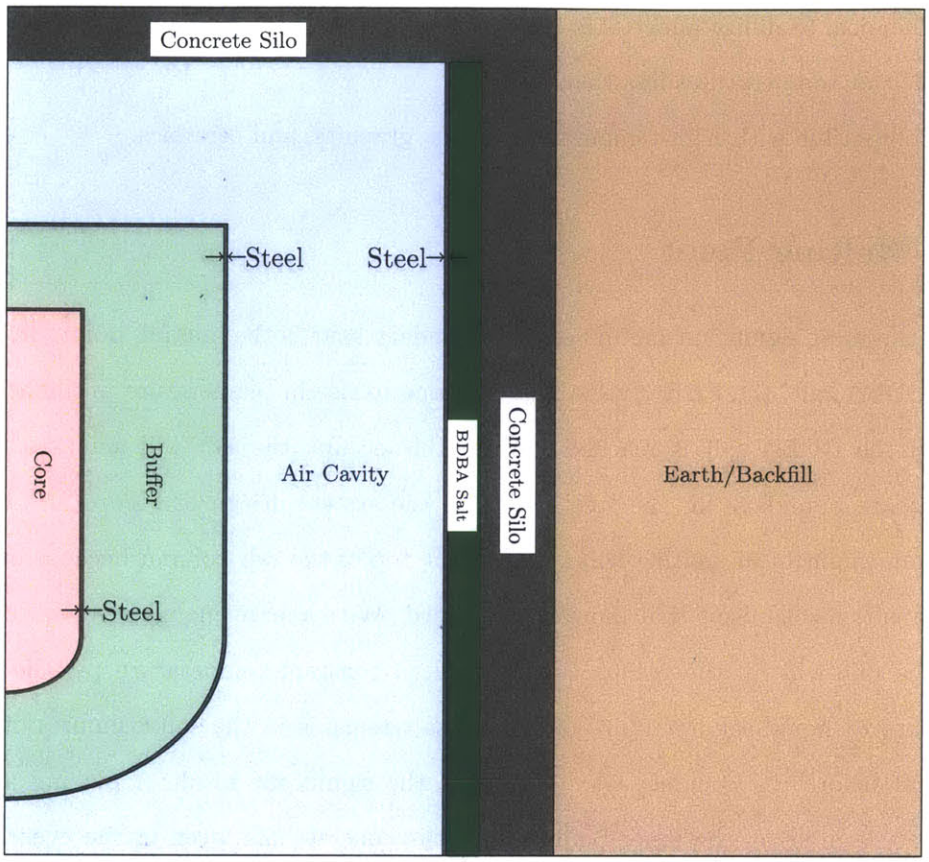

Figure 2.1: Cylindrically Symmetric BDBA Heat Removal System Schematic.

differences in the FHR concept include high temperature operation of the salt (i.e. 700–800° C or higher) and the use of "clean" salts; that is, there is no fuel dissolved into the salts as in prior research. Furthermore, different parts of the FHR will see different characteristics–for instance, the primary coolant will see significant neutron flux while the BDBA salt opposite the insulation and steel lining and vessel of the reactor will see limited neutron flux. This should significantly open the available options for BDBA salt selection.

Regardless of which salt is chosen, a few of the criteria are mandatory for overall FHR success [30]:

- Chemical Stability above 800° C.
- Melt at temperatures less than 525° C.
- Compatible with high-temperature alloys, graphite, and ceramics.

2.1 Melting Point

One of the most significant factors of the secondary salts is the melting point. In the case of the BDBA salt, the FHR system will continue to rise in temperature until the melting point of the BDBA salt is reached. When this occurs, the salt will act as a constant temperature boundary for the steel liner. In the system design of Figure 2.1, the most significant quantity of melting will occur at the top of the salt column because of various heat transfer mechanisms that move heat upward. With a large enough reservoir of BDBA salt, this salt will fill the reactor cavity while a constant temperature (at the liquidus temperature) liquid-solid mixture of BDBA salt remains in the salt column outside the liner and before the concrete silo. This has the significant result of placing an upper temperature limit on the inner boundary of the concrete silo, even in the event of total (including passive) silo-cooling failure.

The desired melting point temperature of the BDBA salt must be a compromise between desired structural integrity under normal operations and keeping the beyond design basis accident scenario maximum system temperatures as low as possible. If the BDBA salt melts at too low a temperature, it could melt and in theory leak from the silo. The higher melting point implies that when it reaches a cooler location, it freezes. It is a self-sealing system to assure no salt loss. It also prevents localized overheating events from triggering system operation. However, with a high melting point temperature, it will take longer for the BDBA salt to begin melting with higher fuel and reactor vessel temperatures before full system activation, the concrete will reach a higher temperature in an accident, and, once

the BDBA salt melts and fills the reactor cavity, the circulating liquid will be at higher temperatures during the accident.

2.2 Heat Capacity

Recall that the product of density and specific heat capacity of any material is called volumetric heat capacity and measures the ability of a material to store thermal energy. When combined with the thermal conductivity, k, of a substance, a material can be evaluated based on a property termed the thermal diffusivity, α:

$$\alpha = \frac{k}{\rho c_p}$$

This property determines the ability of any material to conduct thermal energy against its ability to store thermal energy. Salts, with large densities and specific heat capacities in addition to low thermal conductivities, make an excellent material not only for the BDBA salt but also the buffer salt since, with their low α value, they will respond to thermal environments slowly. This concept is termed *thermal inertia* and will limit the severity of the accident since the salt solutions will absorb heat as the decay heat exponentially decays following the onset of the accident scenario. Though salts in general are characterized by having low thermal diffusivity, finding a salt with lower thermal diffusivity will serve to limit peak temperatures post-accident.

2.3 Chemical Properties

Chemical stability with the material and atmospheric environment, corrosion control, and degradation properties must be taken into account for the salts of the FHR. Research is currently examining the effects of materials corrosion in a salt-based environment and the

Requirement	Ideal Data	Explanation
Minimum T_{melt}	300–500°C	Freezes upon contact with silo wall
Minimum T_{boil}	1200 °C	Below $T_{fuel\ failure}$
High Heat Capacity	$\geq$ 800 kJ/MT-K	Absorbs large amounts of heat before boiling
Inorganic		Less likely to decompose at high temperatures
Toxicity		Avoid creating additional hazard in incident
Neutron Absorption		Aids in reactor shutdown
Fission Product Solubility		Prevents release of fission products
Minimal High-Temperature Decomposition		Prevents release of gas and formation of other products
Compatibility with Reactor Coolant and Buffer Salt		Does not generate heat or gas
Compatibility with Construction Materials		Does not promote equipment failure
Low Cost		Avoid quantity constraint

Table 2.1: Requirements of Frozen Salt for a BDBA.

introduction of impurities. The database of corrosion tests in high temperature radiation environments is currently limited [30], but it will be a significant factor in the selection of FHR salt employment.

A chart summarizing the desirable characteristics of BDBA salt is listed in Table 2.1.

2.4 Salts Modeled

Based on the salt research available, both the buffer salt and BDBA salt modeled in this research were the LiF-NaF-KF eutectic composition, commonly referred to as FLiNaK. It ranks high among the salt compositions for heat transfer properties that were researched. Furthermore, work at Oak Ridge National Laboratory indicates that temperatures of near 900° C may be achievable with acceptable corrosion rates for Fluoride-based salts with good purification system engineering. The downside to Fluoride-based salts is that their cost is much higher than that of Chloride–based salts. The properties are sufficiently similar that major conclusions are not expected to change base on specific salt selection. However,

research with Chloride–based salts has not yet matured for BDBA salt selection [30].

Chapter 3

Vessel and Silo Design

3.1 FHR Dimensions

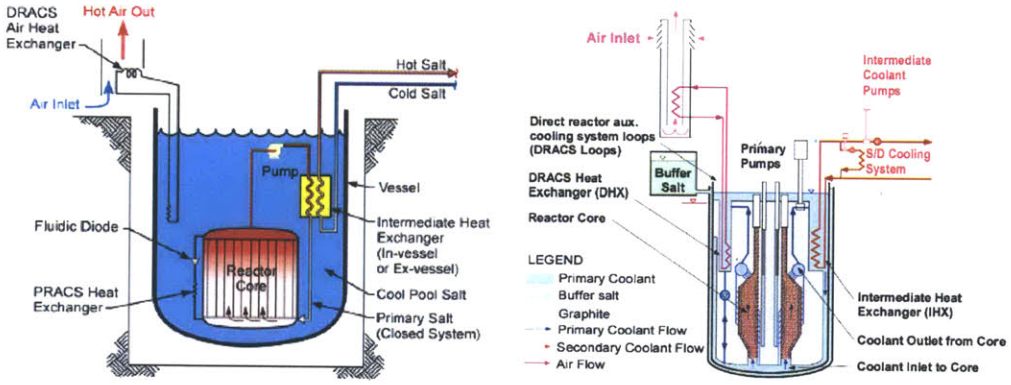

(a) FHR Vessel

(b) Alternative Vessel Configuration

Figure 3.1: FHR Alternative Designs [7].

The vessel analyzed for this report is based on the University of California-Berkeley (UCB) initial design [7, Apdx. I]. Since the FHR is a new reactor concept, there has been limited vessel analysis to date. UCB is a partner in this FHR project; they have provided

a baseline design. The fuel geometry is based on the South African Pebble Bed Modular Reactor (PBMR).

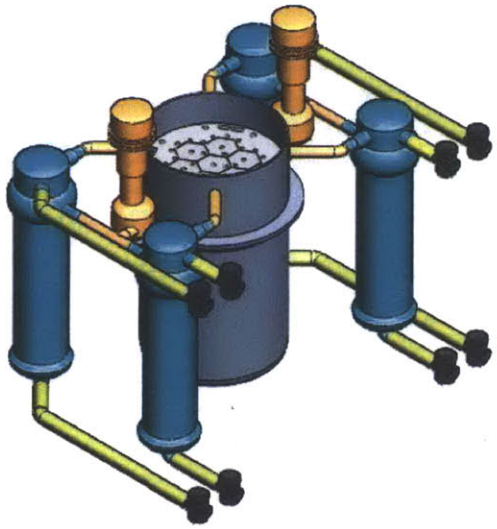

Figure 3.2: FHR Loop Design [7]

The primary loop consists of two salt pumps that drive the primary salt coolant through the reactor core. The flibe salt leaves the core and transfers heat with the secondary salt in one of the four intermediate heat exchangers. These heat exchangers are initially designed as cross-flow heat exchangers in which the primary salt flows on the tube side. The secondary salt flows on the shell side and then proceeds to the gas turbine for the production of electricity. This design has a vessel outer diameter of 6.0 meters and a height of 10.6 m [7, Apdx I].

3.2 Vessel Material

Figure 3.3 gives a big-picture overview of material strength at high temperatures, which is of primary concern in the FHR. Most of the materials in this illustration are ceramics

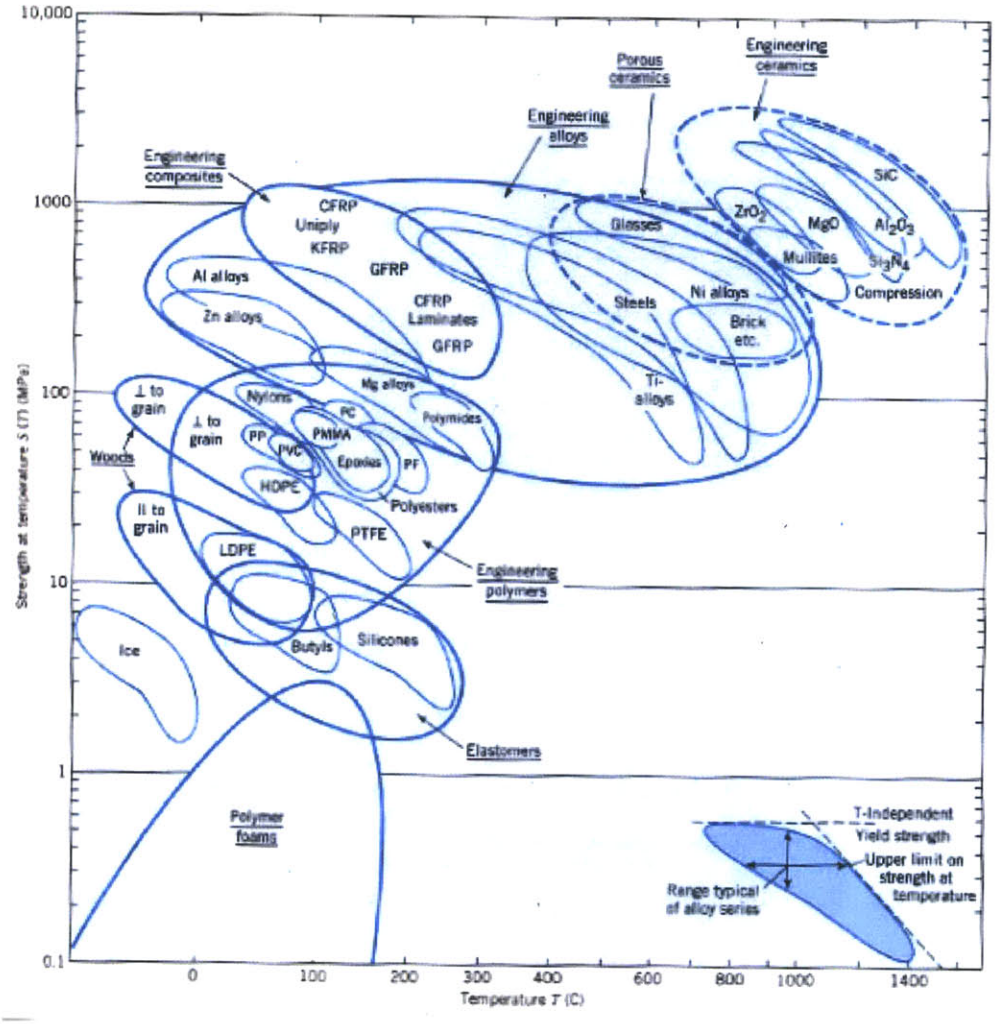

Figure 3.3: Strength at T vs Temperature [13].

because they are the only engineering materials with long-term strength above 1000° C. However, Nickel alloys and steels exist in the region of 700° C. Note that the "strength" in this region is short term yield strength; that is, yield strength for one hour loading. For longer times, creep must be taken into account. Though further iterations are required on vessel design, some alloys are promising in their prospect of retaining high tensile strength

at higher temperatures for long time intervals [26].

Based on the unique high-temperature, low-pressure operation of the FHR, two materials are currently being considered for the vessel. The first is an alloy called Hastelloy N, and the second is austenitic Stainless Steel 316. These are both selected for their high-temperature creep resistance properties and corrosion resistance in the salt environment.

Much of the initial FHR vessel design is based on extensive research completed in the 1960s at the Oak Ridge National Laboratory for the Molten Salt Reactor Experiment (MSRE); this was a test reactor to determine the technical viability of a Molten Salt Reactor as a commercial reactor. The molten salt reactor developed from the earlier Aircraft Nuclear Power (ANP) program [7]. During this time, extensive material design and testing of Hastelloy N (called Alloy N from here) was completed to support this project. Alloy N is a Nickel-based alloy developed at ORNL; it has good balance of corrosion and mechanical properties expected in the low-pressure, high-temperature salt cooled environment [24].

Stainless steels, on the other hand, are commonly used engineering materials which are alloyed to be heat resisting. Additionally, they have superb resistance to corrosive attack in air due to the higher concentration of alloying Chromium. Moreover, stainless steels have high strength, excellent workability, abrasion, and erosion resistance, magnetic properties, and ease of cleaning and sterilizing surfaces. The subtype austenitic stainless steel, such as Stainless Steel 316, has high ductility and high tensile strength which allows for ease of forming. They are easily welded and work hardened. The 300 series stainless steels have the best strength properties above 540° C [12].

Stainless Steel 316 has been in widespread use throughout a variety of industries [11]. It (1) is a cheaper alternative than Alloy N, (2) has an existing code in nuclear applications, (3) is readily available, and (4) is easily formable for the gamut of reactor components; therefore, this analysis uses a Stainless Steel 316 vessel for the base design [25].

Element	wt %
C	0.080
Mn	2.0
P	0.045
S	0.030
Si	1.0
Cr	16-18
Ni	10-14
Mo	2.0-3.0

Table 3.1: Stainless Steel 316 Composition.

Stainless Steel 316 From the ASM data sheet, AISI type 316 is a molybdenum-bearing, chromium-nickel, stainless and heat resistant steel. It has superior corrosion resistance over other chromium-nickel steels in air. This is a highly desirable quality when the steel vessel exterior is to be in constant contact with air near 600° C. However, there are uncertainties with respect to long-term corrosion in salts. The backup option is to add a clad to the vessel interior—similar to what is done with Light Water Reactor vessels. No structural credit is given to the clad. Moreover, Stainless Steel 316 offers higher creep, stress-to-rupture, and tensile strengths than any other stainless steel. The composition is given in table 3.1 [12].

Pertinent data for the pressure vessel analysis of a Stainless Steel 316 vessel is given in table 3.2.

Stainless Steel 316

T_{melt}	1400°C	ρ	8000 kg/m^3
C_p	500 J/kg-K	α	20 μm/m-K
25°C:			
σ_y	580 MPa	σ_{ult}	290 MPa
760°C, static and creep (10^5 hr):			
σ_y	240 MPa	σ_{ult}	125 MPa
σ_{rupt}	30 MPa	$\sigma_{1\%\epsilon}$	15 MPa

Table 3.2: Stainless Steel 316 properties [12].

3.3 FHR Vessel Analysis

Reactor vessels are designed in accordance with ASME Code, Section VIII. This analysis uses ASME code and known properties of Stainless Steel 316 to determine the required vessel thickness for use in the FHR.

Since the FHR nominally operates at atmospheric pressure, pressurization of the vessel only comes from the head produced by the pump in order to circulate the flibe coolant and from the hydrostatic pressure due to the salts. Although this will lead to an axial pressure gradient, because of the small pressures developed, this analysis will use a constant internal pressurization assuming the maximum developed pressure.

Although the FHR design is in its infancy, and power output is not yet determined, this analysis assumes 1500 MW_{th} as the design power of the reactor for vessel considerations. Core power of less than 1500 MW_{th} was used for the simulations; this is discussed in Section 6.2.1. Reactor exit temperatures are expected to be 700° C with reactor inlet temperatures of about 600° C [3]. This data can be used to determine the required flowrate of the coolant, and with some assumptions regarding thermal hydraulics from PWR studies, one can find an approximate pressure developed in the FHR.

Properties used are stated in Table 3.3.

Properties

Item	ρ	C_p	k
flibe	1940	2414	1.0
Stainless Steel 316	8000	500	22

Table 3.3: Properties Used in Vessel Analysis.

The flowrate to produce the required thermal power is:

$$\mathrm{P_{out}} = 1500\ \mathrm{MW_{th}} \tag{3.1}$$

$$\mathrm{P_{th}} = \dot{m} c_p \Delta T \tag{3.2}$$

$$\dot{m}_{coolant} = \frac{1.5E6}{2414\,\mathrm{J\text{-}kg/K} \cdot 100\,\mathrm{K}} \approx 6200\,\frac{\mathrm{kg}}{\mathrm{s}} \tag{3.3}$$

Assuming a conservatively low Re of 5×10^4, using the McAdams relation for friction factor, 7 vertical meters of pumping (discussed in Chapter 6), a hydraulic diameter and loss coefficients similar to that found in a 3000 MWth PWR, one can estimate a pressure developed by the pump:

$$\begin{aligned} \Delta p &= L\frac{fG^2}{D_e 2\rho} + L\rho g + K\frac{G^2}{\rho} \\ &\simeq 300\,\mathrm{kPa} \simeq 45\,\mathrm{psi} \end{aligned} \tag{3.4}$$

Likewise, hydrostatic head can be estimated:

$$P_{\mathrm{hydrostatic}} = \rho g h = 1940(9.8)(7m) \approx 133\,\mathrm{kPa} \approx 19\,\mathrm{psi} \tag{3.5}$$

In addition to the small internal pressurization from the pump head and fluid load, the vessel will need to be designed to support its weight. The high-temperature operation of the FHR will cause expansion of the vessel from cold conditions to normal operating conditions. To preserve the integrity of the control rod drive mechanism design at the top of the FHR, the vessel will likely need to be suspended. The weight of the system is the combined weight of the FHR vessel and salts plus the fuel. Since fuel loadout is unknown, but the graphite is less dense than the salts, estimating the principal stress developed by hanging the vessel is conservative by assuming the core is all salt.

Using the vessel design described in Chapter 6 and the schematic of Figure 6.1, the weight of the vessel is expected to be 6.1×10^6 Newtons. The cross-sectional of the cylindrical outer vessel is

$$A_{\text{cylinder}} = \pi(3^2 - 2.95^2)\,\text{m}^2 = 0.93\,\text{m}^2 \tag{3.6}$$

Therefore, the principal stress developed in the cylindrical head by hanging the entire FHR by the outer vessel is

$$\sigma = \frac{F}{A} = \frac{6.1 \times 10^6\,\text{N}}{0.93\,\text{m}^2} = 6.5\,\text{MPa} \tag{3.7}$$

The FHR is designed against pressure vessel rules laid out in the ASME code Sections III and VIII. The goal of this code is to design a vessel which does not require a detailed analysis of all the stresses in the vessel. Rather, it applies a series of safety factors and design rules for details of these vessels. The FHR vessel is of similar design to today's light water reactor vessels. The key differences are the much higher vessel temperature and the significantly reduced reactor vessel pressure. By first order analysis above, this internal pressure is expected to total about 64 psig. Since this design is still in its nascent stages and approximations were made, this paper designs the FHR vessel for a peak internal pressure of 150 psig.

Nuclear vessel design has a long history, and it is based on history and practice that the ASME codes apply based on certain material selection, mechanical design, manufacturing processes, quality assurance, installation, and testing standards [23].

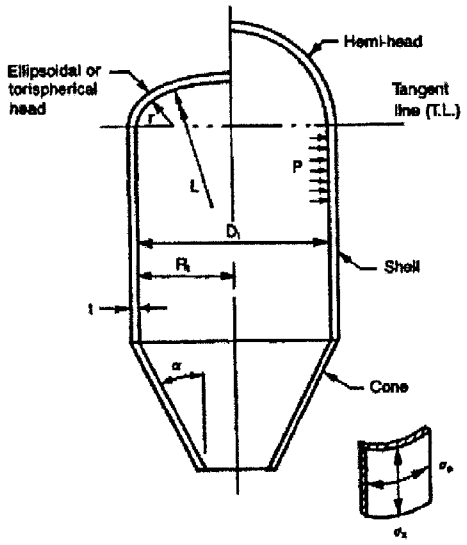

Figure 3.4: Vessel Shell [20].

3.4 General Pressure Vessel Design

Given the pressure vessel in figure 3.4, the ASME designs for a certain set of criteria. Although the FHR vessel is considered a thin-walled vessel for design purposes ($R_{mean}/t < 10$), thick walled distributions are readily available and more accurate. For the purposes of this analysis, external pressure is neglected, as it is expected to be atmospheric.

According to reference [20], both the hoop and radial stresses reach their peak values at the inner surface. But, failure is designed from the outside surface. The inconsistency lies in the constraints. Although the fibers on the inside surface reach yield first, they can not fail because they are constrained by the outer portions of the shell. Once above the yield conditions, the plastic flow direction is in the radial outward direction and causes hoop stress to be relieved at the inner wall. This comes at the expense of the outer wall; this leads to failure occurrence at the outer vice inner wall despite the stress peak on the

inside.

For a cylindrical vessel with a hemispherical head, if the thicknesses are identical (assumed to be true for this analysis), the maximum and minimum stresses would occur on the inside wall of the cylinder and be equal to:

$$\sigma_\theta = \frac{PR_i^2}{R_o^2 - R_i^2}\left(1 + \frac{R_o^2}{R_i^2}\right) \tag{3.8}$$

$$\sigma_r = \frac{PR_i^2}{R_o^2 - R_i^2}\left(1 - \frac{R_o^2}{R_i^2}\right) \tag{3.9}$$

$$\tau_{\max} = \frac{\sigma_\theta - \sigma_r}{2} = \frac{PR_o^2}{R_o^2 - R_i^2} \tag{3.10}$$

For the FHR, this yields principal stresses of:

P = 150 psi = 1 MPa	
σ_θ	19.5 MPa
σ_r	1 MPa (C)
τ_{max}	10.3 MPa

Table 3.4: Thick-Walled Vessel Principal Stresses.

For the thick-wall design pressure vessel of 3.4, the ASME criteria has determined formulas for minimum thickness, maximum pressure and maximum allowable stress in any given vessel. These formulas are valid for pressures less than 3000 psi and vessel thickness less than one half of the mean radius [20].

The general vessel formulas accepted by the ASME code are found in Table 3.5.

Allowable stress is taken to be the lesser of $\frac{2}{3}\sigma_y$ or $\frac{1}{3}\sigma_{ult}$. The weld efficiency, E, relates the expected strength of the weld to the allowable stress value, and is taken from code UA-60 [18].

Since the peak operating vessel temperature is expected to be 700°C, this analysis

Longitudinal

	I.D.	O.D
t	$\frac{PR_i}{2SE+0.4P}$	$\frac{PR_o}{2SE+1.4P}$
P	$\frac{2SEt}{R_i-0.4t}$	$\frac{2SEt}{R_o-1.4t}$
S	$\frac{P(R_i-0.4t)}{2Et}$	$\frac{P(R_o-1.4t)}{2Et}$

Circumferential

	I.D.	O.D
t	$\frac{PR_i}{SE-0.6P}$	$\frac{PR_o}{SE+0.4P}$
P	$\frac{SEt}{R_i+0.6t}$	$\frac{SEt}{R_o-0.4t}$
S	$\frac{P(R_i+0.6t)}{Et}$	$\frac{P(R_o-0.4t)}{Et}$
S = Allowable Stress		
E = Weld Efficiency		

Table 3.5: ASME Vessel Requirements for minimum thickness, t, maximum pressure, P, and maximum allowable stress, S.

"Allowable Stress"			
$\frac{2\sigma_y}{3}$	83.3 MPa	$\frac{\sigma_{ult}}{3}$	80 MPa
S		80 Mpa	
E		0.85, nuclear-grade weld	

Table 3.6: Allowable Stress, 760° C, Stainless Steel 316.

will use the strength properties ASM lists for 760° C given in Table 3.2. Moreover, weld efficiency for the butt and filet welds in nuclear vessel applications is commonly accepted to be 0.85 [18].

Using the ASME basic code parameters for a static vessel with no special (i.e. discontinuity or seismic) loads, one calculates the minimum required shell thickness, maximum internal pressure, and minimum allowable stress, S, of the material in Table 3.7.

Longitudinal

	I.D.	O.D
t	2.1 cm	2.2 cm
P	7.3 MPa	7.3 MPa
S	10.9 MPa	10.9 MPa

Circumferential

	I.D.	O.D
t	4.2 cm	4.2 cm
P	3.5 MPa	3.5 MPa
S	23.1 MPa	23. 1MPa

Table 3.7: Minimum Design Criteria.

An additional ASME design concern is to keep all primary membrane stresses under the S value from Table 3.7. Equation 3.7 shows that the expected principal stress due to hanging the FHR of 6.5 MPa is much less than the allowed 80 MPa. Furthermore, based

FHR Vessel	
R_i	2.95 m
R_o	3.0 m
t	5 cm
$H_{overall}$	10.6 m

Table 3.8: FHR Vessel Dimensions.

on a maximum operating design pressure of 150 psi (1.0 MPa), a shell thickness of 5 cm throughout the vessel and a material S value of 80 MPa, these initial design requirements are easily met. The thin-walled vessel implies that the resistance to heat transfer through the vessel will be small.

Chapter 4

Silo Cooling System

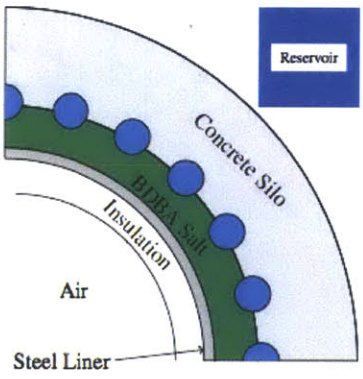

Figure 4.1: Silo Cooling System.

The FHR reactor vessel is surrounded by an air-filled gap, insulation, a steel silo liner, the frozen BDBA salt, the silo cooling system, and the reactor silo (Figure 4.1). The silo is likely to be concrete, although there are a few other candidate materials that will be examined. The purpose of the silo is to provide containment and to provide some heat transfer and cooling capability.

During normal operations, the active cooling system within the silo prevents heat dam-

age to the concrete and the equipment in the silo by circulating water via cooling channels in the wall to prevent concrete degradation. This will ensure that the concrete is exposed to a normal operating temperature over its many decade lifespan. Cooling channels are located behind the steel silo liner and BDBA salt between the salt and concrete. This same cooling system is designed to provide cooling that may stop severe accident progression before vessel failure–depending on reactor decay heat.

The initial assessment is to use water cooling in a system where the temperature is controlled during normal operation by cooling the water that cools the silo. In this accident scenario, the silo cooling system goal shifts from active cooling to keep concrete at design operating temperatures to passive heat removal in order to reject decay heat. During a BDBA, the water removes heat by boiling—a totally passive system where steam can be vented and added water be provided by a passive water tank. The basic design is from silo cooling systems for High Temperature Gas Reactors. For the BDBA simulations modeled in this report, a complete failure of silo cooling was assumed to examine if fuel failure can be prevented in worst-case conditions. This assumes even passive silo cooling failure.

Experimental work with a similar cooling system for gas-cooled reactors at the University of Wisconsin and University of Idaho is promising. Wisconsin has a scaled water-cooled Reactor Cavity Cooling System that performs both active (one-phase water) cooling and passive (which produces two-phase) cooling outside the reactor pressure vessel. Their initial experiments demonstrate that the concept can remove a significant amount of decay power; when their prototype is scaled to the full design, decay heat removal from this cooling system may be over 2MW [16] in a 350 MW_{th} gas-cooled reactor—higher in a FHR with higher reactor vessel temperatures.

Chapter 5

Insulation Failure

A significant requirement in this worst-case accident scenario is the degradation or failure of reactor vessel insulation in a BDBA. The insulation must be a high quality insulator during normal reactor operations, as the radiative heat transfer due to the high operating temperature promises to be significant. This same insulation is a formidable barrier to decay heat transfer outside the vessel to the environment in a worst-case accident scenario. A number of options are available, as well as those that must still be explored, to eliminate the insulation and allow removal of decay heat in a BDBA.

During normal operations, the vessel temperature is about 600° C. The vessel insulation system is designed to minimize heat losses to the silo cooling system during normal operations. But, *it must be designed to fail as the vessel temperature rises.* Insulation failure results in massive radiative and convective air heat transfer to the silo structure and may stop the rise of the vessel temperature over time and its subsequent failure. This is the lynchpin upon which the BDBA heat removal system design rests.

Several thermal insulation systems have been identified that insulate the reactor system at operating temperatures but allow efficient heat conduction to the silo at higher

temperatures.

- *Mirror Insulation.* Radiation heat transport reduces the insulating effect of mirror-type insulation above 600° C.
- *Melt Insulation.* Any insulating material designed to melt at a low enough temperature and pool at the bottom of the silo.
- *Fall-away Insulation.* Any of the insulation which loses contact with the silo structure in a certain range of temperatures.

In all cases, there is a requirement that the insulation allow efficient heat transfer if exposed to hot liquid salt. This can be accomplished by the insulation failing or insulation with appropriate channels to allow salt flow. An example of the latter is mirror insulation, which is discussed below. *In all cases, the design objective is to reduce the temperature drop required to move heat from the reactor core to silo under accident conditions.*

5.1 Mirror Insulation

Mirror insulation, or reflective metal insulation, is in use at every nuclear power station in the United States [10]. It is a specialized form of reflective insulation widely used in nuclear applications. Mirror insulation significantly reduces heat transfer by thermal radiation. It is composed of multi-layered, parallel, thin sheets (or foils) of highly reflective metallic materials. These are spaced to reflect thermal radiation back to its source. This spacing is designed to restrict the motion of air, and in high performance insulations, the space is evacuated. The evacuation of this space reduces the effective thermal conductivity in the system [1].

Mirror insulation is widespread in the nuclear industry and its qualities are well known. It was originally patented by Babcock and Wilcox in 1975 (#3892261) and underwent a

series of patent improvements by the same and other companies.

Mirror insulation is a possible candidate in the FHR because it contributes to the BDBA systems insulation failure at high temperatures. There are two mechanisms that will aid in this insulation degradation.

First, at high temperatures, the reflective metal layers will significantly degrade their insulation capabilities. This occurs through increased emissivity (reduced reflectivity) and consequently increased radiation heat transfer to the silo as well as increased thermal conductivity, therefore increased conduction to the silo wall. This degradation is more pronounced for the inner layers of reflective material, as they will be exposed to the higher temperature environment—and thus degrade—earlier in the accident sequence.

The second mechanism that will work in mirror insulation degradation is the use of the evacuated or gas-gapped channels between the reflective metal layers. These channels will be exposed from underneath to the gas-filled gap between the reactor vessel and the insulation. During the reactor accident, this gap will be subject to flooding by the BDBA salt and reactor vessel salt if significant reactor vessel failure was to occur. These flooded salts will fill the lower part of the channels in the mirror insulation, creating conductive and convective heat transfer through the insulation to the silo.

The disadvantage of using mirror insulation is that its failure mechanism is of questionable effectiveness and its time scale appears to be long. It will take a rise of a few hundred degrees C to see initial degradation of the mirror insulation. When this does occur, it will take much longer for the outer layers to be degraded so there is meaningful heat transfer to the silo wall. Furthermore, the filling of the channels with any of the salts will take time. Even the BDBA salt, the first of the likely salts to fill these gaps, will not melt and yield meaningful heat transfer until a significant time has occurred. Therefore, other insulation failure mechanisms are being considered.

5.2 Melting Point Insulation

The insulation can be designed to melt and flow to the bottom of the silo upon overheating. The liquid state of insulation may be abundant enough to form a liquid pool in the base of the silo. In solid form, the insulation contains gas spaces that are the primary barrier to heat flow. There are several candidate metals and salts within the appropriate range of melt temperatures. Once the solid melts, liquid puddles at the bottom of the silo. As the liquid level rises in the silo, it enables convective liquid heat transfer between the hot vessel and the silo wall.

This concept is not as well tested in industry as applications like mirror insulation. One of the reasons is that current reactors cannot withstand high enough temperatures to reach the melting point of most metals before the fuel fails. However, while this concept will be explored, finding materials that significantly melt early enough in the BDBA to allow decay heat to transfer to the silo wall before vessel failure—and with adequate margin to fuel failure—may prove to be difficult. That is, the ideal design of the insulation failure will occur early in the accident sequence. This allows convective heat transfer (via the gas-gap) and radiation heat transfer to be significant enough to keep reactor core temperatures below the coolant boiling point and fuel failure point and allows reliance on the silo cooling system to remove heat in addition to conduction to earth via the silo and convection via the BDBA salt if the situation escalates to that point. By design, this should all be able to occur while the reactor vessel containing the core and the buffer salt is still intact. Finding a material that has good insulation properties at operating temperature but degrades/melts at significantly lower temperatures than the reactor vessel is proving to be a challenge.

5.3 Fall-away Insulation

In the event of overheating, insulation could fall away so that heat from the reactor vessel can radiate directly to the silo wall. Two major mechanisms that allow fall-away insulation upon increases in temperature are being examined. The insulation can be held in place with temperature-sensitive fusible links, much like the triggering mechanism in fire sprinkler systems. When the temperature increases, the fusible link melts at a preset temperature. Alternatively, the insulation can be held in place with magnets where if their Curie point is exceeded, they become non-magnetic and fail. The fall-away insulation concept at a predetermined temperature is the baseline design assumed for the analysis of accident behavior in this report.

5.3.1 Curie-Point Magnetic Insulation

A magnetic materials Curie point, also called Curie temperature, is the temperature at which certain magnetic materials completely lose their magnetism. Exploitation of the Curie point of ferromagnetic materials could lead to insulation that is held in place by permanent magnets designed to fail at a preset temperature. This preset temperature is tunable, both by materials selection, and by tweaking the non-stoichiometry of certain magnetic compounds. This would drop the insulation away at a design temperature and allow for the radiation and convective heat transfer process described above to happen almost instantaneously when the design temperature is reached.

The use of this property in the nuclear industry began in the late 1990s in Japan. The Japan Atomic Energy Agency and Japan Atomic Power Company have been developing a passive shutdown system in which control rods are inserted during an anticipated transient without scram (ATWS) in a liquid-metal-cooled breeder fast reactor, the Joyo Mk III. This

self-actuated shutdown system has been developed for use in a large-scale reactor. They have designed the control rods to be held in place by magnets which exhibit failure at a certain temperature in the environment of high temperature, high neutron flux and flowing sodium. Their results have been published and demonstrate a significant capability of these magnets to perform as intended [28].

The advantage of using this concept to hold insulation in place during normal operations is that there is now over twenty years of research and experimentation upon which to rely and concept validation in the hostile nuclear environment. Curie point properties are well known, and differing materials exhibit Curie points between 120° C to over 700° C, which allows for a very wide range of insulation failure temperatures [17].

A concern for all drop-away insulation is the total insulation volume. It will fill space at the bottom of the silo in a BDBA; if it remains intact, it will provide insulation at the bottom of the silo. Ideally, one would want an insulation that drops away quickly for rapid heat transfer and then melts or degrades to lose its insulating properties. There are possible options such as glass foam that melts at higher temperatures, glass cloth that would melt, or glass cloth that would become saturated with the BDBA salt. There are equivalent metallic materials.

In all cases there is the need for reliable systems since accidental loss of vessel insulation would subject the vessel to a major thermal transient that could reduce vessel lifetime. There must be high confidence that only high temperatures (not radiation damage or other mechanisms) initiate curie-point magnet operation.

5.3.2 Fusible Link Insulation

Fusible links, or thermal fuses, are another promising candidate for fall-away insulation. The insulation can be held in place with temperature-sensitive fusible links, much like

the triggering mechanism in fire sprinkler systems. When the temperature increases, the fusible link melts at a preset temperature.

Industrial use of fusible links is widespread. Perhaps the most common and well-known examples are the thermal links that are contained in fire-sprinkler systems, which activate at a preset temperature. They are also used in many appliances with heating elements, such as coffeemakers, where a defective thermostat could yield a dangerous condition. The fusible link provides a safety mechanism to break the current flow path in a high temperature condition.

The advantage of the fusible link insulation concept is that, like Curie point magnets, there is a great body of research and development already done. Fusible link materials are well known with failure points 180° C to over 800° C [17]. Like the Curie-point insulation, the fusible link insulation would likely completely fail in a preset temperature range, and the increased heat transfer from reactor vessel to silo would be near instantaneous.

The disadvantages of using fusible links are the size of insulation required and the lack of testing in the nuclear environment. Similar to the Curie point magnet concept, it would take a significant number of fusible links to hold in place the insulation required during normal operation for the life of the vessel. Unlike the Curie point concept, however, there is less research on the capability of fusible links in the hostile nuclear environment. Chief among these concerns would be the lack of data on stability of the fusible link failure temperature after exposure to high temperatures and radiation.

5.3.3 Dynamic Property Insulation

A material that is a great insulator at low or normal operating temperatures and naturally becomes a good conductor at high—BDBA—type-temperatures would be ideal. With the temperatures that could possibly be reached during a BDBA, many materials exhibit a

change of state or a change of phase. This unique temperature environment may yield some materials of interest.

Although change of thermal properties with temperature has not yet been fully explored, there is some similar promising research in the thermal conductivity field that is somewhat related. Within the past decade, researchers at Brookhaven national laboratory discovered materials that were both good insulators and conductors—depending on which way the heat was transferred [14].

The advantages of this type of insulation system are readily apparent. There would be no need to remove or physically change the insulation in order to have desirable heat transfer qualities during normal operation and accident conditions. The disadvantages of this system do not reside in the concept, but in the limited research and knowledge of these types of materials.

5.4 Summary

Success of the FHR in a beyond design basis accident is critically dependent on insulation failure. The high fuel and coolant operating temperatures of the FHR dictate that there is a highly effective thermal insulator to keep the heat in the vessel during normal operation. Yet, this insulation becomes a detriment to heat transfer during a worst-case accident in which all other decay heat removal systems are nonoperational. Therefore, there must be a reliable system by which insulation is removed or significantly degraded during accident conditions such that it allows the reactor core to remain below coolant boiling and fuel failure temperatures.

Many ideas are available for insulation failure. Simple systems like melting insulation and the already widely used mirror insulation are feasible, but have significant disadvantages. Fall away insulation is promising, and there is large scale industrial experience on

several systems that could be used (fusible links and curie point magnets). Further research may even yield a suitable insulation that does not need to change but may become a suitable conductor at the temperatures required. For the analysis herein a fall-away insulation is used since both fusible link and Curie-point magnets are demonstrated technologies.

Chapter 6

Parts and Geometry Models

6.1 FHR BDBA System Overall Geometry

Based on the vessel dimensions of Chapter 3, the overall geometry was set up as seen in Figure 6.1. The FHR BDBA system surrounds a core. The internals of the core were neither modeled nor analyzed due to the high levels of uncertainty in core design. Rather, a cylindrical core vessel with hemispherical bottom head was constructed. The overall height of the core is 7 meters including the vessel and the radius of the core is 1 meter. The vessel is 5 cm thick; therefore, the core itself extends from 3.05 to 9.95 meters (Figure 6.1). The core will not only contain the nuclear fuel, but also the primary coolant and a number of coolant support systems. Tentative initial designs of the core and primary coolant systems can be found in Figure 3.1.

Surrounding the core is the buffer salt tank. This buffer salt is modeled as FLiNaK as described in Chapter 2. The buffer salt tank was designed to be geometrically similar to the core with increased scaling. The tank has an inner and outer radius of 1 meters and 2.95 meters respectively, and in enclosed by a 5 cm outer vessel. The bottom of the tank is

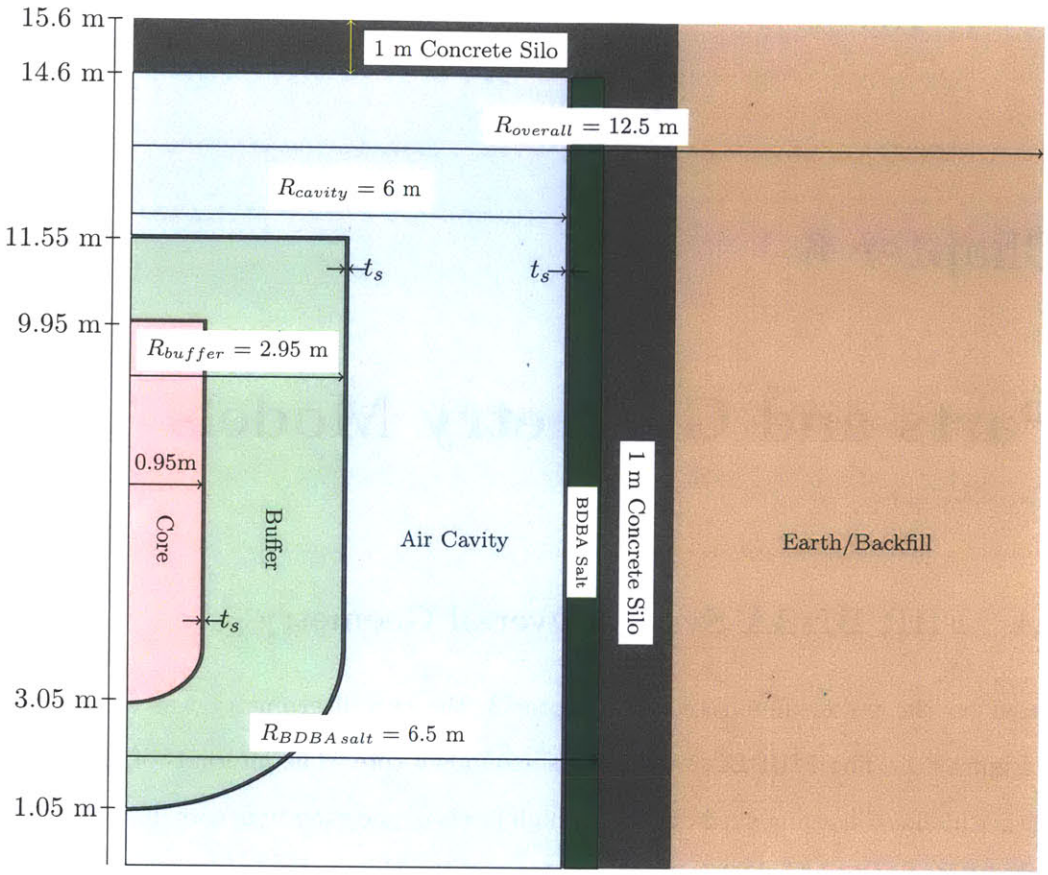

Figure 6.1: FHR Geometry Modeling.

1.05 meters from the FHR base (ground) and extends to 11.55 meters vertically from the base.

The steel vessel surrounds and conforms to the geometry of the FHR salt tank. For reasons explored in Chapter 3, notably that the vessel operates at atmospheric pressure, the steel only needs to be 5 cm thick—or roughly two inches. Surrounding the steel vessel is the large air cavity. This air cavity was designed to completely surround the FHR vessel

from ground to the design height of 14.6 meters with sufficient distance between the vessel and the steel silo liner in order to allow for air currents that will not significantly interfere with each other when they form due to the significant temperature differences in this cavity. As is discussed in Chapters 9 and 10, two cases were evaluated: one with a 3 meter annular air gap and a case with a 1 meter annular distance.

The outer elements of the steel liner, BDBA salt column, concrete silo, and Earth have simple geometries. The liner extends from the ground at 0 meters to the full height of 14.6 meters. Like the steel vessel, the liner needs only to be nominally thick; 5 cm was again chosen. One half meter thickness was chosen for the BDBA salt. With a large reservoir of the BDBA salt above the FHR vessel as a makeup salt in the event of melting during a beyond design basis accident, the thickness of this BDBA salt is not required to be too significant, since the makeup volume will come from outside the modeled geometry.

The concrete was modeled as a 1 meter thick annulus. The concrete silo will also extend above the vessel as shown in Figure 6.1. The earth was modeled as a 5 meter thick annulus. In reality, the earth or backfill extends for many meters outside the FHR. The goal in modeling the backfill in this model is to see where the heat would flow in the earth environment. Five meters is sufficient to show the heat transfer from the FHR during a beyond design basis accident without significant increase of the outer radius temperature. In this context, it is observed that the heat is conducted upward toward the surface (which remains at a nearly constant temperature). This ultimately limits heat conduction in the *radial* direction as heat transfer preferentially flows in the *upward* direction to the atmosphere. This is discussed further in Section 6.6.

Figure 6.1 shows a 2-dimensional slice of the FHR cylindrical geometry. The computer model of Figure 6.1 is shown in Figure 6.2. Note that the computer geometry is only a 15° slice of the overall geometry. Each of the vertical planes is modeled as symmetry

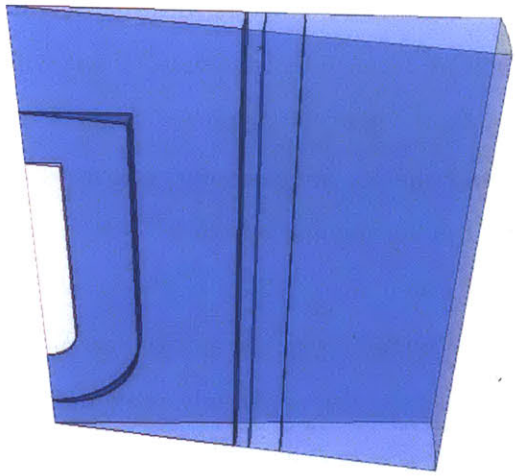

Figure 6.2: STAR-CCM+ Geometry View.

boundaries. Since the FHR as modeled here is cylindrically symmetric, significant computational power is conserved without affecting the results, as the STAR-CCM+ modeling software incorporates symmetry boundary conditions.

6.2 Core Model

The FHR core will contain the fuel and the primary coolant. Initial designs call for high-temperature graphite-matrix coated-particle fuel. This is the fuel developed for helium-cooled high-temperature reactors. It has fuel failure temperatures near 1650° C. The design maximum coolant temperature under normal operations is approximately 700° C. Currently, China is constructing a pebble bed fuel reactor and the United States Department of Energy Next Generation Nuclear Power Plant program has demonstrated that this fuel can be manufactured with very low defects.

The fuel itself consists of small microspheres approximately the size of a grain of sand. These are incorporated into a graphite matrix of different geometries. Many fuel options

are still being explored as detailed in Reference [7], and initial research has begun to design a test reactor that can accommodate different coolants and fuel designs [25].

A substantial volume of the core will be the primary coolant that circulates around the fuel. The baseline design for the primary coolant is a flibe salt mixture of ^{7}LiF and BeF_2. This salt has been successfully used in the Molten Salt Reactor Experiment in the late 1960s with an operating temperature of 705° C. This experiment demonstrated the ability to use flibe (with its high melting point) in sustained high-temperature operation with excellent corrosion rates and compatibility with graphite. Furthermore, it has the lowest neutron absorption of the candidate salts studied so far for efficient fuel usage, and a negative void coefficient with its positive effect on reactor safety. The major disadvantages of using flibe salt is Beryllium toxicity and the high cost of the salt [7].

The design of the FHR core is rapidly evolving. Advanced options in fuel design include pin fuel assemblies with silicon-carbide-matrix clad. Cost and toxicity of the flibe salt are motivating research into lithium fluoride and zirconium fluoride as well as sodium fluoride coolants. Though the core is an uncertain part of the FHR system, the goal is to have a fuel surrounded by a liquid salt at atmospheric pressure. This model used a core containing flibe coolant with a constant volumetric heat source.

6.2.1 Core Power

The goal of the FHR is to provide economic production of electricity and process heat [3]. A starting point for core power design is current PWR designs. Data compiled from the Seabrook Station Reactor, which operates at 3411 MW_{th} is used for the first analysis. The height of the Seabrook vessel is 13 meters, with a cylindrical radius of 2.5 meters. Treating the vessel as a cylinder by ignoring the hemispherical head, one can find the volumetric power density of the Seabrook Station PWR [29]:

$$q''' = \frac{3411 \times 10^6\,\mathrm{W}}{\pi(2.5\,\mathrm{m})^2(13\,\mathrm{m})} = 4.2 \times 10^7\,\mathrm{W/m^3} \tag{6.1}$$

This simulation rounds this volumetric power density up to $5{\times}10^7$ W/m^3. The FHR core is modeled as a hemispherically-headed cylindrical vessel with an overall volume of $\pi r^2 h + (0.5)4/3\pi r^3$. Recalling that the radius of the core is 1 m, the height of the cylindrical portion is 6 m, and there is a 1 meter radius head (Figure 6.1), the overall power output for the modeled FHR core is:

$$P_{\mathrm{core}} = q'''V = 5 \times 10^7\,\mathrm{W/m^3}\pi\left((1\,\mathrm{m})^2(6\,\mathrm{m}) + (1/2)(4/3)(1\,\mathrm{m})^3\right) = 1047\,\mathrm{MW} \tag{6.2}$$

The flibe in the core will begin the heatup process upon accident initiation with the shutdown of the secondary heat removal system. This primary coolant is a major contributor to the thermal inertia of the FHR in an accident. The high density of the salt and its favorable specific heat capacity allow the flibe to absorb significant amounts of heat which will raise the temperature of both the fuel and the primary coolant, but in a controlled manner. If the fluid were stagnant, heat transfer would need to occur entirely by conduction through a minimally conducting salt. In order to have effective heat transfer out of the core, convection needs to occur. The core design must allow some convective currents in an accident situation.

Obtaining an effective circulating salt will be a challenge. The FHR core is cylindrically symmetric. A flat radial and axial power distribution would provide no radial, axial, or polar temperature differences. The fluid would be stagnant. While fuel loading and design has not been accomplished for the FHR, the core is modeled with a cosine shaped axial and radial power distribution to provide hotter regions (with the hottest at the bottom center)

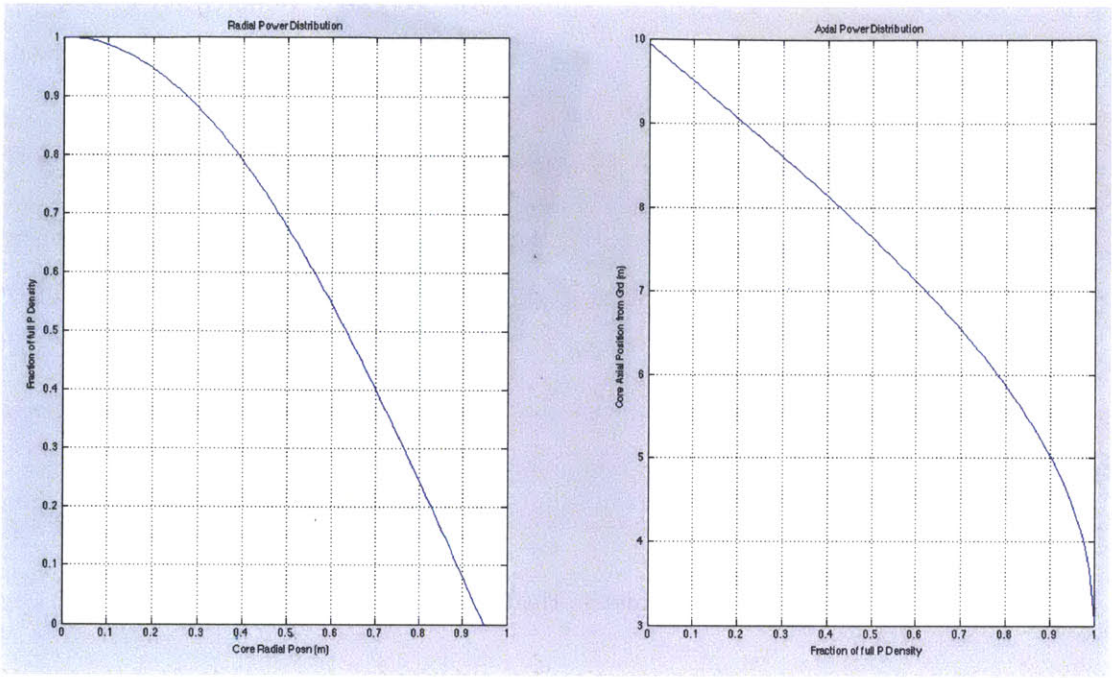

Figure 6.3: Axial and Radial Power Distribution Plots.

and colder regions (with the coldest at the upper, outer corner). Peak heat production is in the center of the core, approximated by a cosine shaped radial distribution reaching zero heat production at the vessel interface. Likewise, an axial variation was modeled with the peak production at the bottom, reaching zero heat production at the top of the core. This allows the atmospheric pressure liquid flibe to circulate in the core, which will keep the primary volume nearly isothermal, and provide efficient natural-circulation liquid heat transfer to the buffer salt and ultimately to the outer surface of the buffer vessel.

The plot of axial and radial power distribution as a fraction of the full heat source are illustrated in Figure 6.3. The overall volumetric power density with position in the core is given in Figure 6.4. This is further discussed in Section 7.1.

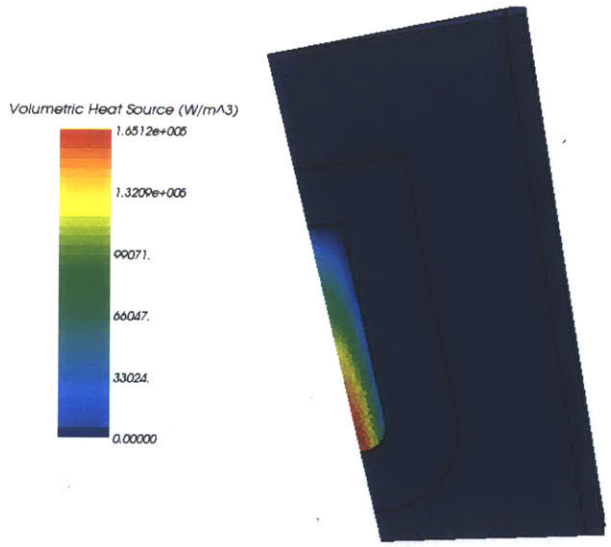

Figure 6.4: Volumetric Heat Source Distribution.

6.3 BDBA Air Cavity

Between the buffer vessel to the steel liner is a volumetrically large gap. This is modeled with air. Future studies may demonstrate a better gas with which to fill this gap. The gap will surround the buffer vessel from the FHR ground to the upper atmosphere boundary. A gap thickness of 3 meters was chosen to significantly separate the convectively–driven upwards flow surrounding the outside of the hot buffer vessel from that of the relatively cool steel liner. This same 3 meter distance was modeled for the gap distance between the buffer vessel upper boundary and the atmosphere boundary to prevent constriction of the air flow where the hot FHR buffer vessel is directly below the cold atmospheric boundary. This is the base case geometry. A reduced annular gap case was also examined with a one meter annular gap as discussed in Chapter 10.

As the accident sequence progresses, the BDBA salt reaches its liquidus temperature and begins the process of melting. Because of the air currents driving the hottest air to

the top of the BDBA salt column, melting is expected to begin in this region. As a result, the BDBA system should be designed to spill the liquifying BDBA salt from the top of this column, which is coincident with the base of the BDBA reservoir. To melt the BDBA salt once the temperature reaches liquidus temperature, the latent heat of fusion must be added. As a conservative first estimate of this BDBA system's heat removal power, the air cavity remains air throughout the scenario until enough heat has been input into the salt to immerse the FHR buffer salt tank in salt. By showing that the core temperatures will be low enough to prevent fuel failure without any liquid-BDBA salt convection during these first few critical hours until enough heat enters the salt to immerse the buffer salt tank, it is demonstrated that the FHR can sustain a long-term accident without any operator action. BDBA salt circulation is modeled with the air cavity replaced by liquid FLiNaK salt when sufficient heat has been input into the solid salt.

6.4 BDBA Salt Two-Phase Model

The BDBA salt is designed to melt and flood the reactor cavity in order to increase heat transfer from the buffer vessel to the silo liner. This process requires a heatup from the BDBA salt equilibrium operating temperature to the salt's liquidus temperature, followed by the input of heat to overcome the latent heat of fusion before the salt becomes liquid and begins to flood the cavity.

Modeling of two-phase fluid dynamics remains very difficult. The best way to use two-phase modeling for the type of melting seen in the FHR is to use the volume of fluid (VOF) multiphase model. The VOF model resolves the interface between the phases of immiscible fluids as would be seen in the liquid-solid interface of the BDBA salt. This method does not model any additional inter-phase interaction, and it assumes that all phases share the same pressure and temperature. The VOF model is suited for flow simulations where each

phase constitutes a large structure, with a relatively small surface area, such as would be expected in the BDBA salt.

However, in a complex system such as the FHR BDBA system, modeling two-phase flow is computationally prohibitive. The only time varying input for the system is the decaying heat flux entering the reactor. Though an unsteady problem, because of the slowly changing heat input and the slowly changing temperature and velocity fields, the system can run relatively quickly overall when modeled as one phase. Adding the second phase requires tracking every mesh point's content of phases and changing the velocity from zero to a non-zero value in varying cells with each time step. In order to get convergence in the model, the number of time steps needed must increase by at least one order of magnitude, and the number of steps to advance one time step also increases by at least an order of magnitude. The result is greater than two orders of magnitude more computational steps are required to accurately model the two-phase BDBA salt. This is an impracticality for a system that needs to be modeled for greater than 10^5 seconds during an accident scenario.

Simplifications and knowledge of BDBA salt behavior during the accident greatly simplify the analysis. Modeling the BDBA salt as a one-phase solid is wholly accurate while the system is below its liquidus temperature. With the reservoir of BDBA salt above the system geometry, the entire BDBA salt column will remain at or below its liquidus temperature during the accident, since makeup salt is filling the void remaining after any melted salt fills the air cavity. When the average BDBA salt temperature reaches the liquidus temperature, modeling the silo liner/BDBA salt boundary as a constant temperature boundary at the salt liquidus temperature will provide a reasonably accurate, and computationally permissible model.

6.5 BDBA System Reduced Geometry

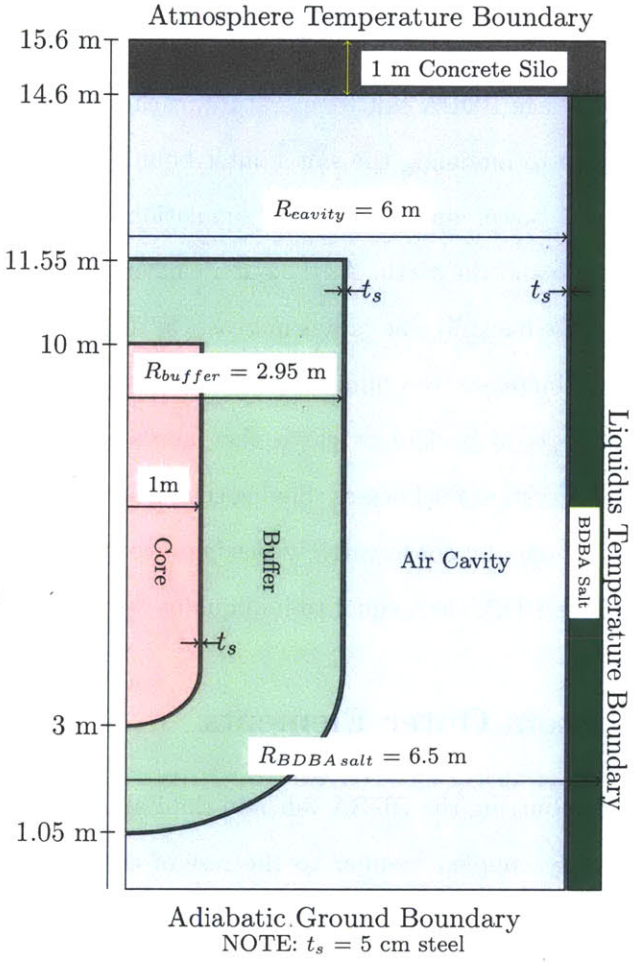

Figure 6.5: Reduced Geometry Modeling.

As discussed in chapter 6.4, the maximum temperature the BDBA salt reaches places an upper limit on one boundary condition. It is therefore conservative to model the outer radius of the BDBA salt as a constant temperature liquidus temperature boundary throughout the simulation. Conditions dictate that this boundary will be at the BDBA salt equi-

librium temperature during reactor operation and heat to the liquidus temperature upon accident initiation, thereby absorbing some heat from the accident in the process. If this boundary is instead modeled as the higher constant temperature boundary, it underestimates the amount of heat absorbed by the BDBA salt, and gives a conservative estimate on the time until the average BDBA salt temperature reaches its liquidus temperature.

The major advantage to modeling the salt's outer boundary as constant temperature is to save computational power during the long simulation that would be expended by modeling the concrete silo and the earth. At the outer elements of the BDBA system (such as the concrete silo and the backfill), the radius increases as does the volume of the modeled parts; this significantly increases the number of elements the solver needs to compute. Furthermore, the thickness of backfill or earth that needs to be modeled is significant compared to all the other system thicknesses. Saving computational power on each iteration is accomplished in this model by conservatively placing a constant temperature boundary at the outer radius of the BDBA salt equal to its liquidus temperature of 725 K (452° C).

6.6 BDBA System Outer Elements

While the concrete silo abutting the BDBA salt and the Earth/backfill of Figure 6.1 were not modeled in a directly coupled manner to the rest of the simulation as described in Section 6.5, an understanding of the dynamic temperature distribution over time in these outer element aids in understanding the overall accident sequence.

Heat transfer through the concrete silo and to the surrounding environment occurs through conduction. Figure 6.6 shows how this geometry was modeled. This outer elements model should be conservative for two reasons:

1. The bottom boundary is modeled as Adiabatic consistent with the rest of the FHR

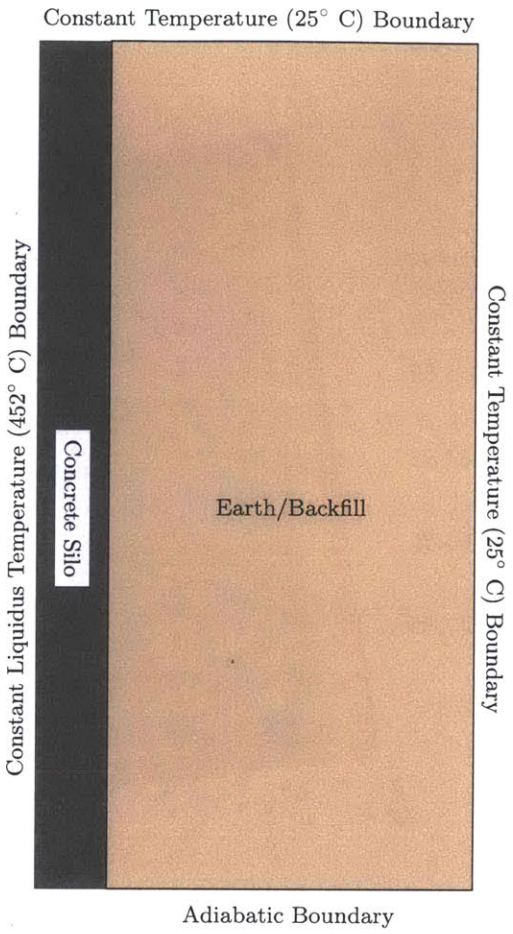

Figure 6.6: Outer Elements System Model.

model; this could be a constant temperature boundary dependent on how much basemat is provided in this area.

2. The BDBA salt/Concrete interface is modeled at the liquidus temperature of 452° C for the duration of the simulation. However, upon initiation of the accident, this interface will be at a much lower operating temperature. It will take time to reach this temperature; during this period, there will actually be less heat input into the

concrete and backfill.

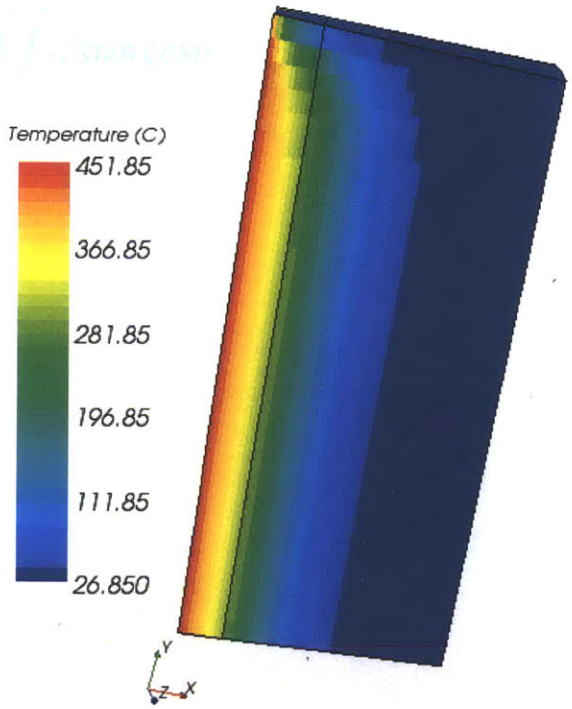

Figure 6.7: Silo and Backfill Temperatures after 5×10^6 seconds (58 days).

The results of the simulation for 5×10^6 seconds are shown in Figure 6.7. This is nearly two months (58 days) of the constant 452° C temperature boundary acting on the concrete silo. Note the colder temperatures at the *top* of the silo in Figure 6.7 due to heat losses via conduction through the silo top to the atmosphere. As will be discussed later, circulating air and the circulating BDBA salt convectively transfer heat *upward*.

Figure 6.8 plots the volume-weighted average temperatures in both the concrete silo and the backfill. The backfill does not see a very significant increase in temperature over the course of many weeks of the accident scenario. As in Figure 6.1, a backfill volume of

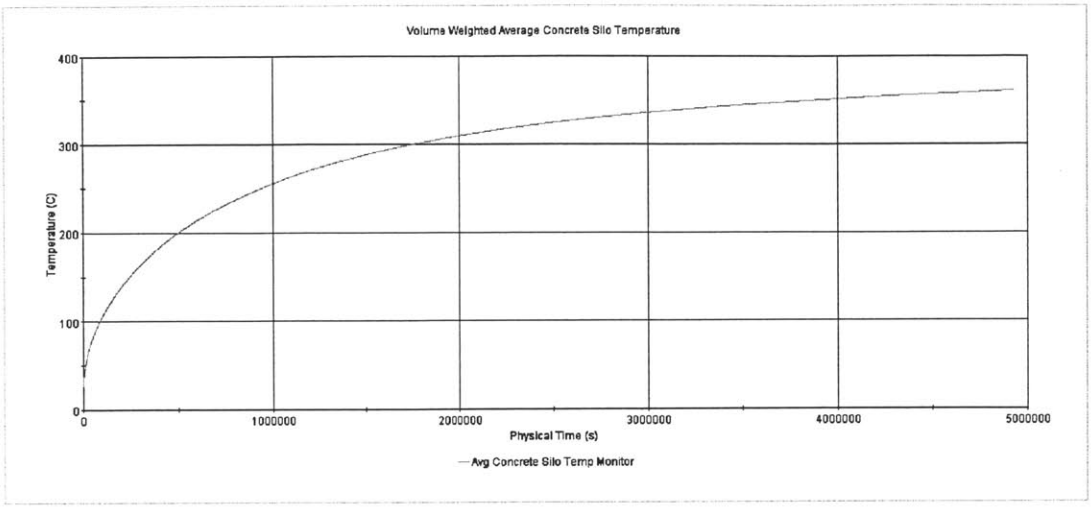

(a) Concrete Temperature through 58 days.

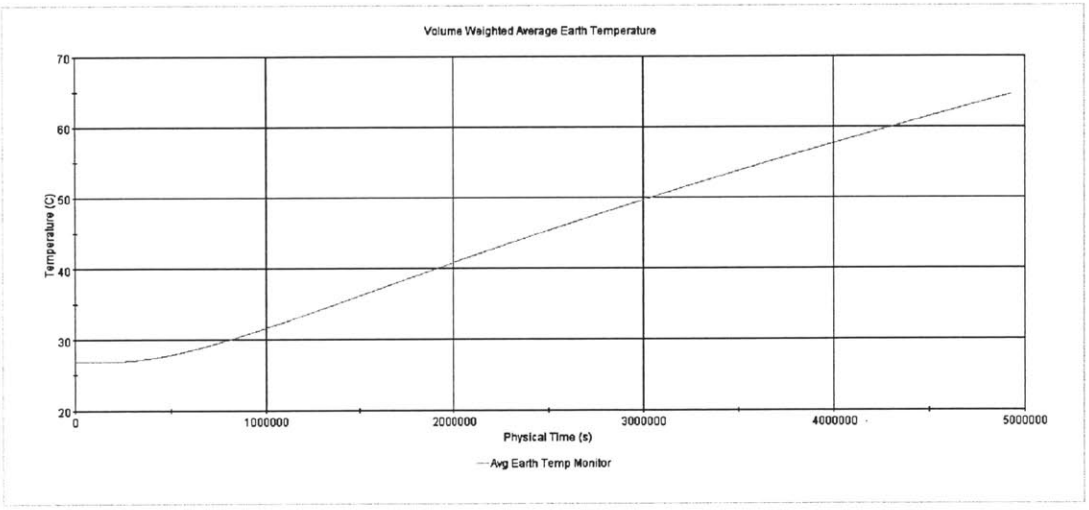

(b) Backfill Temperature through 58 days.

Figure 6.8: Outer FHR Component Temperatures vs Time.

only 5 meters from the silo outer radius should see an increase of less than 50° C in nearly two months.

The concrete silo, on the other hand, will see a significant increase in operating temper-

ature. Recall that during normal operation, there will be an operating silo cooling system in place—in addition to the FHR insulation—to keep the concrete within acceptable operating temperatures. Recall also that this silo cooling system is expected to work passively for a significant amount of time during an accident. But with no silo cooling system operating in any capacity beginning with the initiation of the beyond design basis accident, one could expect to see temperatures approach 100° C within the first 12 hours of accident initiation. A temperature of 200° C would be expected within a day, and maximum temperatures of the concrete could reach over 300° C.

The rapid rise of the concrete temperature will need to be taken into account with the overall FHR design. Depending on the constituents of the concrete, the silo would be expected to release gas upon reaching high temperatures. Vent paths will likely need to be designed into the FHR in order to keep the BDBA salt in the design configuration. Experimentation with concrete heatup and its subsequent behavior is required to understand its affect on the overall FHR beyond design basis accident scenario.

Chapter 7

Initial Conditions

7.1 Heat Input Boundary Condition

The knowledge of decay power in the FHR is not yet developed. However, substantial research in the prediction of decay power in UO_2 fuel assemblies has been documented. The current revision of the American Nuclear Society Decay Heat curve demonstrates a relative error between -5% and +1% from 400 to 4×10^5 seconds (111 hours). For times less than 400 seconds, it is up to 14% conservative. Letting f be the fraction of full power operation present in a given time period, the following data were used [29]:

$$f = -6.14575 \times 10^{-3}\ln(t_s) + 0.060157 \qquad \text{for } 1.5 < t_s < 400 \text{ seconds} \qquad (7.1)$$

$$f = 1.40680 \times 10^{-1} t_s^{-0.286} \qquad \text{for } 400 < t_s < 4 \times 10^5 \text{ seconds} \qquad (7.2)$$

$$f = 8.70300 \times 10^{-1} t_s^{-0.4255} \qquad \text{for } 4 \times 10^5 < t_s < 4 \times 10^6 \text{ seconds} \qquad (7.3)$$

This is coded into the STAR-CCM+ fluid dynamics modeling package as a field function

coded as:

```
($Time < 400)?-6.14575E-3*log($Time)+0.060157:(($Time < 4E5) ?
1.40680E-1*pow($Time,-0.286):(($Time<4E6)?8.70300E-1*pow($Time,-0.4255):0))
```

Determining the heat input into the FHR from the core is required to establish the boundary condition for the operation of the BDBA system.

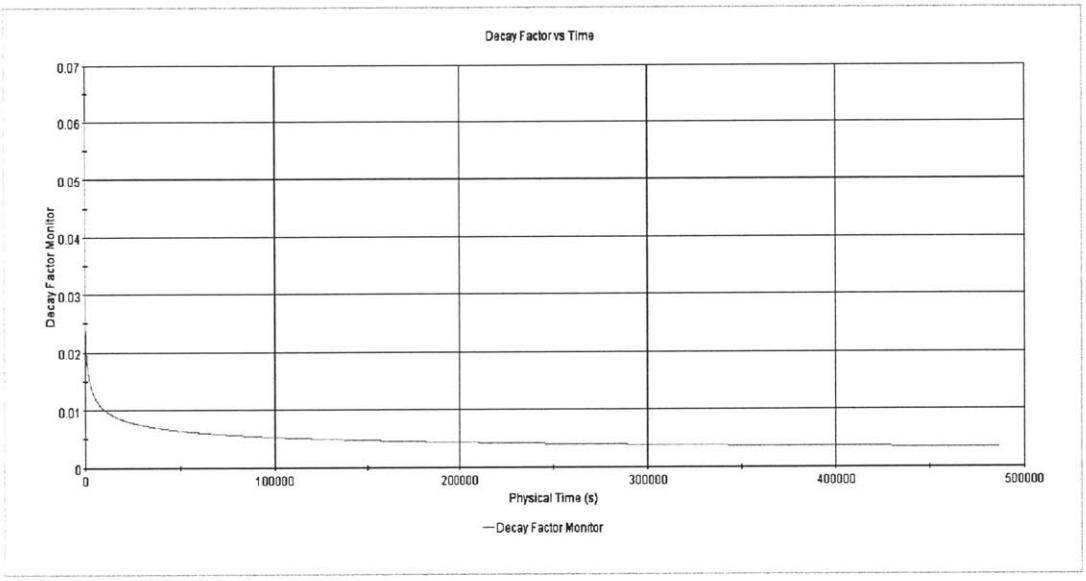

Figure 7.1: Decay Heat Fraction vs Time.

For the first iterations of FHR core decay heat, a value of 5×10^7 W/m^3 was taken initially, based on the reasoning discussed in the previous chapter. However, because of the need to set up core convective flow, both an axial and a radial cosine flux distribution were built into the volumetric heat source of the core. Thus, the core is modeled as flibe salt with a volumetric heat source energy condition with the data listed in Table 7.1. Note

Description	Value
Maximum Heat Source	5×10^{7} W/m^{3}.
Axial Distribution	$(\pi/2)\cdot\cos(\frac{\pi}{2}\frac{y-3.05}{L=6.9})$
Radial Distribution	$(\pi/2)\cdot\cos(\frac{\pi}{2}\frac{x}{0.95})$

Table 7.1: Volumetric Heat Source Energy Distribution in the Core.

that the axial and radial distribution factors were multiplied by $(\pi/2)$, because the average value of the axial and radial distribution is a factor of $\pi/2$ less than the peak value.

Given that this heat source is the design operating condition of the plant, it is continuously multiplied by the decay fraction in the simulation that is pictured in Figure 7.1. The volumetric heat source distribution is illustrated in Figure 7.2. Note that the areas surrounding the core are all dark blue indicating no heat generation in any area except the core. Closer inspection of the core shows that axial heat distribution with maximum at the bottom of the core (starting at 3.05 meters above the ground level) to zero at the top of the core ($L = 6.9$ meters higher). Similarly, the radial distribution shows maximum energy in the center of the core reaching zero at the $R = 0.95$ meter boundary. In reality, this will be a function of fuel loading and design, and usually will incorporate an *extrapolation distance* where the flux would reach zero if the shape of the energy distribution were extended outside the core such that it does not actually reach zero in the core itself.

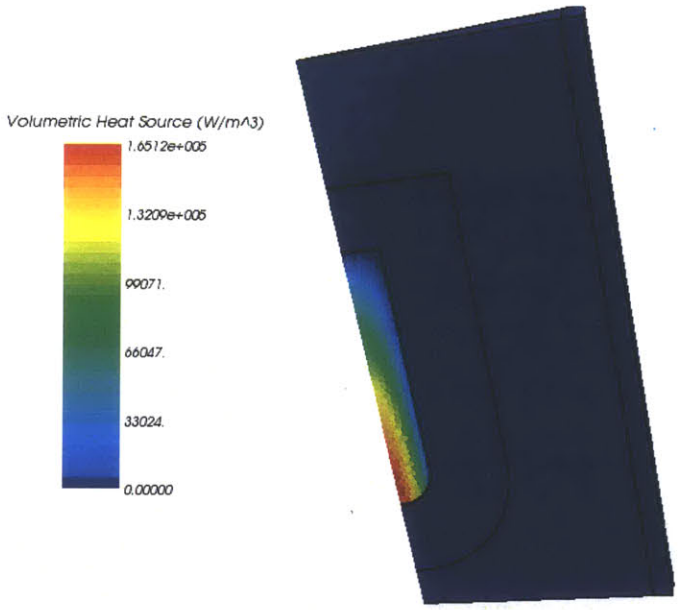

Figure 7.2: Volumetric Heat Source Distribution in FHR.

7.2 Maximum Salt Temperature Boundary Condition

The BDBA salt column is a significant absorber of decay heat. During normal operations, it is expected to remain near atmospheric temperature (approximately 25°C) because of the insulation between the vessel and the steel liner in addition to active silo cooling system that will be adjacent to both the BDBA salt column and the concrete silo.

During a reactor accident, the heat flux from the air cavity will be driven into the steel liner and into the BDBA salt. For the first many hours of the accident sequence, the salt will absorb heat through a rise in temperature, absorbing 1620 Joules for every degree Celsius per kilogram. Upon reaching it liquidus temperature of 452° C, the salt will need to absorb the latent heat of fusion, which is 1.62×10^6 J/kg for FLiNaK. During the melting process, the salt will remain at 452° C, and with a large reservoir of BDBA salt

above the FHR vessel to replenish any liquified salt that enters the air cavity, the BDBA salt column becomes a 452° C constant temperature boundary upon reaching this liquidus temperature.

7.3 Initiating FLiNaK Circulating Flow in the Air Cavity

As discussed in section 6.3, the FHR's BDBA system is modeled as a geometrically static system. Further iterations will need to show the dynamic movement of the BDBA salt. Based on the geometry of the air cavity at the bottom of the FHR, with a 6 meter radius and a height of 1 meter until the bottom of the steel vessel is reached, at least $\pi r^2 h = \pi(6)^2(1) = 113\,\mathrm{m}^3$ of BDBA salt will need to melt into the cavity until the salt even begins to come into contact with the very bottom of the vessel. The amount of salt that is expected to melt will be monitored and is discussed in Section 9.3

7.4 Expected Temperatures and Pressure in the System

The FHR system is expected to operate at atmospheric pressure. The reactor coolant operating temperature is expected to be near 700° C [7]. The core flibe, the core vessel, and the buffer salt should be nearly isothermal during reactor operations. This was selected to be just above 700° C (1000 K) for the initial conditions. The silo cooling system and the surrounding earth at atmospheric (25° C) conditions should keep the silo near 25° C, and this was chosen for the initial temperatures for the silo and the earth.

During normal operation, the insulation between the air cavity and the steel liner should keep the air between the vessel temperature of 700° C, and the atmospheric temperature. 450° C was selected as the initial air temperature for the air, and the steel liner was initialized at 327° C (600 K).

The BDBA salt is in contact with the active silo cooling system during normal operation. However, as discussed in Chapter 4, complete failure of the silo cooling system is assumed for the simulations in this report. Furthermore, the simulation commences after a complete loss of insulation, as the insulation is not built into the model. The BDBA salt temperature will rise because of (1) a loss of silo cooling, and (2) increased heat input due to insulation failure. Therefore, an initial temperature of 300° C was used as a BDBA salt initial temperature. BDBA salt location will affect the BDBA sequence. This analysis uses BDBA salt outside the steel liner as described in Chapter 6. Another option is discussed in Appendix D.4.

There are many questions that still remain in the FHR core design and the geometrical design of the FHR system. Given a primary coolant temperature target of near 700° C, and a substantial amount of liquid salt surrounding the core, the 1000 K initial temperature for the core and salts is reasonable, while the air and vessel temperatures are approximations. Upon initiating the accident in the STAR-CCM+ modeling software, the temperatures for the geometry between the core (which will rise in temperature due to the decay heat input) and the outer boundary will stabilize as the heat fluxes balance each other.

The initial temperature snapshot is illustrated in Figure 7.3.

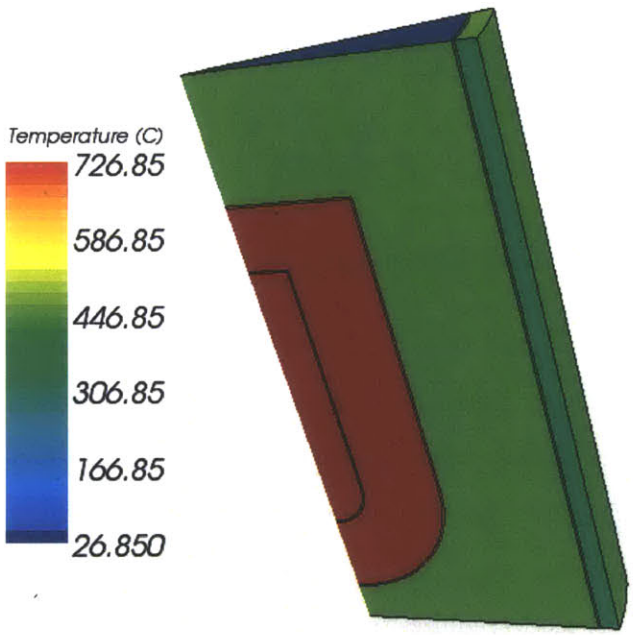

Figure 7.3: Initial FHR Temperature Schematic.

Chapter 8

Physics Models

8.1 Time Step and Unsteady Solver

The problem being simulated dictates the choice between steady and unsteady models. Situations that are clearly time-dependent and require an unsteady model include time varying boundary conditions. In the case of the FHR, the time-varying decay heat is the source of energy being distributed to the reactor vessel. This leaves the modeler no choice but to use an unsteady model.

Using an unsteady model requires that transient temperature distributions are obtained by marching out in time using intervals of Δt in any type of solver. There are two methods of solution: an explicit and an implicit method. An explicit method is a solution method in which the unknown mesh temperature of each interior node is determined exclusively by the known temperature at the previous time [1, p. 331].

The Explicit Unsteady model is only available with a coupled energy model. It is only compatible with the inviscid and laminar viscous regime models. The choice between the implicit and explicit approaches is based on the time scales of physical interest.

Compared to the explicit method, implicit methods have the significant advantage of being unconditionally stable; that is, there are no restrictions on Δx and Δt that cause the solution to introduce numerically-induced oscillations and divergence from steady state conditions [1]. However, the *accuracy* of the solution could depend on the choice of Δt; this time step should be chosen such that results are independent from reductions in value of Δt.

8.1.1 Implicit Unsteady Modeling

The implicit unsteady approach is appropriate if the time scales of the phenomena of interest are related to some relatively low frequency external excitation like time-varying boundary conditions (as seen in the FHR decay heat input).

In the implicit unsteady approach, each time step involves some number of *inner iterations* to converge the solution for that given instant of time. These inner iterations can be accomplished using implicit spatial integration or explicit spatial integration schemes. The modeler must specify the physical time-step size that is used in the outer loop. The integration scheme marches inner iterations using optimal pseudo-time steps that are determined by the modeler.

With the implicit unsteady approach, the modeler is required to set the physical time step size and the number of inner iterations at each physical time step. The transient phenomena being modeled generally governs the physical time-step size. As indicated in Reference [1], a good way to determine the physical step size is to ensure that results are independent of step size.

Figure 8.1 shows the base FHR case run for 360,000 seconds (100 hours). This research is focused on determining the maximum peak temperature that will be observed in an FHR during a beyond design basis accident. Here, starting with a temperature of 727°C (1000

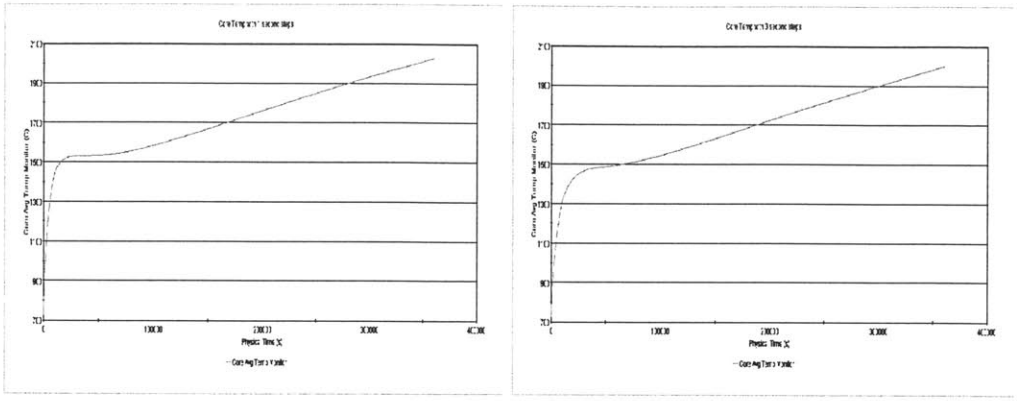

(a) 1 sec (b) 3 sec

Figure 8.1: Core Average Temperature vs Time Step Size.

Time Step (sec)	T_{start} (C)	T_{end} (C)	ΔT (C)
1	727	2025	1298
3	727	1998	1271
% Difference $= \frac{1298-1271}{1298}(100) = 2$			

Table 8.1: Difference in 1 and 3 Second Time Steps on Core Temperature.

K) in the core in both cases, Table 8.1 shows the results for decreasing the time step by a factor of three.

The difference between the 3 second and 1 second time step shows a difference in temperature of 2%. While lowering the time step from 3 to 1 sec does result in a slightly different temperature, the small difference is noise compared with the approximations made in the FHR geometry, core modeling, power density, and other yet-unknown conditions in the FHR. Nevertheless, in order to capture most of the effects of the first few hours of the accident as temperatures are expected to oscillate to find an "equilibrium" condition due to initial approximations on the operating temperatures, 1 second time intervals are used for the first 14400 seconds (4 hours) of the accident. Then, given the small error introduced by increasing the time step to 3 seconds, the rest of the accident sequence proceeds in the

simulation with 3 second time steps.

8.1.2 Time Stepping and Inner Iterations

The number of inner iterations per physical time-step is harder to quantify. Generally, STAR-CCM+ recommends a modeler determine this number by observing the effect that it has on results. Select a number of inner iterations, plot a monitor for one or more specific quantities against iteration, and see whether these monitors are converging within each time-step.

Smaller physical time-steps generally mean that the solution is changing less from one time step to the next; fewer inner iterations are then required. There is an optimal balance of time-step size and number of inner iterations for a given problem and desired transient accuracy.

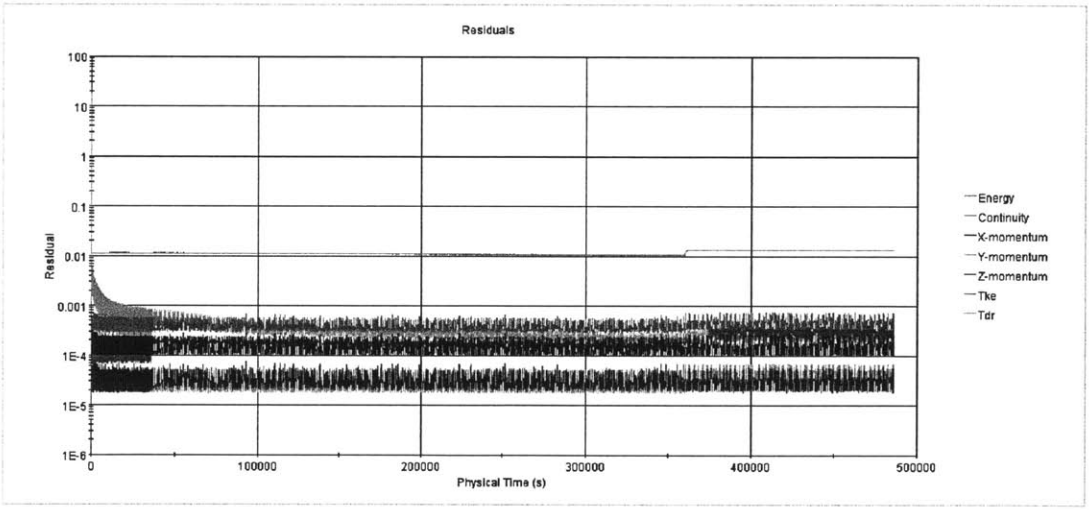

Figure 8.2: Residuals for the base FHR Case.

This FHR model showed that the residuals (shown in Figure 8.2) on each time step converged within 5 inner iterations, which was selected for the duration of the simulation.

8.1.3 Coupled and Segregated Models

A coupled energy model is an extension of the Coupled Flow model. Together they solve the conservation equations for mass, momentum, and energy simultaneously using a time- (or pseudo-time-) marching approach. This formulation is more robust for solving compressible flows and flows with dominant source terms, such as buoyancy.

A Segregated Flow Model solves the flow equations (one for each component of velocity, and one for pressure) in a segregated, or uncoupled, manner. The linkage between momentum and continuity equations is achieved with a predictor-corrector approach. This model has its roots in constant density flows. However, it can handle mildly compressible flows and some natural convection flows.

Choosing between coupled and segregated flow models depends on the physical phenomena and accuracy desired. The segregated algorithm uses far less memory (that is, computational power and time) than the coupled flow. The disadvantages are that the coupled flow yields better results for compressible flows, and high-Rayleigh number convection. However, the segregated flow model is known to perform reasonably well for mildly compressible flows. Furthermore, for high Rayleigh-number flows, it is known that no model can capture many of the flow effects [4]; thus use of the coupled flow solver for the first iteration and approximation of the FHR is not an efficient use of computing resources. Therefore, the *segregated* flow model with the implicit unsteady model was used for all regions of the FHR STAR-CCM+ model.

8.2 Capturing Thermophysical Property Variations

As discussed in Chapter 2, FLiNaK salts were used in the simulation modeling of the FHR. In addition to the reasons discussed in that chapter, a significant benefit is that the

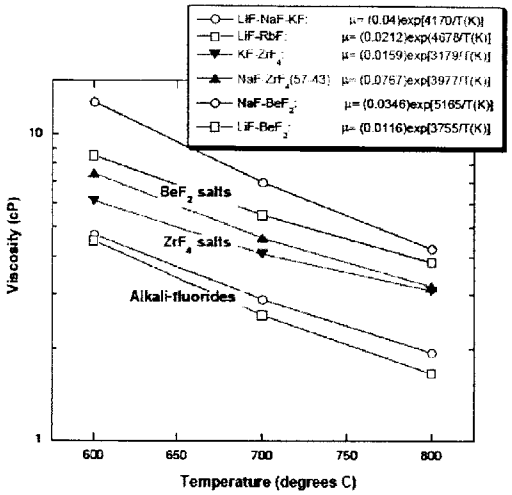

Figure 8.3: FLiNaK Salt Viscosity from Experiment [30].

properties of FliNaK have been extensively determined for a wide range of temperatures, including the high temperatures of interest, for use in this model.

FLiNaK Salt The experimental methods used to estimate the density of FLiNaK salt have been shown to be fairly accurate over a wide range of temperatures. Reference [30] has determined the formula for the density of FLiNaK in g/cm^3 to be

$$\rho_{\text{FLiNaK}}\,(\text{g/cm}^3) = 2.530 - 7.3 \times 10^{-4} \cdot T(^\circ C) \tag{8.1}$$

A conversion of Celsius to Kelvin was made, and the following field function was input as the FLiNaK density function in the STAR-CCM+ modeling software:

```
1000 · (2.729 - 0.00073*$Temperature)
```
(8.2)

Likewise, viscosity was taken from Figure 8.3 and converted from cP to Pa-s and entered

into the software as:

```
(0.04)·(0.001)· exp(4170/($Temperature))
```
(8.3)

The remainder of the pertinent FLiNaK properties were taken from Table 8.2

Salt	Molar Weight (g/mol)	T_{melt}	k (W/m-K)	c_p (cal/g-C)
LiF-NaF-KF	41.3	454	0.68	0.387

Table 8.2: Properties of FLiNaK Salt [30].

Air Density The motion of the air in the reactor cavity between the vessel and the liner is a key part of convection heat transfer from vessel to liner until the BDBA salt is sufficiently heated to flow into the reactor cavity. Therefore, capturing the effect of fluid motion is important in the cavity. Since there is nothing to force any convection in this region, the flow must come from density gradients.

The air is treated as an ideal gas. Since the airflow is driven by heat transfer, the air properties are mainly functions of temperature. These temperature-influenced properties will cause the fluid motion. Since the density variation is not large over any given period of time, the density may be treated as constant in the unsteady and convection terms, and treated as a variable in only the gravitational term [5]. This is termed the *Boussinesq approximation* and is used in the model of air. The approximation manifests itself in the conservation of momentum equation, which for two-dimensional Cartesian coordinates is given by

$$u\frac{\partial u}{\partial x} + v\frac{\partial u}{\partial y} = g(\frac{\Delta\rho}{\rho}) + \nu\frac{\partial^2 u}{\partial y^2} \tag{8.4}$$

where $\Delta\rho = \rho_\infty - \rho$ is the density difference between the heated surface and the free stream

air.

By recognizing the term $g(\frac{\Delta\rho}{\rho})$ as the buoyancy force per unit mass, one recognizes the origination of flow resulting from the ρ variable. If density is only a function of temperature, one can quantify the density change as a result of a volumetric thermal expansion coefficient:

$$\beta = \text{Volumetric Expansion Coefficient} = -\frac{1}{\rho}\left(\frac{\partial\rho}{\partial T}\right)_p \tag{8.5}$$

The subscript p indicates the process occurs at constant pressure, which is approximately true for the atmospheric pressure FHR. By approximating Equation 8.5 to

$$\beta \approx -\frac{1}{\rho}\frac{\Delta\rho}{\Delta T} = -\frac{1}{\rho}\frac{(\rho_\infty - \rho)}{(T_\infty - T)} \tag{8.6}$$

then

$$(\rho_\infty - \rho) \approx \rho\beta(T - T_\infty) \tag{8.7}$$

and the momentum equation in the x-direction (gravity direction) becomes

$$u\frac{\partial u}{\partial x} + v\frac{\partial u}{\partial y} = g\beta(T - T_\infty) + \nu\frac{\partial^2 u}{\partial y^2} \tag{8.8}$$

Determining β for an ideal gas results from using $\rho = p/RT$ so

$$\beta = -\frac{1}{\rho}\left(\frac{\partial\rho}{\partial T}\right)_p = \frac{1}{\rho}\frac{p}{RT^2} = \frac{1}{T} \tag{8.9}$$

where T is the absolute temperature in Kelvin [1]. Thus, in the simulation, the Boussinesq approximation is used. The thermal expansion coefficient for the Air Continuum is set to `1 / $Temperature` .

Density (kg/m^3)	`2330 - 0.42*$Temperature`
Viscosity (Pa s)	`1.16E-4 * exp(3760/$Temperature)`

Table 8.3: Flibe Property Field Functions.

Flibe Properties Modeling the circulation of the primary coolant requires a density gradient. Prior research on flibe salt between its peritectic and eutectic points (where the melting point is lowest) shows the following correlations for the temperature range of interest [9]:

$$\rho_{\text{flibe}}\,(\text{kg/m}^3) = 2330 - 0.42 \cdot T(K) \tag{8.10}$$

$$k_{\text{flibe}} = 1.0\,\text{W/m-K} \tag{8.11}$$

$$c_{p,\text{flibe}} = 2380\,\text{J/kg-K} \tag{8.12}$$

$$\mu\,(\text{kg/m-s}) = 1.16 \times 10^{-4} \exp(3760/T(K)) \tag{8.13}$$

These values and correlations were used in the STAR-CCM+ simulation, with field functions created for flibe that are listed in Table 8.3.

8.2.1 Turbulence

The Realizable Two-Layer K-Epsilon turbulence model combines the Realizable K-epsilon model with the two-layer approach. The coefficients in the models are identical, but the model gains the added flexibility of an all y^+ wall treatment.

The all-y^+ wall treatment is a hybrid treatment of the low-y^+ that has a properly resolved viscous sublayer (and is thus appropriate for low-Reynolds numbers flows) and the high-y^+ treatment that assumes the near-wall cell lies within the logarithmic region of the boundary layer. It attempts to emulate the high-y^+ wall treatment for coarse meshes

(that are not adequately resolved at the wall) and the low-y^+ wall treatment for fine meshes.

There are a few types of two-layer formulations that are permitted in the STAR-CCM+ modeling package. Two are shear-driven: a model by Wolfstein [31] and one by Norris-Reynolds [21]. Neither of these models are appropriate for buoyancy driven flows that are seen in the liquid buffer salt or in the air cavity. Rather, a buoyancy driven two-layer formulation must be used. The modeling package includes the model proposed by Xu [32] that is appropriate for use with buoyancy.

8.3 Buoyancy

The FHR is completely passive during a BDBA; that is, there is no forced convection present. Convection motion will be due to buoyancy forces within the fluid. Buoyancy is the result of the combination of a fluid density gradient and a body force proportional to density. The only body force of concern in the FHR model is gravitational.

Like forced convection, knowledge about the temperature and velocity profiles results from the momentum and energy equations that were derived from the conservation of mass, momentum, and energy equations. Inertia and viscous forces are important to understand in order to capture effects of the flow. However, unlike the forced convection case, the FHR relies on buoyancy forces to drive the flow.

By nondimensionalizing Equation 8.8, it can be demonstrated that two important factors in determining free convection fluid flow are the *Grashof number*:

$$Gr_L \equiv \frac{g\beta(T_s - T_\infty)L^3}{\nu^2} \tag{8.14}$$

which is the ratio of buoyancy forces to viscous forces (analogous to the ratio of inertial to viscous forces in the Reynold's number seen in forced convection) and the Prandtl number;

these two factors form an important product known as the *Rayleigh number*:

$$Ra = Gr\,Pr = \frac{g\beta(T_s - T_\infty)L^3}{\nu\alpha} \tag{8.15}$$

Accurate modeling of free convection flows for vertical plates is limited by a critical Rayleigh number of 10^9 [1]. For the air cavity with a vertical length of 14.6 m, Rayleigh numbers are expected to be very high due to the large ΔT across the boundary layer. With a 100°C ΔT and a cavity free stream temperature of 700 K, one would see a Rayleigh number significantly above 10^9:

$$Ra_{\text{FHR air cavity}} = \frac{(9.81\,\text{m/s}^2)(100\,\text{K})(14.6\,\text{m})^3}{(1.22\times10^{-4}\,\text{m}^2/\text{s})(1.69\times10^{-4}\,\text{m}^2/\text{s})(973\,\text{K})} \approx 1.5\times10^{11} > 10^9 \tag{8.16}$$

Due to the significantly higher than critical Rayleigh number, hydrodynamic instabilities will arise. These disturbances will lead to significantly turbulent flow. In the case of the FHR, this will greatly aid in the heat transfer through the thermal boundary layer. In reality, a greater heat transfer coefficient will be present than simulations will predict, leading to increased heat transfer from core to the liner and BDBA salt. Unfortunately, modeling of free convection systems with high Rayleigh numbers remains critically complex and is only able to be accurately predicted in very limited cases discussed in Chapter 12.4.1. Therefore, emphasis for the FHR free convection flow will need to be placed on experimental results of hydrodynamically similar models.

Chapter 9

Results: Base Case

The base case was run with the 6 meter radius air cavity as shown in Figure 9.1. The effects of changing the silo size are described in the next chapter. This case had no radiation modeling built into the simulation. Radiation and the results of modeling with radiation are discussed in Chapter 11. This base case was run to see if (1) it is possible to prevent a fuel melt without relying on radiative heat transfer and (2) to see how the heat is distributed by the air in the cavity.

As discussed earlier and as shown in Figure 9.1, the BDBA salt outer radius is modeled as a constant temperature boundary with the temperature equal to the FLiNaK liquidus temperature of 452° C (725 K). This is the model that is shown in Figure 9.1(a). Once the FLiNaK temperature reaches 452° C, there will be *no further rise* in its temperature until it absorbs enough heat to overcome its latent heat of fusion. As discussed in Section 6.4, the accurate tracking of the 2-phase FLiNaK salt is computationally prohibitive. Therefore, a different approach to the model is used once this condition is reached.

Figure 9.1(b) shows the base case model after the BDBA salt reaches an average of 452° C. Notice that the BDBA salt is removed from the model, and the outer boundary

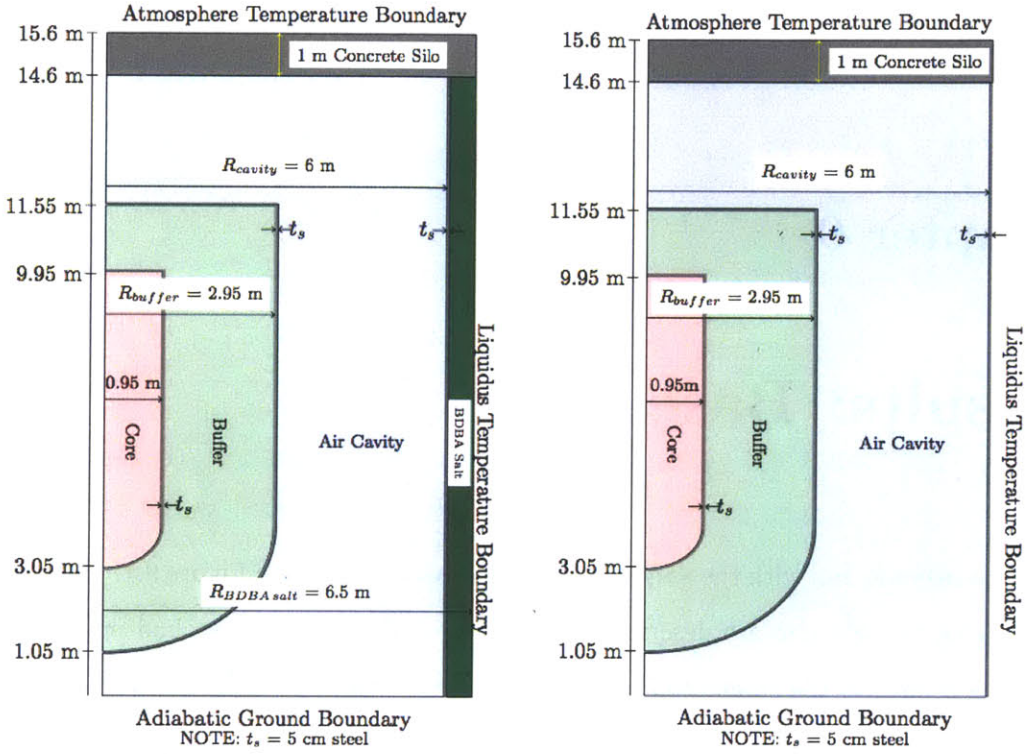

(a) Base Case Model.

(b) Base Case Model after BDBA Salt Reaches Liquidus Temperature.

Figure 9.1: Modeling of the Base Case.

t_{liquidus} = 281190 seconds (78 hours).
Component Average Temperatures

	°C	K
Core	1120	1393
Core Vessel	1078	1351
Buffer	1027	1300
Steel Vessel	1023	1296
Air	680	953
Liner	522	795
BDBA Salt	452	725

Table 9.1: Component Temperatures when BDBA Salt Average Temperature = 452° C

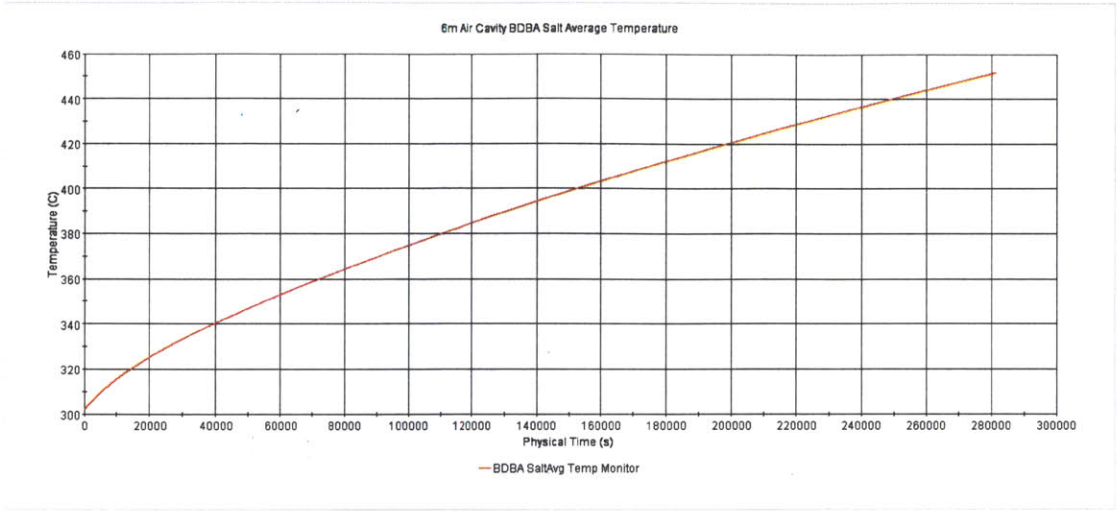

Figure 9.2: Base Case Average BDBA Salt Temperature vs Time.

of the steel liner is held at a constant temperature (452° C). This requires restarting the simulation after removing the BDBA salt boundary from the model.

The BDBA salt is of special importance to monitor because this becomes a significant heat sink for a long period of time. The FHR accident sequence outer boundary modeling in the STAR-CCM+ program is dependent on tracking the average BDBA salt temperature reaching its liquidus temperature of 452°C. This can be seen in Figure 9.2. The BDBA salt average temperature reaches 452° C at 281190 seconds (78 hours), and the average temperatures of each of the components is listed in Table 9.1. The simulation was re-started with the conditions just discussed at the 281190 second point (this affects the amount of decay heat power remaining).

A striking (and positive) result of this base case shows that convection is extremely helpful in the creation of *isothermal temperature conditions* in the core's flibe salt and in the FLiNaK buffer. Figure 9.3 shows the temperature distribution of the FHR salts in the core and in the buffer. Of note is the minimum and maximum temperature in each of

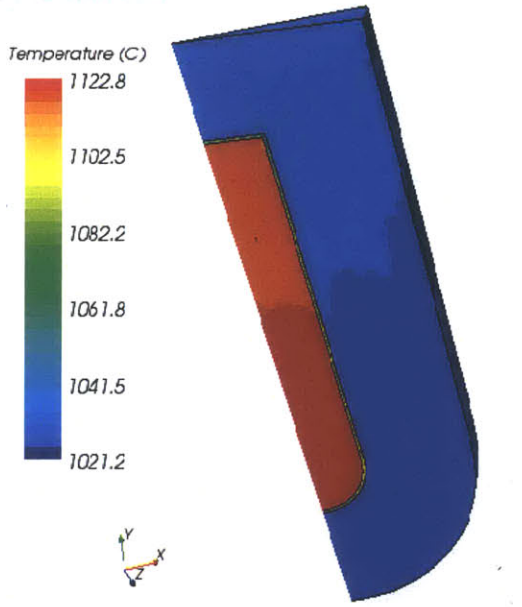

Figure 9.3: Temperature Profiles in the Core and Buffer.

the regions. There is a 21°C maximum difference throughout the entire core and a 16 °C temperature difference in the buffer salt tank. These nearly isothermal conditions indicate excellent heat distribution in the core and in the buffer. The creation of nearly isothermal conditions is indicative that the core and buffer salt are efficiently transferring heat to the FHR vessel where it undergoes heat transfer with the air cavity and ultimately to the environment.

However, heat transfer is severely limited by the amount of conduction and convection that can occur outside the FHR outer vessel through the air. In the case of the air cavity, the thermal conductivity is quite small and the convection heat transfer coefficient is nearly negligible. Figure 9.4 provides an overall temperature profile of the entire FHR system.

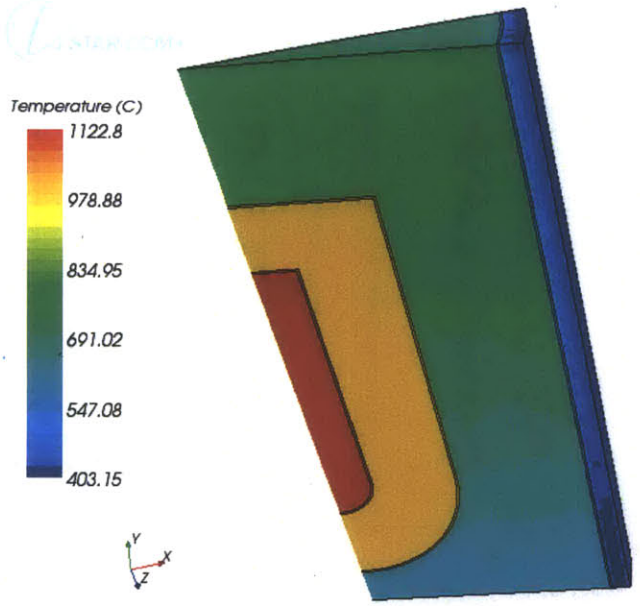

Figure 9.4: Overall FHR Temperatures When the Average BDBA Salt is at Liquidus Temperature.

The core and buffer salt tanks are nearly isothermal. Unfortunately, the air cavity sees a significant drop in temperature from the steel vessel to the outer steel liner; this will be discussed in the forthcoming paragraphs.

Figure 9.5 shows the convective vectors after 281190 seconds (78 hours) (when the average BDBA salt temperature reaches 452° C). The air cavity realizes a high amount of convective flow with velocities near 1 m/s (Figure 9.5(a)). Due to the extensive temperature difference between the metal buffer vessel, operating near the core temperature, and the steel liner, much closer to normal atmospheric temperatures, air will convect in the general pattern shown with a significant upward current surrounding the buffer vessel and a falling current as the air gives up heat to the silo wall. Intuitively, this should cause significant heat transfer on the inner wall of the air cavity (which interfaces with the steel vessel)

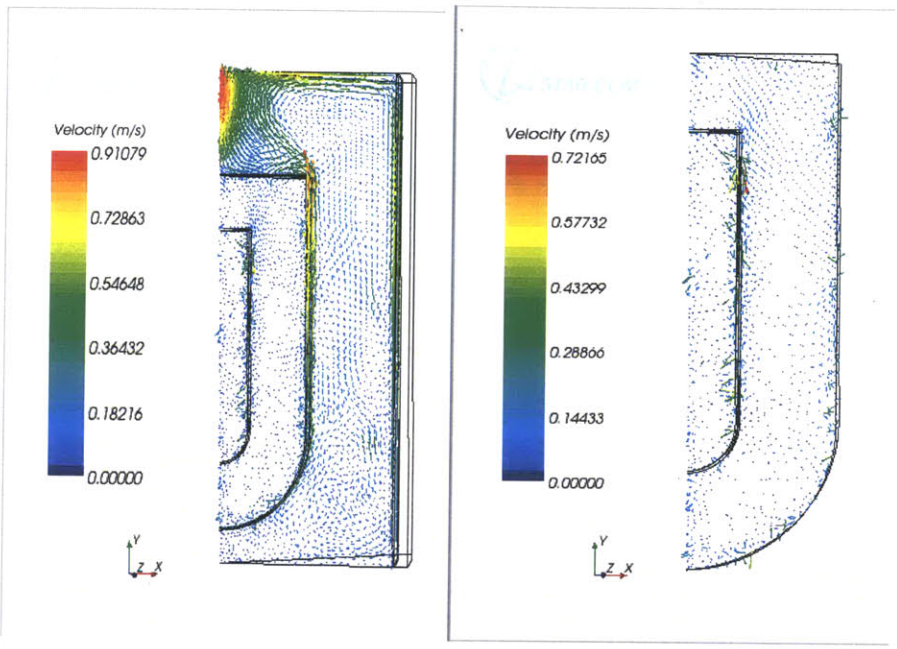

(a) Convective driven velocity vectors (BDBA system).

(b) Convective driven velocity vectors (BDBA salts).

Figure 9.5: Convective Currents in the Core and BDBA Salt.

and cooling on its outer wall (interfacing with the steel liner); these flows are separated by a significant enough distance to allow upward and downward convective flow without significant interference. The air should be able to convect heat away from the FHR vessel to the steel liner (outer radius) efficiently.

However, the heat transfer coefficient of *naturally convected* air is expected to be low. Despite the limitations of predicting high-Rayleigh number flows, a rough approximation calculated in Appendix A indicates that the heat transfer coefficient is likely to be near 5 W/m^2-K. The STAR-CCM+ composite model shows even less favorable predictions for the heat transfer coefficient as shown in Figure 9.6. The low ability of the air to convectively transfer heat away from the FHR outer vessel to the steel liner (and ultimately to the BDBA

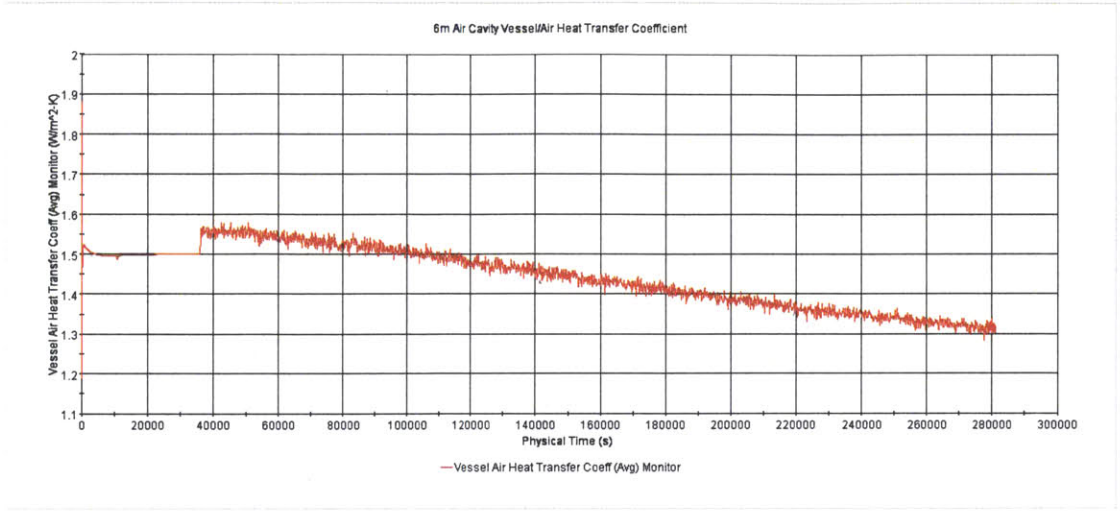

Figure 9.6: Air/FHR Outer Vessel Heat Transfer Coefficient vs Time.

salt) appears to be the most limiting aspect of the FHR BDBA heat removal system. The low convective heat transfer coefficient–coupled with the low thermal conductivity of air (about 0.067 W/m-K at atmospheric conditions)–results in a large ΔT from FHR vessel to steel liner.

Air currents directly above the buffer vessel will experience an unpredictable flow. The buffer vessel will heat the air directly above it, causing a marked decrease in air density and upward current. However, as the air reaches the upper boundary of the air cavity and comes in contact with the near environmental temperatures, it will rapidly compress and want to fall. There will be a competing front of air between the vertically rising flow from the vessel and the falling flow from the upper boundary. This is likely to set up a stagnation region which will need to be resolved by experiment and/or geometry modification.

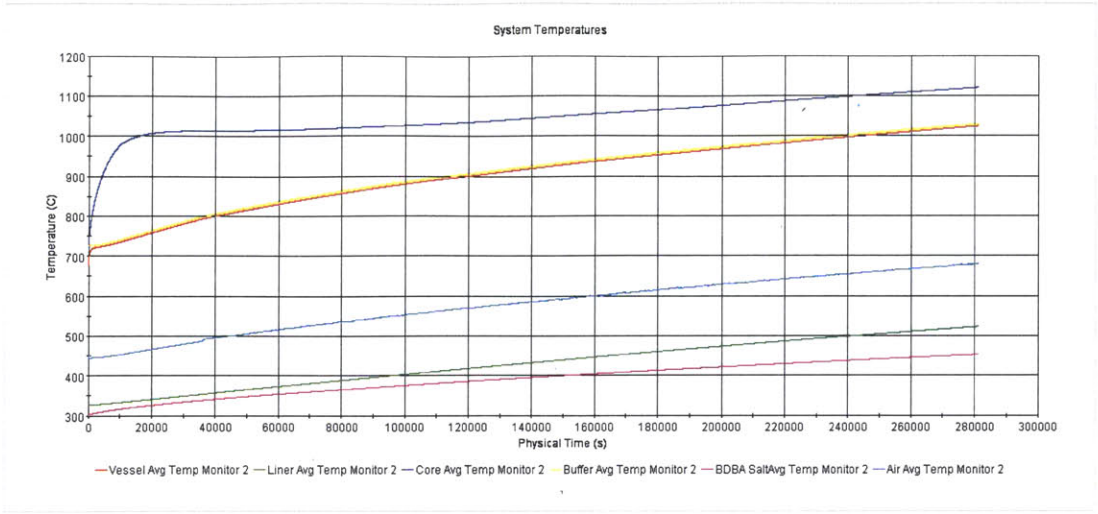

(a) System Temperatures during first $t = 281190$ sec (78 hours).

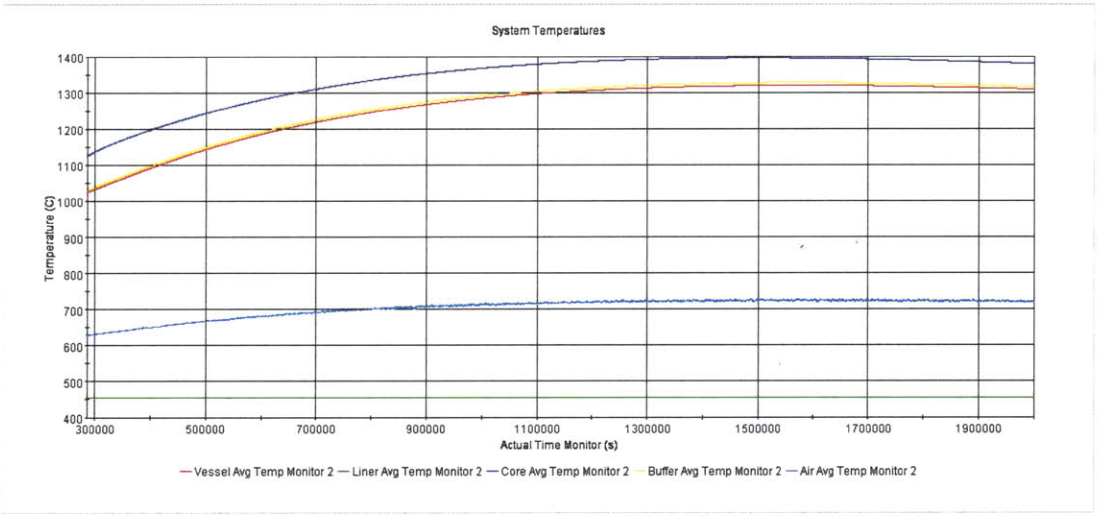

(b) System Temperatures after $t = 281190$ sec (78 hours).

Figure 9.7: Base Case System Temperatures vs Time.

9.1 System Temperatures

The overall system temperatures during accident progression are illustrated in Figure 9.7. Figure 9.7(a) is the first $t = 281190$ seconds until the average BDBA salt temperature

reaches 452° C. Figure 9.7(b) spans from $t = 281190$ seconds until 2×10^6 seconds (23 days). Note that the vastly different time scales of each of the subfigures results in perceiving incongruent slopes in the temperatures—especially of the core, buffer, and vessel—despite the continuous sequence of events.

Initial Heat Transfer Dynamics

The most crucial time in the accident progression is the first 10^5 seconds. This is when the core temperature is being driven upward rapidly by the significant decay heat. Recall that the conservation of energy requires any volume to store the net energy that is not transferred out from inward heat transfer and/or internal heat generation:

$$\dot{E}_{in} + \dot{E}_g - \dot{E}_{out} = \dot{E}_{st} \tag{9.1}$$

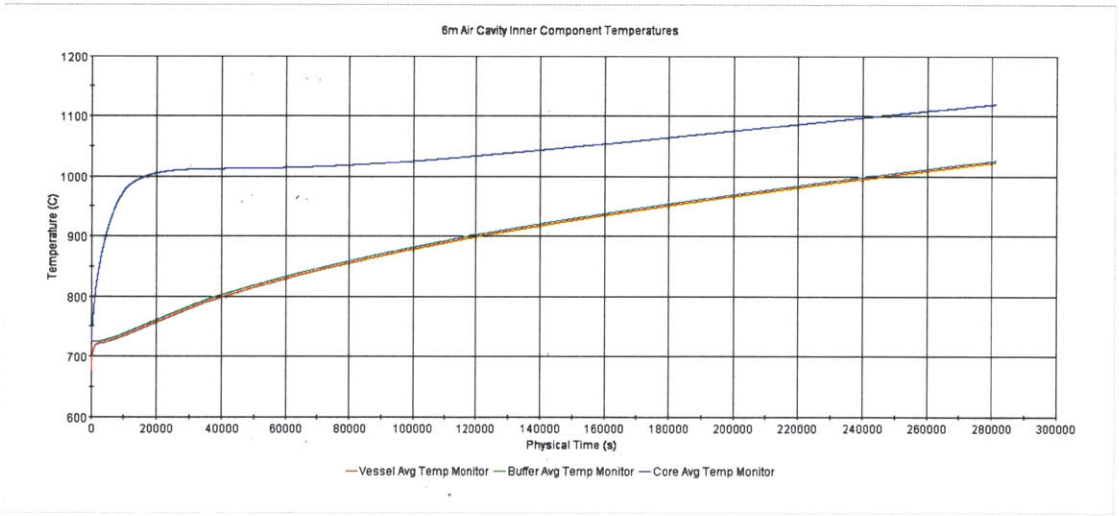

Figure 9.8: Core, Buffer, and Outer FHR Vessel Temperatures during first 281190 seconds (78 hours).

During the FHR's normal operation, temperatures will have equalized in the system.

For the core, core vessel, buffer salt tank and buffer vessel, given the liquid and solid interactions with convective current, this is expected to be nearly isothermal. Heat transfer is driven by ΔT. At the initiation of an accident, $\dot{E}_{out}$ of the core through the secondary coolant system (gas turbine) heat sink will be lost while $\dot{E}_g$ will decay slowly at first. With low ΔT between the core and the surrounding components, energy transfer out of the core is not rapid, and the core experiences a very large storage rate, $\dot{E}_{st}$, which manifests itself as a significant increase in temperature of the core.

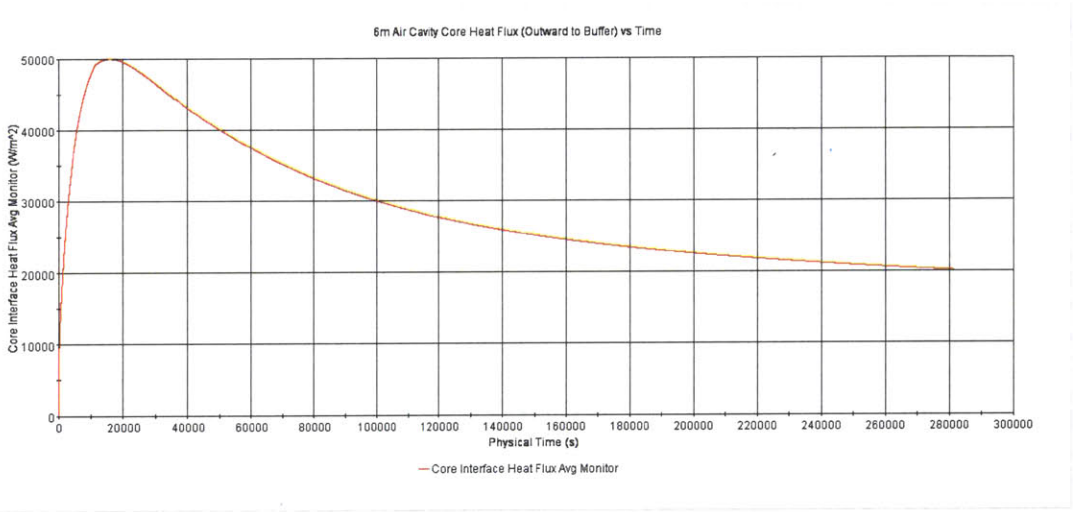

Figure 9.9: Heat Flux at the Core/Buffer Interface for first 281190 seconds (78 hours) (W/m^2).

Figures 9.8 and 9.9 show the FHR's response to a beyond design basis accident–that is, *no* active cooling systems and no silo cooling of any type–during the first 281190 seconds (78 hours) until the average BDBA salt reaches 452° C. These figures show the same phenomenon in two different manners.

Figure 9.8 demonstrates that a ΔT is required between the core and its surroundings to have heat transfer out of the core. During normal operation, the core and buffer will be expected to be nearly isothermal due to the convective currents discussed earlier *and*

because of the primary heat transfer from the core through the secondary cooling system (to power and steam generation). Therefore, the first part of the beyond design basis accident is the *establishment of a temperature difference* from the core to the surrounding buffer and FHR outer vessel. The first approximately twenty thousand seconds establish a maximum of 260° C temperature difference between the core (flibe) and the buffer salt. The temperature difference between the core and buffer stabilizes at approximately 100° C after nearly 2×10^5 seconds. This ΔT remains nearly constant throughout the entire accident scenario as seen as well in Figure 9.10.

Figure 9.9 shows this same dynamic by monitoring the heat flux at the core/buffer interface (in W/m^2). The core heat flux is nearly zero initially, when there is very little ΔT between the core and buffer. The heat flux leaving the core rises rapidly during the first 20,000 seconds until that maximum ΔT of nearly 260° C is established. The heat flux then diminishes and appears to approach an asymptotic value as the ΔT between core and buffer approaches the nearly constant ΔT of approximately 100° C.

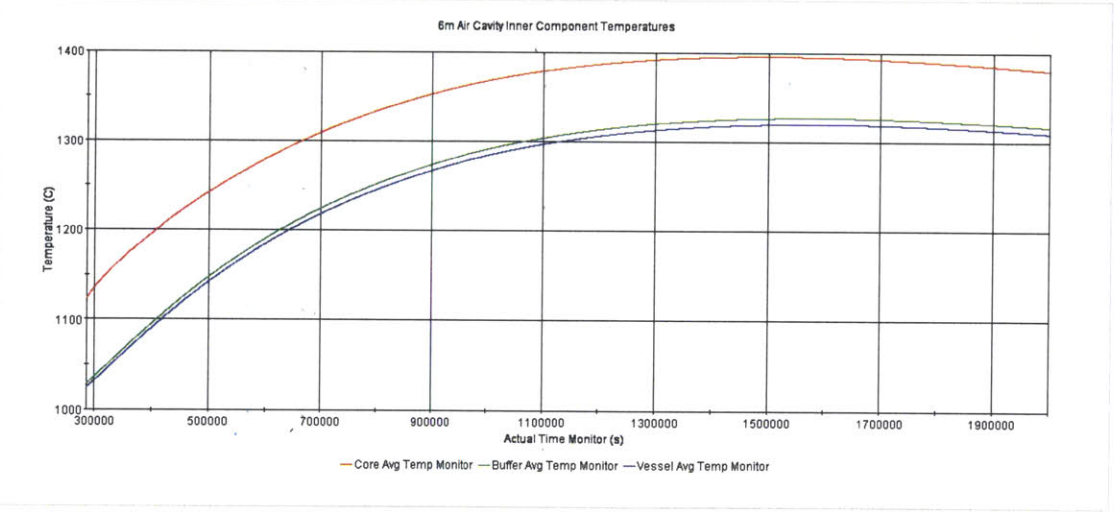

Figure 9.10: Core, Buffer, and Outer FHR Vessel Temperatures after 281190 seconds (78 hours).

9.2 Heat Transfer Outside the FHR Vessel

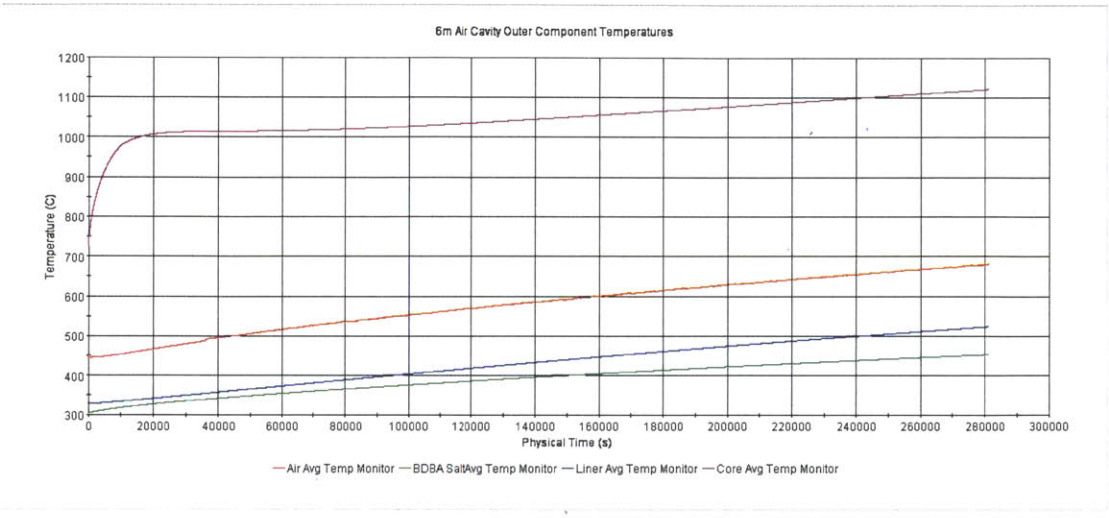

(a) Core, Air, Liner, and BDBA Temperatures during first $t = 281190$ sec (78 hours).

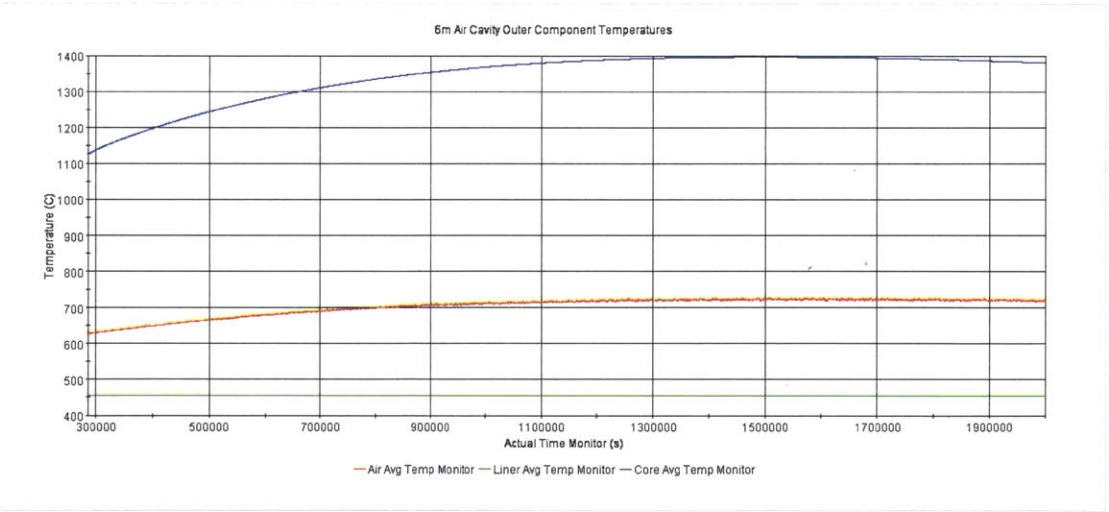

(b) Core, Air, and Liner Temperatures after $t = 281190$ sec (78 hours).

Figure 9.11: Base Case Overall System Temperatures vs Time.

Transferring heat through the air cavity remains the most significant challenge of the

FHR system. This sets up the large ΔT between the core (and FHR vessel) to the air. With a more effective heat transfer coefficient and/or thermal conductivity of the gas in the cavity, a more uniform temperature distribution would occur from the vessel to the liner. Figure 9.11 shows the large temperature difference between the hottest temperatures (in the core) and the air gap. The ΔT between the core and the air cavity approaches 600° C in the latter stages of the accident sequence. Recall that the heat in the air cavity has two pathways out as seen in Figure 9.1(b): (1) radially through the steel liner to the 452° C boundary and (2) axially upward through the 1m concrete silo barrier to the constant temperature atmosphere boundary. Therefore, as the air temperature gets hotter, especially as seen in Figure 9.11(b), the ΔT between the core and the air grows slightly, since the core continues to rise in temperature while the air's outward heat flux actually rises due to the larger temperature difference between the air cavity and both the atmosphere boundary and the BDBA salt boundary.

9.3 Maximum Temperatures and Energy Transfer

There is the design possibility of flooding the air cavity with liquid BDBA salt upon melting. The advantage to this approach is what makes the FHR design so unique. If BDBA salt melts in significant enough quality to flood at least the lower portion of the FHR buffer vessel, convective heat transfer through the BDBA salt with its much larger heat transfer coefficient will replace the convective heat transfer of air. Once this occurs with enough salt, the system should eventually equalize in a temperature near the 452°C liquidus temperature, since any BDBA salt that melts would be replenished from an external reservoir above the FHR system.

The simulation of the accident sequence with the constant temperature boundary condition at the steel liner outer boundary is run until heat transfer into BDBA salt is enough

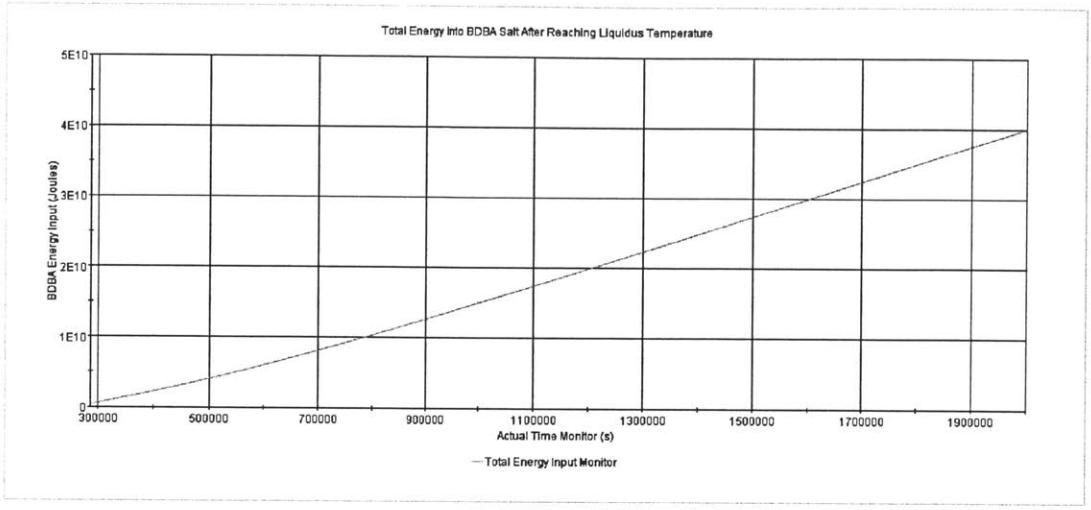

Figure 9.12: Base Case Energy of Fusion Input Into BDBA Salt.

to melt the salt to a level that rises above the hemispherical heat of the buffer vessel; that is, until it reaches the vertical cylindrical part of the vessel. Monitoring of the energy input is accomplished by setting up a time integral of the heat rate (Watts) into the BDBA salt from the time it reaches its liquidus temperature. The setup of this monitor function is described in Appendix C.

The final part of the BDBA sequence is the melting of sufficient BDBA salt to have meaningful liquid salt circulation in the lower part of the salt cavity. This is assumed to occur when the BDBA salt has melted in sufficient volume to fill the air cavity at least to the cylindrical portion of the FHR vessel (at a height of 4 meters above the base). Since the radius of the hemispherical head of the FHR vessel is 3 m and it sits 1 m above the ground level (refer to Figure 9.1(a)) and the air cavity has a radius of 4 meters, the volume that needs to melt is:

$$\pi\left(r_{\text{air}}^2 h - (0.5)\frac{4}{3}r_{\text{hemisphere}}^3\right) = \pi\left(6^2(4) - \frac{2}{3}(3)^3\right) = 396\,\text{m}^3 \tag{9.2}$$

The density of FLiNaK is approximately 2019 kg/m^3 on average, while the latent heat of fusion is 1.6×10^6 J/kg. Since 15° of the FHR system is modeled, (15/360) of this is required in the simulation to melt the salt to cause the circulation.

$$E_{\text{for circulation}} = V\rho E_{\text{fsn}} = 396\,\text{m}^3(2019\,\text{kg/m}^3)1.6\times10^6\,\text{J/kg} = 1.3\times10^{12}\,\text{J} \quad (9.3)$$

$$E_{\text{required to circulate, simulation}} = \frac{15}{360}(1.3\times10^{12}\,\text{J}) = 5.4\times10^{10}\,\text{Joules}. \quad (9.4)$$

Both Figures 9.7(b) and 9.11(b) show the system temperatures reaching a maximum in the accident scenario at 1.5×10^6 seconds without the aid of circulating salt. The crucial maximum temperature is the core temperature, which reaches 1400° C at 1.5×10^6 seconds. This is well below the fuel melt temperature of approximately 1650° C [7], and slightly below (but near) the boiling point of the flibe salt—1430° C.

Figure 9.12 shows the total energy input into the BDBA salt upon reaching the average temperature of 452° C. After 2×10^6 seconds, it approaches 4×10^{10} Joules, which is still well shy of the 5.4×10^{10} Joules required to establish meaningful circulation with the liquid BDBA salt. The surprising result is that *the BDBA salt does not melt enough* to cause covering of the FHR vessel.

The base case scenario with a 1047 MW core (on average) and *no* radiation appears to stave off fuel failure and flibe boiling—barely—during the entire accident scenario *without the aid* of the circulating salt (or radiation). The amount of BDBA salt required to melt to cause a liquid circulation pattern between the FHR vessel and the steel liner—thus increasing the heat transfer coefficient for convection *and* conduction by at least an order of magnitude—is not reached. However, radiation is expected to play a large role in this high temperature reactor scenario and the results of this model are discussed in Chapter 11. On the other hand, requiring *less salt* to melt in order to cause meaningful circulation is

another possibility. Reducing the air cavity size would require less salt to melt, but the question remains to what extent it will affect the overall system temperatures.

9.4 Validating the Solution

A first-order analysis can be performed to verify that the solution produced in STAR-CCM+ is reasonable. There are numerous correlations for determining convection heat transfer coefficients and approximating conduction in one-dimensional cases. A look at some of the comparable data that can be quantified is detailed in Appendix A.

Chapter 10

Effect of Reducing the Air Cavity Annular Gap

A modification of the base case geometry with the 6m air cavity radius (and 3m air cavity annular gap) was run with a 4 meter air cavity radius (a 1m annular gap). The goal was to (1) see the temperature dynamics with a reduced air cavity and (2) see if enough energy would be put into the salt to melt it to a a meaningful level for heat transfer in the cavity. If the BDBA system maximum temperatures are acceptable with a reduced air cavity, this would be advantageous to the overall system design. Shrinking the radius of the FHR would requires far less capital cost and material.

10.1 Reduced Annular Gap Model

Similar to the modeling of Chapter 9, the STAR-CCM+ model was initiated with the base geometry and boundary conditions given in Figure 10.1. In the same manner as the previous section, the BDBA salt average temperature was monitored until it reached the FLiNaK liquidus temperature of 452° C. The initial boundary condition placed the 452° C boundary on the outside of the BDBA FLiNaK salt as in Figure 10.1(a). Recall that this was the conservative model that is computationally permissible as discussed in Section 7.1.

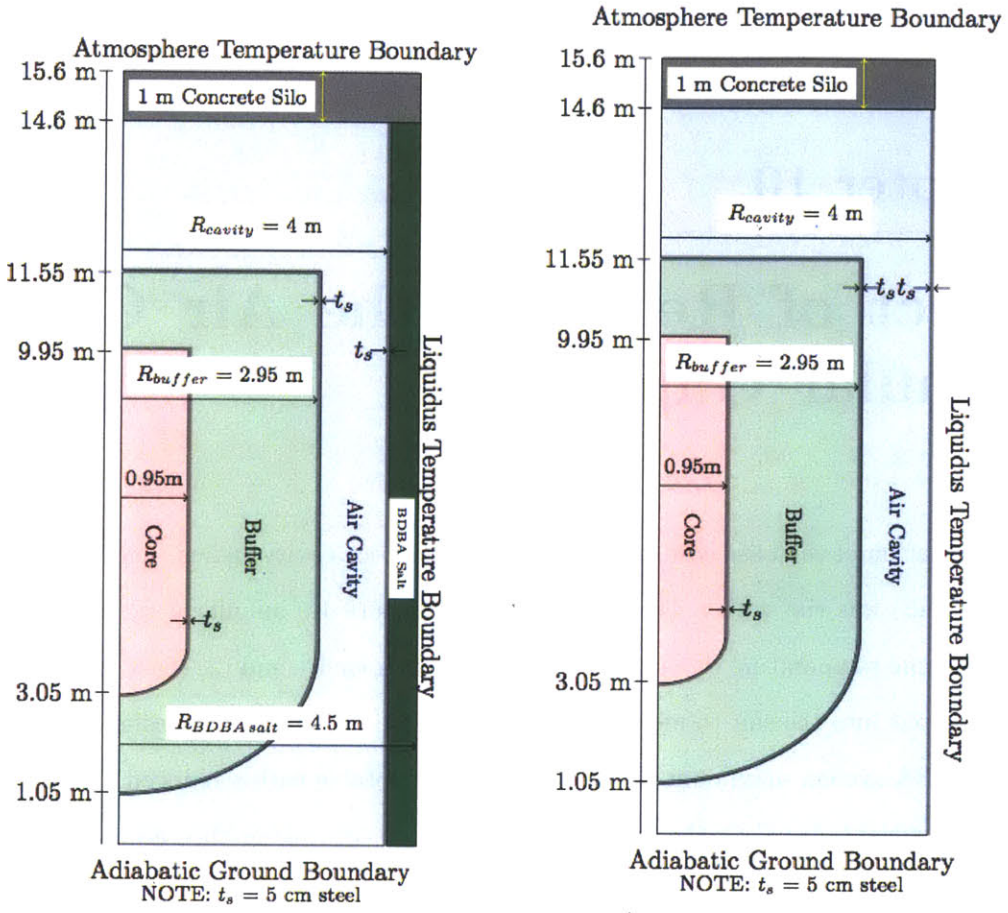

(a) 4m Air Cavity Model until BDBA Salt Average Temperature Reaches 452° C.

(b) 4m Air Cavity Model with BDBA Salt at Liquidus Temperature.

Figure 10.1: 4m Air Cavity Models.

The model was then switched to the constant temperature boundary at the outside of the steel liner as in Figure 10.1(b).

The BDBA salt was monitored as in Chapter 9 and the results are plotted in Figure 10.2. The time required to reach the liquidus temperature (for the volume-weighted average), is $t = 244305$ seconds (about 68 hours). The average component temperatures are given in

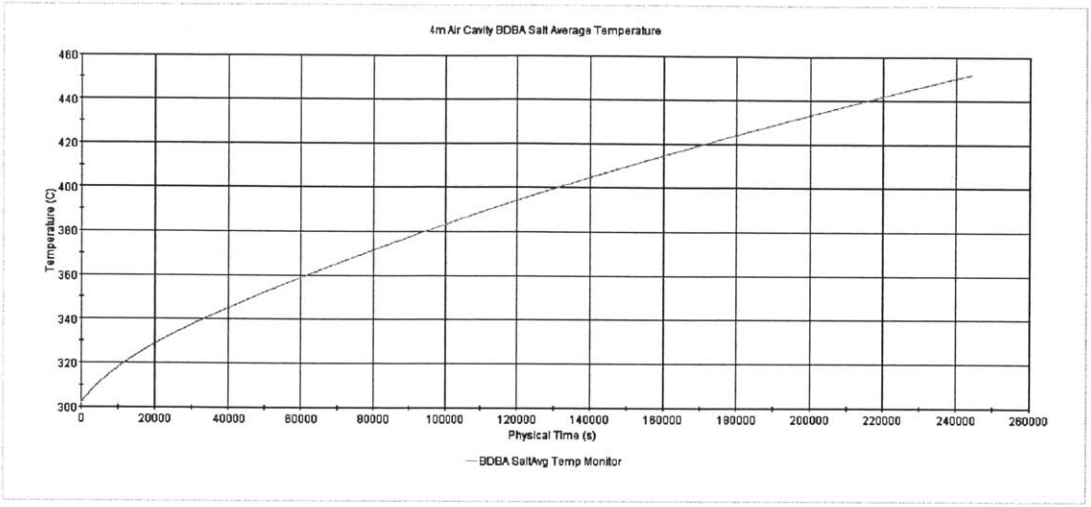

Figure 10.2: 4m Air Cavity BDBA Average Salt Temperature vs Time.

Table 10.1.

$t_{\text{liquidus}} = 244305$ sec (68 hours).
Component Average Temperatures

	°C	K
Core	1103	1376
Core Vessel	1051	1324
Buffer	970	1243
Steel Vessel	963	1236
Air	684	957
Liner	528	801
BDBA Salt	452	725

Table 10.1: Component Temperatures when BDBA Salt Average Temperature is 452° C.

This compares with the base case (6 meter radius air cavity) reaching the liquidus temperature in 281190 seconds—a 13% reduction in time to reach liquidus temperature. A 66.5% reduction in cavity volume only reduces the time to reach 452° C in the BDBA salt by 13%. Furthermore, it is striking to compare the temperatures in this 4 meter cavity case against the 6 meter cavity case.

10.2 System Temperatures

The core, buffer, and vessel temperatures upon reaching the liquidus temperature of the BDBA salt actually *decrease* by reducing the volume of the air. The temperature of the *air* and outer *steel liner* increase slightly (by about 5° C from the base case).

The volume of the core, the power output, the volume of the buffer and vessels are all identical between the 6m and 4m cavity cases. Recall from Chapter 9 that the heat transfer to the air—by convection and conduction—is what limits the overall heat removal scenario. Here, the distance that the heat needs in order to *conduct* through the air has decreased by a factor of three. A 3 meter radial distance to the BDBA liner has become a 1 meter radial distance. One-dimensional thermal resistance to conduction is given by L/k, where L is the length of conduction, and k is the thermal conductivity. Here, thermal conductivity is nearly constant—it is dependent on temperature which is very similar in the air cavity in both cases—but L is significantly decreased. Therefore, heat is transferred faster to the BDBA salt, but is still limited by the very weak conductive abilities of air and weak convective heat transfer coefficients for gases in natural circulation as discussed in Section 10.3.

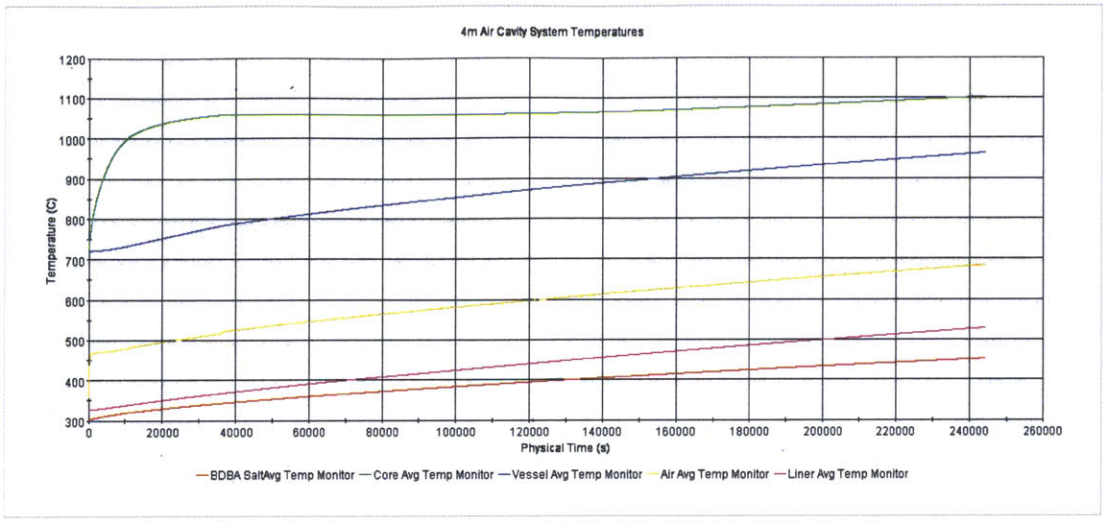

(a) System Temperatures during first $t = 244305$ seconds (68 hours).

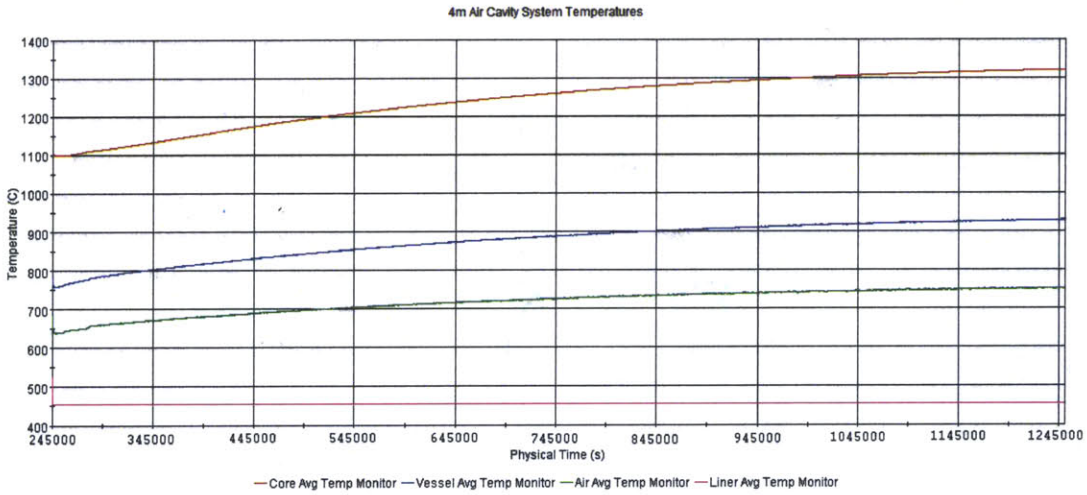

(b) System Temperatures after $t = 244305$ seconds (68 hours).

Figure 10.3: 4m Air Cavity Model Overall System Temperatures vs Time.

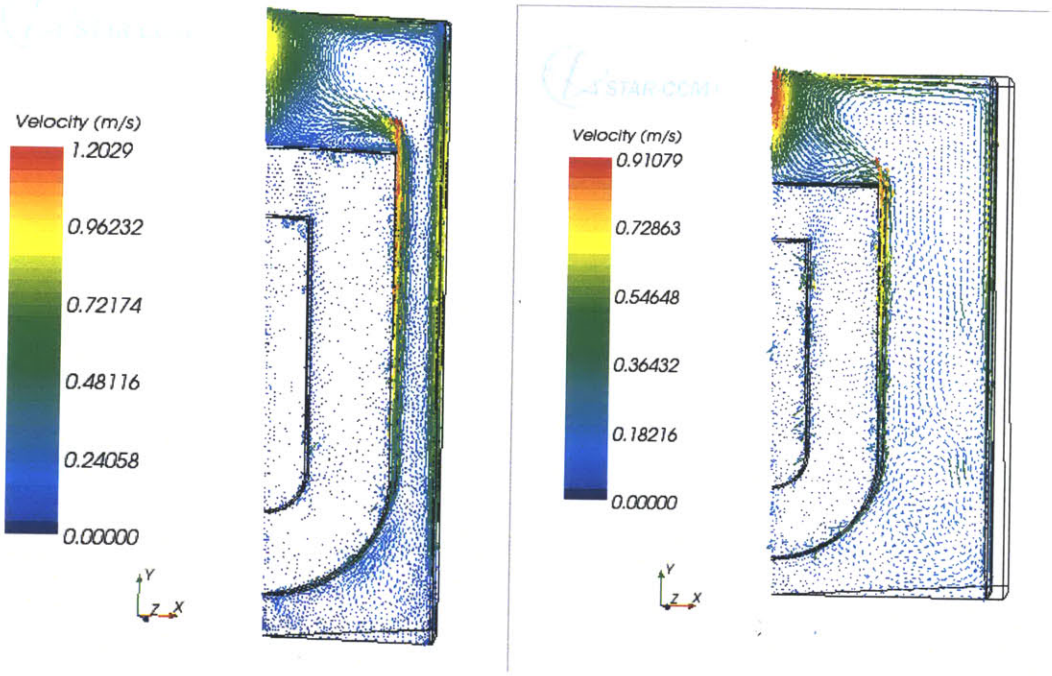

(a) 4m Cavity at $t = 244305$ sec (68 hours).

(b) 6m Cavity at $t = 281190$ sec (68 hours).

Figure 10.4: Convective Currents when BDBA Salt Temperature Reaches Liquidus Temperature.

10.3 Convective Currents

As in the 6m air case, the convective currents at any given point in time in the core and buffer are rather small in magnitude. Rather, the convection occurring in these regions serves to give near isothermal conditions. However, the air has a significant ΔT across its region from the FHR outer vessel to the BDBA liner. The convective currents are given in Figure 10.4(a). Recall from Section 8.1.3 that high-Rayleigh number modeling is inaccurate with available computational methods. Therefore, only general trends can likely be trusted. Comparing Figure 10.4(a) with Figure 10.4(b) from the 4m and 6m case,

Figure 10.5: Convective Heat Transfer Coefficient (W/m^2-K) vs Time.

respectively, the noticeable difference is the velocities in each case. The much narrower space within which the convective currents are forced likely causes a higher velocity.

The heat transfer coefficient in the 4m case provides a little bit more insight into the modeled solution. In the 4m case, one sees a higher coefficient than in the 6m case. (Figure 10.5 vs Figure 9.6). This should be expected if the velocity is higher in the 4m case—a higher velocity in the boundary layer correlates with a higher heat transfer coefficient. However, the heat transfer coefficient in *both* cases is still very—1 to 2 W/m^2-K, indicating that convective heat transfer through the air cavity is going to be inefficient.

10.4 Total Energy Input and Circulating Salt

As in Section 9.3, the total energy input into the BDBA salt *after* it reached the liquidus temperature is monitored as in Figure 10.7. In this case, there is only a 4 meter radius for the air cavity and the same dimensions for the FHR vessel:

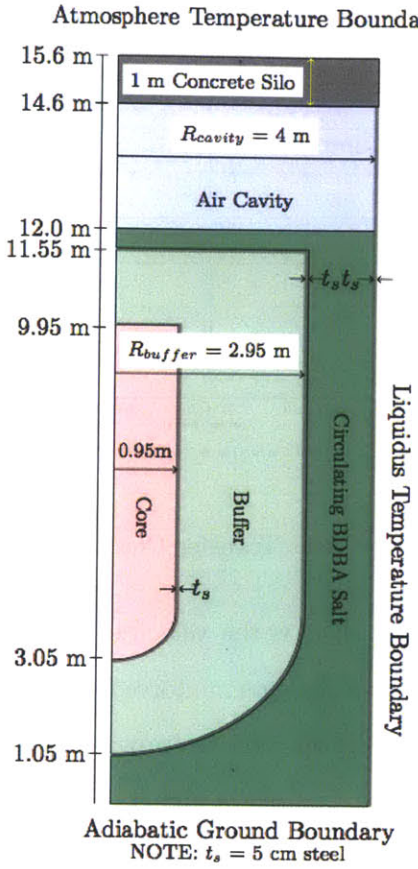

Figure 10.6: Model of 4m Air Cavity with Circulating Salt Immersing Vessel.

$$V_{\text{for circulation}} = \pi\left(r_{\text{air}}^2 h - (0.5)\frac{4}{3}r_{\text{hemisphere}}^3\right) = \pi\left(4^2(4) - \frac{2}{3}(3)^3\right) = 145\,\text{m}^3 \tag{10.1}$$

$$E_{\text{for circulation}} = V\rho E_{\text{fsn}} = 145\,\text{m}^3(2019\,\text{kg/m}^3)1.6\times10^6\,\text{J/kg} = 4.7\times10^{11}\,\text{J} \tag{10.2}$$

$$E_{\text{required to circulate, simulation}} = \frac{15}{360}(1.7\times10^{11}\,\text{J}) = 1.9\times10^{10}\,\text{J} \tag{10.3}$$

Figure 10.7 shows that 1.9×10^{10} Joules is reached at $t = 1.249\times10^6$ seconds (14.5 days).

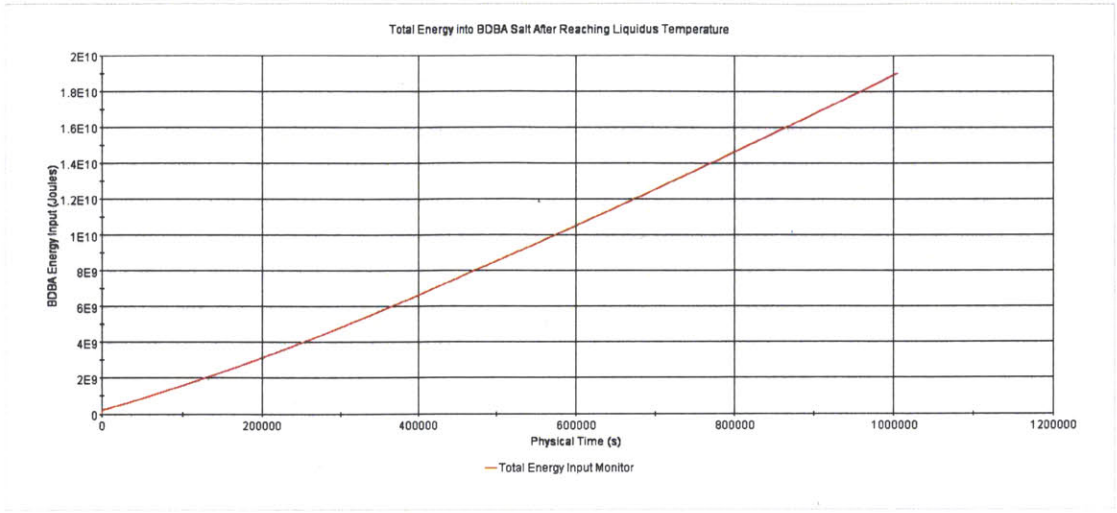

Figure 10.7: Energy of Fusion Input into BDBA Salt.

When this is reached, the hemispherical head of the FHR outer vessel is fully immersed in salt. In reality, salt melted and rose to this level while beginning the heat transfer process from the lower head portion of the FHR vessel. The dynamic modeling of melting salt and varying geometry is very difficult and is saved for future work. Heat transfer by liquid salt convection started some time before this, and convective heat transfer will continue to increase as the level of the melted salt rises. Only one level was analyzed in this case—the modeled system is in Figure 10.6. This is when the FHR vessel is fully submerged in the circulating salt. Table 10.2 shows the component average temperatures when the BDBA salt energy input is 1.9×10^{10} Joules.

The expected temperature behavior trends for the FHR system with circulating salt is illustrated in Figure 10.8. The circulating salt interfaces with the FHR outer vessel. This significantly drives the temperature of the vessel down from over 1000° C by a few hundred degrees, and should continue to decrease until it equilibrates with the circulating salt temperature. Note that the air temperature sees a significant decrease. This is because

$t_{\text{heat of fusion}} = 1.25 \times 10^5$ seconds (14.5 days)

Component Average Temperatures		
	°C	K
Core	1321	1594
Core Vessel	1294	1567
Buffer	1259	1533
Steel Vessel	1253	1526
Air	753	1026
Liner	454	727

Table 10.2: Component Temperatures when BDBA Salt Energy Input Reaches 1.9×10^{10} Joules

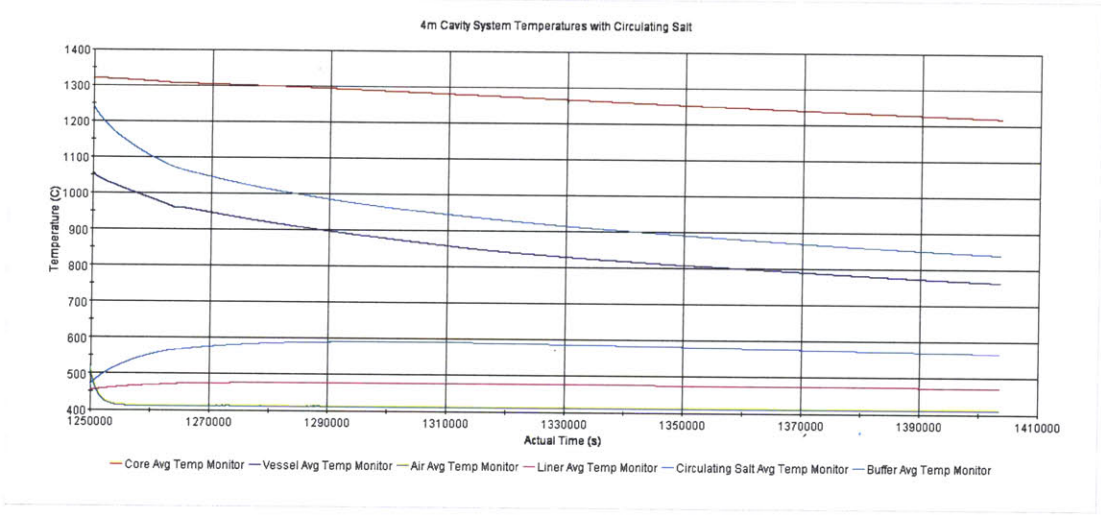

Figure 10.8: System Temperatures after Immersing the FHR Vessel with FLiNaK.

the air is *no longer in contact* with any heated portion of the FHR vessel; rather, it absorbs heat from the circulating salt and transfers it upward to the atmosphere boundary (via the concrete silo) and outward to the steel liner. See Figure 10.9. The buffer follows the steel liner temperature, but is limited by the conduction through the steel vessel. Finally, there is a definite downward trend in the core temperature. However, the core is still seeing heat generation. Even after 1.3×10^6 seconds, there is still 0.2% of full power being generated

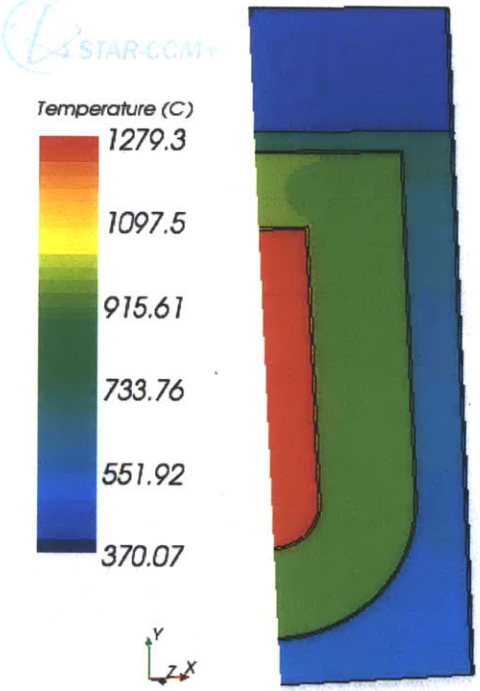

Figure 10.9: Temperature Distribution with Circulating Salt, 1.3×10^6 seconds.

in the core; this is preventing the core temperature from falling precipitously.

The positive result of reducing the cavity radius is the significant increase in heat transfer through the air by (1) decreasing the conduction length during the first part of the sequence and (2) increasing the convective heat transfer coefficient and thermal conductivity of the gap by over a factor of 10 each when the circulating salt is initiated in the cavity. The vessel/circulating salt interface heat transfer coefficient is plotted in Figure 10.10. Compare this with the h values seen in Figure 10.5. However, the reduced air cavity does come at a cost. Note the peak temperature in Figure 9.7. It occurs at approximately 1.5×10^6 seconds without any aid of circulating salt before the temperatures

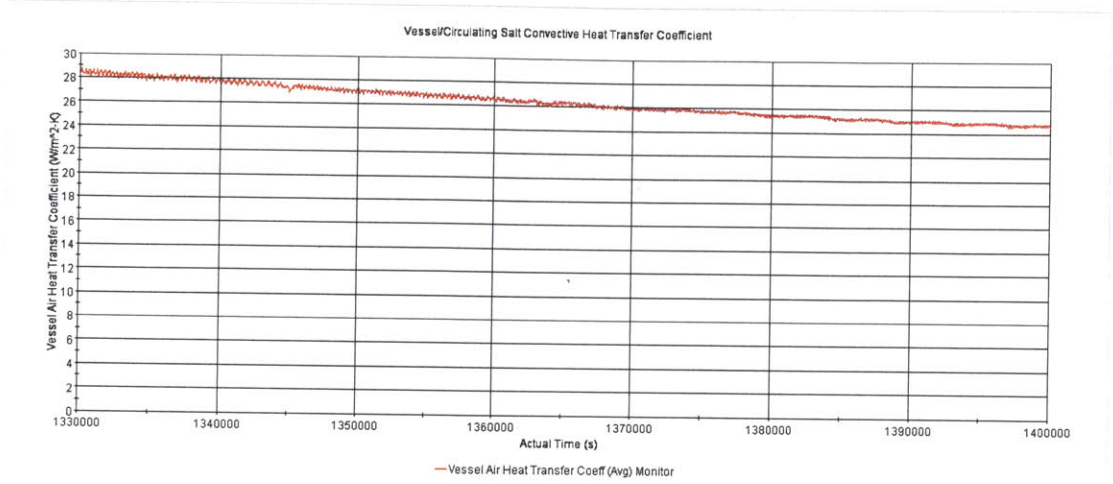

Figure 10.10: Circulating Salt/Vessel Interface Heat Transfer Coefficient.

begin to fall. On the other hand, in the 4m air cavity case, the *heat capacity* of the entire air volume is much less than that of the 6m case due to the 66.5% reduction in cavity volume. Therefore, in Figure 10.3, one sees that there is still an increasing trend in system temperatures before the BDBA salt is melted. However, the BDBA salt melting process starts a much more effective heat transfer process through the cavity; therefore the reduced cavity radius is significantly beneficial for the FHR system with its *lower* peak temperatures (well below the fuel melting and flibe boiling point).

This case was entirely for a non-radiative system. However, a base case radiation model was introduced in a few iterations to approximate the type of effect this has on the FHR system. The net result of this is that radiation heat transfer should be relied upon to have meaningful heat transfer from the steel vessel to the steel liner and greatly reduce the amount of time until the BDBA salt begins to melt and aid in vessel heat removal, and more importantly, limit peak system temperatures. This is discussed in the next chapter.

Chapter 11

Radiation

Recall that all matter at a non-zero absolute temperature continuously emits energy termed *radiation*. This energy is transported by electromagnetic waves. Unlike the conduction and convection heat transfer, radiation does not require any matter. Radiation is emitted by a surface and this energy originates from the *thermal* energy that is contained in the surface.

A few concepts are key to understanding that radiation will be an important phenomenon in the FHR. Emissive power is the energy flux (W/m^2) from a surface. For a perfect emitter (termed a blackbody) there is an upper limit that can be emitted:

$$E_{\text{blackbody}} = \sigma T_s^4 \tag{11.1}$$

where σ is the Stefan-Boltzmann constant and T_s is the surface temperature in absolute units.

There are no perfect emitters, so a real surface has an emissive power equal to $E = \epsilon\sigma T_s^4$ where ϵ is termed the *emissivity* of a surface Emissivities are tabulated for many substances and many different temperatures [15].

In addition to emitting radiation, materials have radiation incident on their surfaces,

which is termed irradiation, G. This irradiation may be *absorbed*, *reflected*, and/or *transmitted*. Simple engineering models often treat liquids as opaque and and gases (like air) as transparent to radiation. Issues arise with these models for very high temperatures and for liquids which are semi-transparent [1].

To further complicate the problem, radiation is highly dependent on the spectral distribution—which varies with the nature of the surface and its geometry—and the directionality; that is, many surfaces emit preferentially in certain directions. For a certain geometry over a certain spectral range for a certain material, one can determine the coefficients of absorptivity, reflectivity, and transmissivity to determine the overall *net* radiative heat flux through a surface.

Radiation analysis is greatly simplified by using Kirchhoff's law. This states that for any surface in an isothermal enclosure, the emissivity equals the absorptivity. It is apparent that radiation heat transfer will not occur in an isothermal body. However, it has been shown that if irradiation is diffuse (that is, the irradiation is independent of direction) and the material surface is diffuse (the emissivity and absorptivity of the surface are independent of direction), Kirchhoff' law is valid for many engineering applications. Furthermore, for a surface in which a material's emissivity and absorptivity are gray, these coefficients are assumed to be independent of the wavelength of radiation [1]. Assumption of a gray surface is reasonable for many engineering applications; however, this assumption diverges when the spectral regions of irradiation and emission are widely separated [1].

Since it is clear that the FHR is a high temperature system, radiation needs to be considered in the overall analysis. The ultimate source surface of radiation–the vessel surrounding the primary coolant–has the potential to operate near 1750 K during a beyond design basis accident. The irradiation surface–the steel liner–could be near 500 K. Therefore, the emissivity will depend on the emission temperature while the irradiation

will depend on the liner surface temperature. The spectral distribution of absorption and emission are likely to vary over these temperature ranges; thus, a gray surface approximation is only a first-order approximation for radiation analysis; experimentation will need to be accomplished to determine the spectrally-dependent radiation effects.

11.1 Thermal Radiation Model

A Thermal Radiation Model is used to define how thermal radiation properties are modeled– as either wavelength independent (gray) or as wavelength dependent (spectral). The choice pertains uniformly to all radiation within the regions of the simulation and in the surrounding environment. The Thermal Radiation model is responsible for managing the radiative properties and spectrum-dependent solution variables in the continuum. The type of Thermal Radiation model may be either Gray (wavelength-independent) or Multiband (spectral).

11.1.1 Gray Thermal Radiation Model

The Gray Thermal radiation model makes it possible to simulate diffuse radiation *independently of wavelength.* With this model, radiation properties of the media and surrounding surfaces are considered the same for all wavelengths. This is the approximation that is used for this first iteration of radiation in the FHR.

However, the medium that fills the space between the surfaces may also absorb, emit, or scatter radiation. Therefore, the amount of radiation that is received and emitted by each surface depends on this effect, as well as the optical properties of the surface and the thermal boundary conditions that are imposed on it. In a simulation, the Participating Media Radiation model lets one control these phenomena by activating material properties with related parameters. Because of the lack of data on geometry and salt properties with

respect to radiation, the media in this analysis is considered non-participating. More is discussed in Section 14.1.

Emissivity Emissivity is the ratio of the power that is emitted by a body to the power it would emit as a black body at the same temperature (dimensionless). This is tabulated for many material types and temperatures [1, 15]. This model used the values for 700° C from Reference [1] of 0.3 for steel and 0.9 for the concrete boundary surfaces (like the silo atmospheric boundary and the ground boundary).

Reflectivity Reflectivity is the ratio of reflected radiant energy over incident radiant energy at a given surface (dimensionless). It is calculated from the specified emissivity and transmissivity using Kirchhoff's law (Reflectivity = 1 - Emissivity - Transmissivity).

Transmissivity Transmissivity is the ratio of transmitted radiant energy to incident radiant energy at a given surface (dimensionless). As previously mentioned, the simple approach of treating solids (steel) as opaque was used. Thus, the transmissivity was set to zero for the concrete silo boundaries and the steel liner and vessel surfaces. Transmissivity in between the core vessel (steel surface) and the buffer vessel (steel surface) will not, in actuality, be zero. Since this is a liquid buffer, the media (buffer solution) should be modeled as a semi-transparent surface. Further iterations of radiation modeling will need to analyze the transmissivity of the salt.

11.2 Surface-to-Surface (S2S) Radiation Model

The S2S Radiation model makes it possible to simulate thermal radiation exchange between diffuse surfaces forming a closed set. The medium that fills the space between the surfaces is non-participating (i.e. air). That is, it does not absorb, emit, or scatter ra-

diation. Under these circumstances, the radiation properties and the thermal boundary conditions that are imposed on each surface uniquely define the amount of radiation that a surface receives and emits. The surface properties are quantified in terms of emissivity, reflectivity, transmissivity, and radiation temperature. These properties are not dependent on direction.

11.2.1 Radiation Modeling with View Factors

To compute radiation exchange between any two surfaces, one must first introduce the concept of a *view factor* (also called a configuration or shape factor).

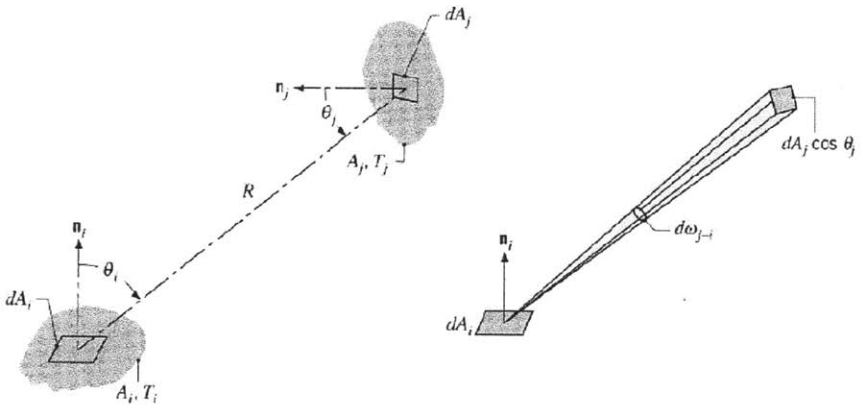

Figure 11.1: The View Factor Integral [1].

The View Factor Integral The view factor F_{ij} is defined as the *fraction of the radiation leaving surface i that is intercepted by surface j.* To develop a general expression for F_{ij} consider the arbitrarily oriented surfaces A_i and A_j. Elemental areas on each surface, dA_i and dA_j are connected by a line of length R, which forms the polar angles θ_i and θ_j, respectively, with the surface normals $\mathbf{n}_i$ and $\mathbf{n}_j$. The vales of R, θ_i, and θ_j vary with the position of the elemental areas on A_i and A_j.

Recalling that $d\omega$ is a differential solid angle (steridians), the spectral intensity I (with units W/m^2-si-μm) is then

$$I_{\lambda,e}(\lambda,\theta,\psi) \equiv \frac{dq}{dA_1 \cos(\theta)\, d\omega\, d\lambda}$$

From this definition of radiation intensity, the rate at which radiation *leaves* dA_i and is *intercepted* by dA_j is based on the surface i emitting and reflecting diffusely:

$$dq_{i\to j} = I_{e+r,i} \cos(\theta_i)\, dA_i\, d\omega_{j-i}$$

What results is that

$$F_{ij} = \frac{1}{A_j} \int_{A_i} \int_{A_j} \frac{\cos(\theta_i)\cos(\theta_j)}{\pi R^2}\, dA_i\, dA_j \tag{11.2}$$

This equation may be used to determine the view factor associated with any two surfaces that are *diffuse emitters* and *reflectors* and have *uniform radiosity.*

View Factor Relations An important view factor relation is that

$$A_i F_{ij} = A_j F_{ji}$$

This expression, termed the *reciprocity relation,* is useful in determining one view factor from knowledge of the other.

Another important view factor relations pertains to the surfaces of an *enclosure* (upon which one can model the FHR air cavity). From the definition of the view factor, the *summation rule*

$$\sum_{j=1}^{N} F_{ij} = 1 \tag{11.3}$$

may be applied to each of the N surfaces in the enclosure. This rule follows from the conservation requirement that all radiation leaving surface i must be intercepted by the enclosure surfaces. The term F_{ij} appearing in this summation represents the fraction of the radiation that leaves surface i and is directly intercepted by j.

To calculate radiation exchange in an enclosure on N surfaces, a total of N^2 view factors is needed. This requirement becomes evident when the view factors are arranged in the matrix form:

$$\begin{bmatrix} F_{11} & F_{12} & \cdots & F_{1N} \\ F_{21} & F_{22} & \cdots & F_{2N} \\ \vdots & \vdots & \ddots & \vdots \\ F_{N1} & F_{N2} & \cdots & F_{NN} \end{bmatrix} \tag{11.4}$$

The view factor may be determined by solving the double integral of Equation 11.2. STAR-CCM+ analyzes this view factor prior to running a radiation model and uses these view factors throughout the simulation.

11.2.2 Modeling with the View Factors Model

Within STAR-CCM+, the S2S Radiation model is operated in two steps:

- Calculate the view factors using ray tracing.
- Apply view factors to compute radiosity and irradiation fields on all surfaces.

In the view factor calculation step, deterministic ray tracing is applied to compute the factors. Rays are traced into the hemisphere above each patch using a fixed distribution of

directions over this hemisphere. By default, a distribution of 1024 rays per patch is used.

The view factors must be calculated only when the geometry and radiative properties such as transmissivity and specular reflectivity change. Therefore, they generally can be calculated once and then reused during the combined-mode heat transfer solution to update the radiative fluxes from the surface emissive powers (that is temperatures).

An advantage of the two-step approach is computational efficiency gains from doing relative infrequent ray tracing. The trade-off is that view factors must be stored, often requiring considerable amounts of memory.

11.3 FHR Base Case with Radiation

The radiation model is the same geometry of Figures 9.1(a) and 9.1(b) described in Chapter 9. The same boundary conditions were used. However, radiation modeling was introduced using a surface-to-surface model with the view factors calculator.

Radiation was set up between the FHR outer vessel and the salt liner. The air is considered non-participating since this was modeled with the Surface to Surface Radiation model. This is likely a good approximation for air as described in Reference [1], but radiation through the FLiNaK liquid will need to be substantially evaluated. For this reason, it was ignored in this simulation. Because the temperatures of the flibe salt in the core, the core vessel, the buffer salt, and the outer vessel are nearly isothermal at the start of the accident sequence, the radiation heat transfer between the core and outer vessel was not modeled. This is also due to the unknown properties of the transmissivity, reflectivity, and absorptivity of the FLiNaK buffer between the core vessel and the outer vessel: this will depend highly on material, salt purity (which could change drastically during a major accident), and wavelength. Therefore, the radiation exchange was only modeled between outer vessel to steel liner; in actuality, any radiation exchange between

the core and outer elements will serve to increase heat transfer from the core; this estimate should be conservative.

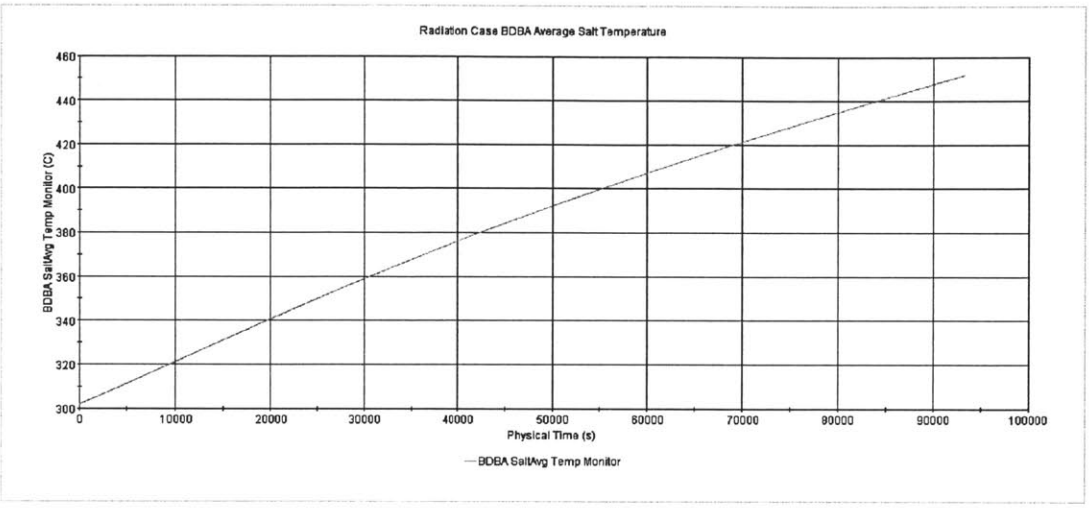

Figure 11.2: Average BDBA Salt Temperature Until Reaching Its Liquidus Temperature (452° C).

$t_{\text{liquidus}} = 93375$ sec (26 hours).

Component Average Temperatures

	°C	K
Core	932	1205
Core Vessel	870	1143
Buffer	789	1062
Steel Vessel	779	1052
Air	727	1001
Liner	703	976
BDBA Salt	452	725

Table 11.1: Component Temperatures when BDBA Salt Average Temperature is 452° C.

As in the previous cases, the simulation was run from the initial temperatures of Section 7.4 until the average BDBA salt temperature reaches its liquidus of 452° C. This is shown in Figure 11.2. The component average temperatures upon reaching the liquidus

temperature are given in Table 11.1. These temperatures were input as initial conditions for the model as shown in Figure 9.1(b). The time at which the average BDBA temperature reaches 452° C occurs in the radiation case at 93375 seconds (26 hours)—67% less time than in the base case. Clearly, the heat transfer effect of radiation is significant in the FHR.

Radiation from the steel vessel to the liner is significant. See Figure 11.3. The temperature difference between the vessel and the steel liner closes to less than 100° C—despite the 3 meter distance. This is a previously unseen result. Recall that in the base case this temperature difference was over 500° C (Figure 9.7). In the base case and the 4m case without radiation, there is a very large ΔT between the vessel and the air. In this case, the radiation exchange between the metal surfaces causes the air to rise in temperature with the liner, which increases much faster in temperature.

Radiation exchange from the FHR outer vessel to the steel liner keeps the buffer salt at a lower temperature, and ultimately the core at a much lower temperature. Whereas peak core temperatures of 1400° C and 1300° C were observed in the two earlier cases, this radiation model shows that a peak core temperature of less than 1000° C might be realized. This would be revolutionary for the FHR.

Another view of the temperature profile is shown in Figure 11.4. This shows a snapshot in time—at 93375 seconds when the BDBA salt average temperature reaches 452° C. The striking result in this illustration is that the maximum temperature in the core is only 240° C higher than the lowest temperature in the steel liner.. Recall that a 240° C difference between the core and buffer alone could be expected in the 6m cavity base case. Compare this illustration with that of Figure 9.3 in the no radiation case. The much smaller temperature differences are significant in the model with radiation.

Another striking difference seen when introducing radiation modeling is the difference

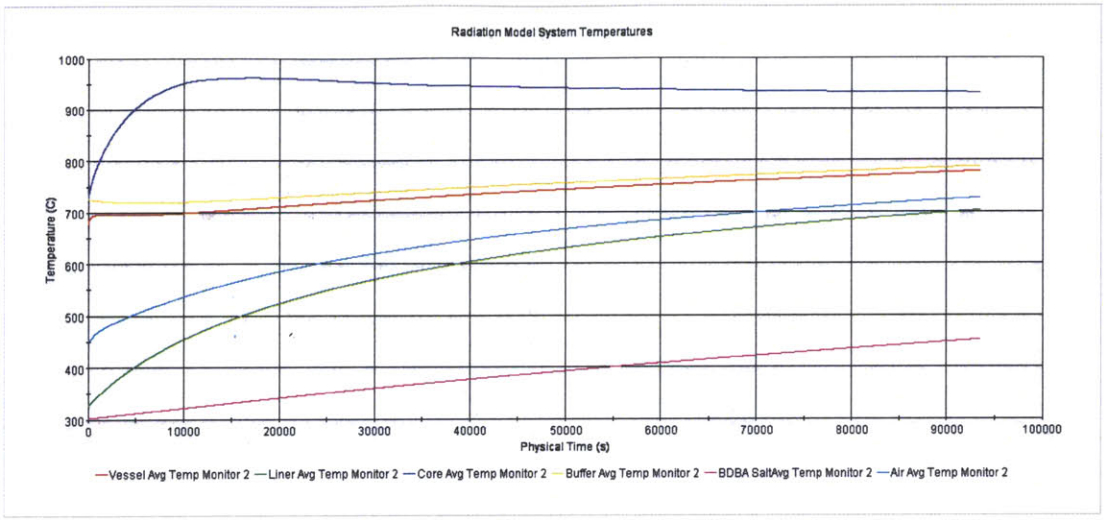

(a) System Temperatures during first $t = 93375$ sec (26 hrs).

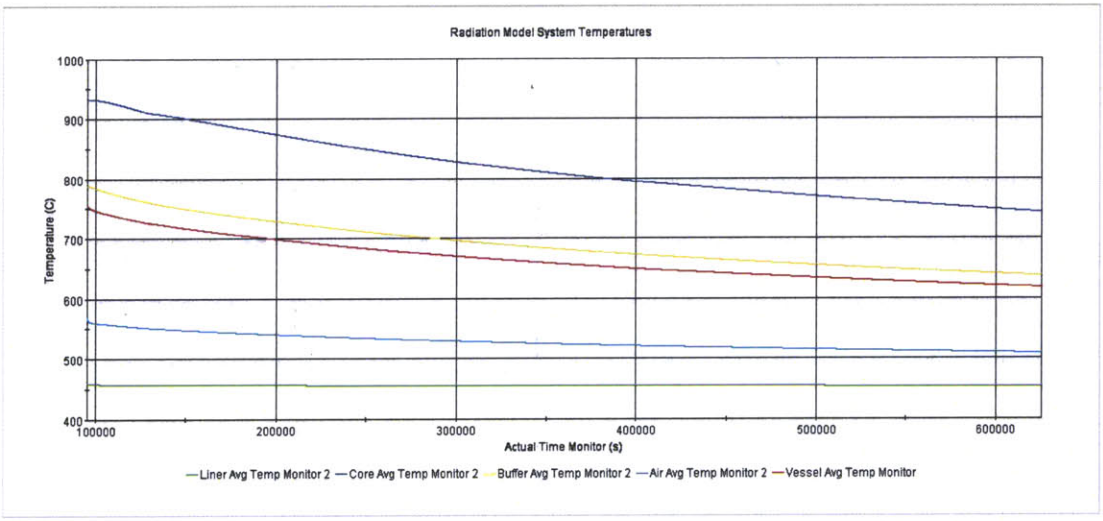

(b) System Temperatures after $t = 93375$ sec (26 hrs).

Figure 11.3: 6m Air Cavity Model Overall System Temperatures vs Time with Radiation Effects.

in the BDBA salt temperature distribution. See Figure 11.5. This figure displays, adjacent to one another, the temperature profile of the BDBA salt in the initial (base) case without radiation and by adding the simplified radiation model. The difference is significant.

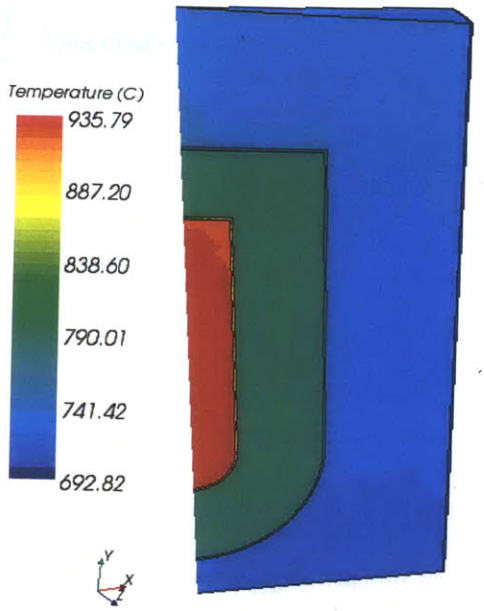

Figure 11.4: BDBA System Temperatures at $t = 93375$ seconds (26 hours).

Figure 11.5(a) is the salt temperature distribution after the BDBA salt *average* temperature reaches its liquidus temperature (452°C) in the base case. Figure 11.5(b) is the salt column with radiation after the BDBA salt average temperature reaches the liquidus temperature. In the no radiation case, the BDBA salt temperature is affected greatly by the air currents. Recall from Figure 9.5(a) that the air will be driven upward from the FHR vessel to the top (atmospheric) cold boundary and back down along the silo wall. Therefore, heat that the air transports is convected to the top of the air cavity and the BDBA salt.

The radiation model, on the other hand, sees a different salt temperature distribution. Recall from Section 11.2.1 that the more "head-on" two surfaces in an enclosure are, the larger the fraction of radiation heat exchange. In this case, the steel vessel has a mostly

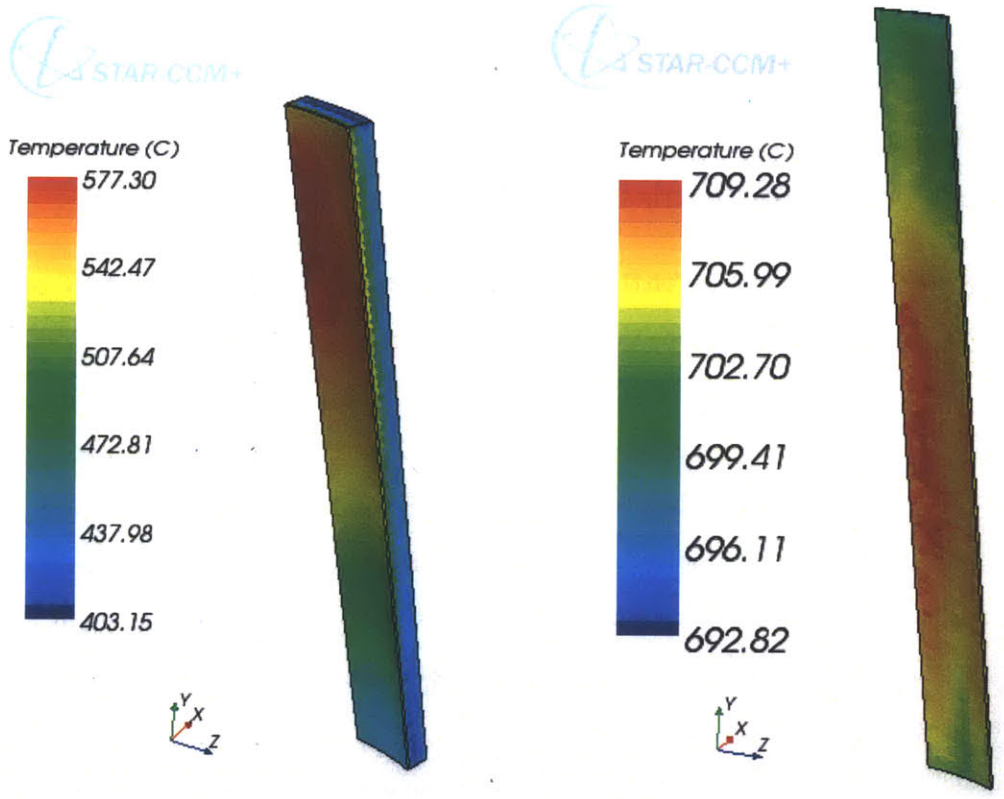

(a) Temperature Profile Without Radiation (b) Temperature Profile with Radiation Model

Figure 11.5: BDBA Salt Temperature Profile When BDBA Salt Average Temperature is 452° C.

vertical cylindrical geometry with a radius of 3 meters. The steel liner is an annulus with an inner radius of 6m. For much of the geometry, these two components act as parallel vertical plates. Therefore, radiation heat exchange leaves the FHR vessel and transports much of its energy directly across to the steel liner. The hottest temperatures in the BDBA salt are in the center from just off the ground up to the location across from the top of the FHR vessel. However, since the surface to surface gray radiation model with view factors

treats surfaces as diffuse emitters, one sees that the overall temperature distribution in the BDBA salt is quite tight–the difference between the maximum and minimum temperatures is only 17° C.

11.4 Optimizing Emissivity

The steel surfaces' emisivities for the buffer vessel and the steel liner were set to 0.3 from the tabulated data of Reference [1]. This is a low value for a "typical, polished stainless steel." However, work on other high temperature projects with metals and molten salts, such as concentrated solar power on demand, have approximated emissivities that are much higher [27]. Reference [22] indicates that Stainless Steel 316 at high temperatures, with a polished finish, has an emissivity closer to 0.7. With an oxidized finish, emissivities are further increased. Use of other stainless steel alloys shows high temperature emissivities upwards of 0.9 [22]. Emissivity research for the work documented in Reference [27] supports the values given in Reference [22].

In light of the higher possible emissivity values, an optimistic radiation case was run to see the effect of carefully selecting metals with high emissivities. As in the first radiation case, the geometry and model of Figures 9.1(a) and 9.1(b) described in Chapter 9 was used with the same boundary conditions. Radiation was again modeled as a wavelength-independent (gray model) system from the FHR outer vessel to the steel liner only as described in Section 11.3. The only difference was the emissivity values of the steel FHR vessel and the steel liner were set to 0.8. This value was chosen because, as described in the previous paragraph, high temperature polished stainless has a value of at least 0.7, and with careful metal selection and alloying treatment, it may be possible to reach 0.9. The emissivity of 0.8 was selected for the simulation, as it lies between these values.

As in the previous cases, the simulation was run from the initial temperatures of Sec-

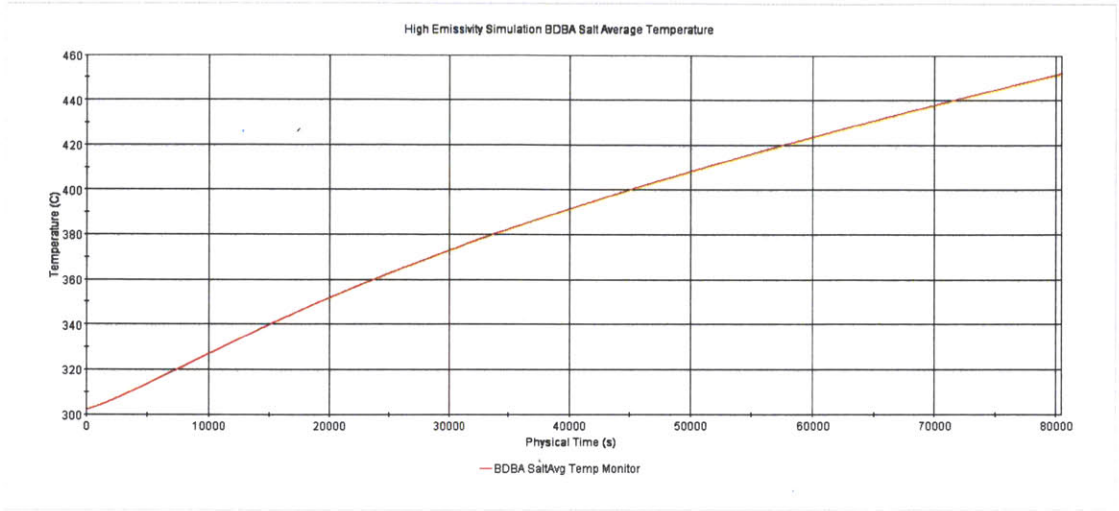

Figure 11.6: Average BDBA Salt Temperature Until Reaching Its Liquidus Temperature (452° C); $\epsilon_{\text{steel}} = 0.8$.

$t_{\text{liquidus}} = 80415$ sec (22 hrs)
Component Average Temperatures

	°C	K
Core	918	1191
Core Vessel	851	1124
Buffer	763	1036
Steel Vessel	754	1027
Air	732	1005
Liner	722	995
BDBA Salt	452	725

Table 11.2: Component Temperatures when BDBA Salt Average Temperature is 452° C; $\epsilon_{\text{steel}} = 0.8$.

tion 7.4 until the average BDBA salt temperature reaches its liquidus of 452° C. This is shown in Figure 11.6. The component average temperatures upon reaching the liquidus temperature are given in Table 11.2. These temperatures were input as initial conditions for the model as shown in Figure 9.1(b). The time at which the average BDBA temperature reaches 452° C occurs in the radiation case with the emissivity of 0.8 instead of 0.3 at

80415 seconds (22 hours)—a 15% reduction in time over the $\epsilon = 0.3$ case.

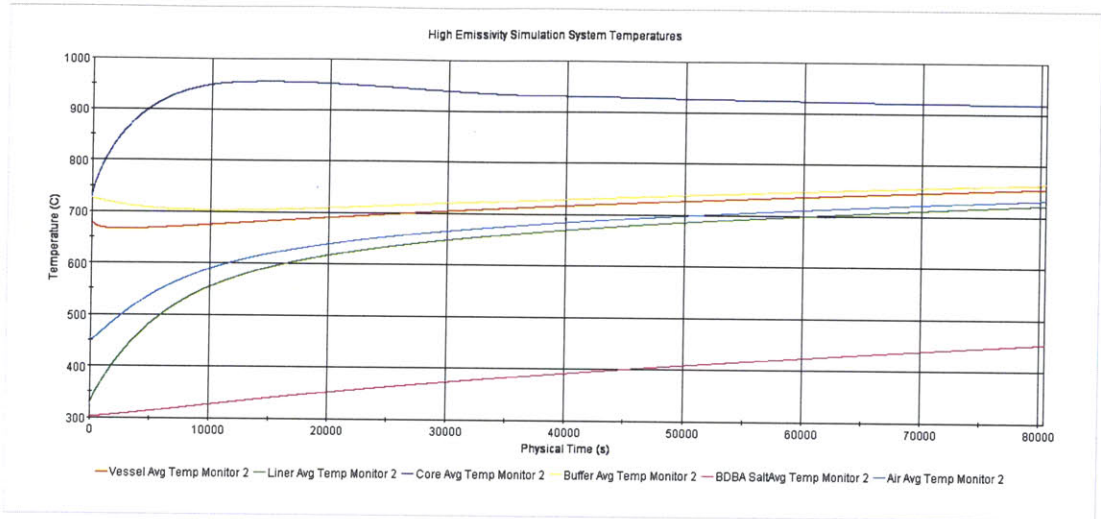

(a) System Temperatures during first $t = 80415$ sec (22 hrs).

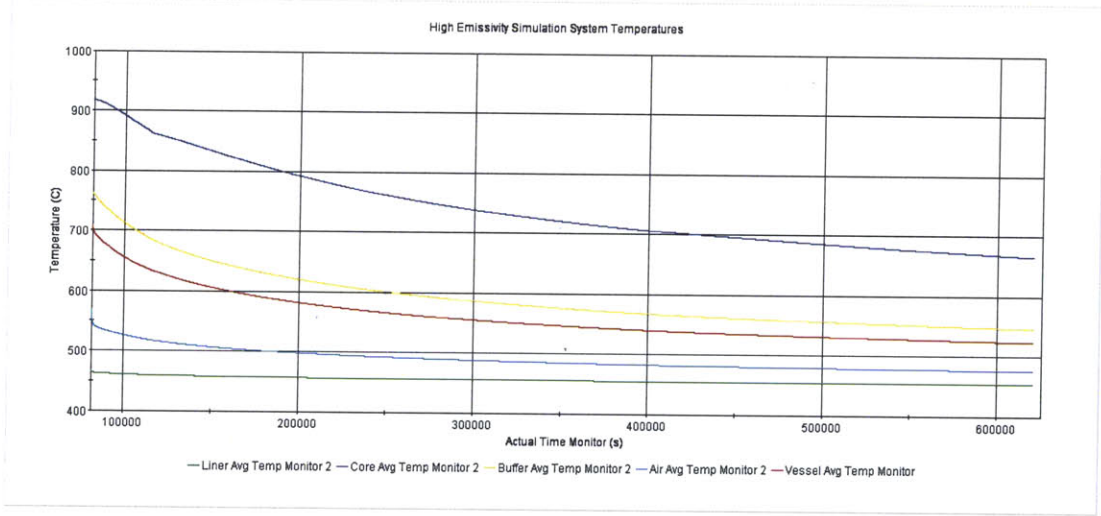

(b) System Temperatures after $t = 80415$ sec (22 hrs).

Figure 11.7: 6m Air Cavity Model Overall System Temperatures vs Time with Radiation Effects for High $\epsilon = 0.8$ Steels.

Figure 11.7 shows the system component temperatures vs time in the high emissivity case. A key feature to note is that, by comparing with Figure 11.3(a), the core peak

temperature is *nearly the same* in both cases. As discussed earlier in the report, the core heats up the primary coolant during the initial stages of the accident to establish the ΔT. Significant heat transfer of any kind—radiation included—does not occur until core heatup. Therefore, both radiation cases show a peak core temperature early in the accident (about 3 hours) of approximately 950° C.

What is noticeable between the emissivity cases is the steel liner temperature. In the low emissivity case of Figure 11.3(a), the steel liner barely reaches 700° C, peaking at 703° C. In Figure 11.7(a) with the emissivity of 0.8, the same liner reaches 722° C in 13% less time (22 vs 26 hours). While this sounds minor, as it is only a 2.3% increase in absolute temperature, this will affect the overall accident sequence stabilization. See Figure 11.8. This is the total energy input into the BDBA salt upon reaching the average salt temperature of 452° C. In both emissivity cases, the model was run for 540000 seconds (150 hours) after reaching the BDBA salt liquidus temperature. In the case of the higher emissivity, the total energy input is 3.7×10^{10} J; in the lower emissivity case, the result is 3.4×10^{10} J. This is a 10% increase in energy input over nearly the same timeframe. After reaching sufficient energy into the salt, temperatures of the liner, air, and FHR outer vessel are expected to drop rapidly as illustrated in Figure 10.8.

Clearly, radiation heat transfer is a dominant effect in the FHR BDBA accident scenario. Higher emissivity values will result in reaching the BDBA liquidus temperature faster as well as melting the BDBA salt to produce the flooded silo faster; however, the core peak temperature is barely affected by markedly increased emissivities. This is because of the accelerated primary coolant heatup in the first hours of the accident to produce a ΔT between the core and surrounding environment. Note that in both cases, the peak temperatures of the core—about 950° C—are reached long before the BDBA salt reaches the liquidus temperature. Reaching liquidus temperature and melting the BDBA salt en-

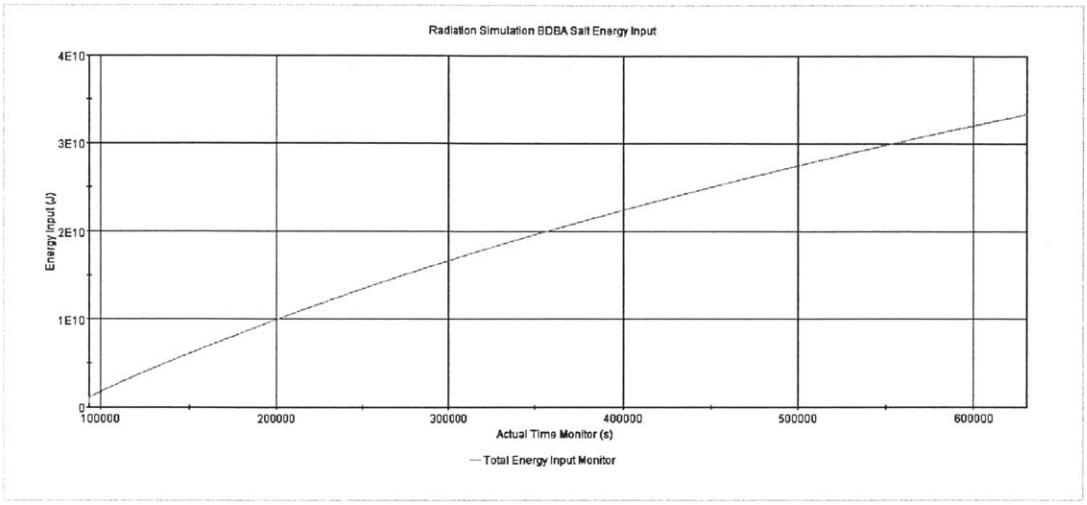

(a) BDBA Salt Energy of Fusion Input ($\epsilon = 0.3$)

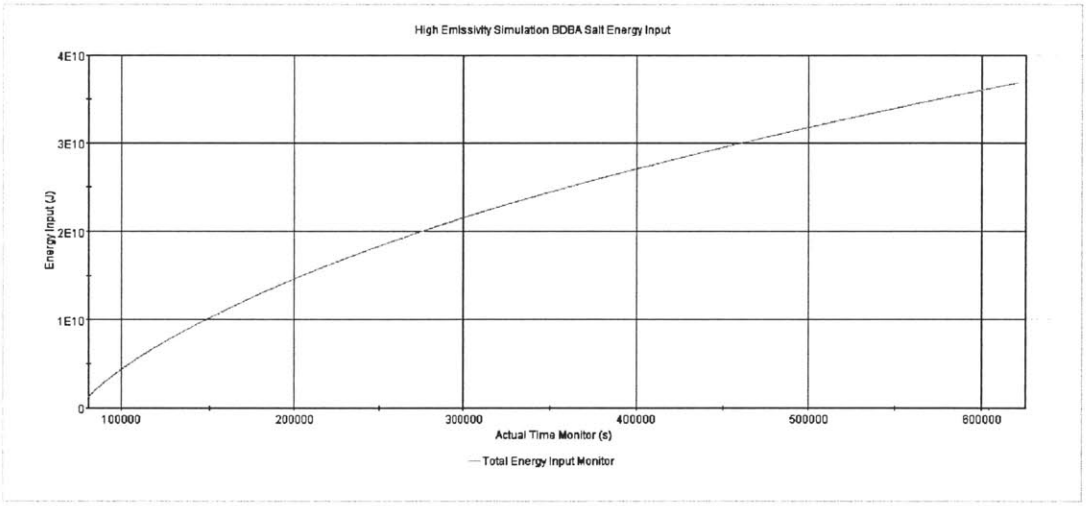

(b) BDBA Salt Energy of Fusion Input ($\epsilon = 0.8$)

Figure 11.8: BDBA Salt Energy of Fusion Input (J) After Reaching 452° C. Time in each case is 150 hours after reaching 452° C.

sures that the FHR system will be placed in a very stable condition transferring more decay heat out of the core than is being put in by decay heat for a long time without operator action. Radiation heat transfer shows that higher core powers than the modeled

1047 MW_{th} can be achieved and keep the fuel from melting which would require a primary coolant temperature of nearly 1450° C.

11.5 Limitations of Modeling with Radiation

Radiation modeling is tough to capture and depends on numerous phenomena that are wavelength, geometry, and temperature-dependent. See further discussion in Sections 12.6 and 14.1.

Chapter 12

Sources of Error and Uncertainty

12.1 Vessel Design

As demonstrated in Chapter 10, reducing the outer radius of the air cavity changes the dynamics of the peak temperatures, heat flux and temperature distributions, and ability of the BDBA salt to heat and melt. It changes the time scale of the accident significantly. The base geometry for the FHR was described in the earlier sections of this report. However, as material selections are made, especially for the high temperature vessel parts, geometries of the different segments will change.

Surface to Volume ratios of the geometries will drastically change the heat distribution. This core was modeled as a 1 meter radius cylinder with a hemispherical head and 6 meters height. However, as the height is reduced the volume to the surface area ratio actually increases. This has a negative effect on the ability of the core to dissipate heat as the volumetric heat source within the core (the fuel) does not have as much surface area and convective surface interface to dissipate the heat with the surrounding buffer. However, while this is negative for the dissipation of decay heat in an accident, a lower surface area

to volume ratio (and higher volume to surface ratio) is much better for neutron economy—therefore plant economics. This will be a balance that will continue to evolve.

Material selection will play a large part in the heat transfer as well. Stainless steels have thermal conductivity on the order of 15 W/m-K [1]. Some alloys of steel have a thermal conductivity three times this, and some pure metals have a thermal conductivity of hundreds of W/m-K. Salt selection will affect the density, system mass, volumetric heat capacity and heat transfer coefficients. The selection of gas—assumed to be air (in the air cavity) for this report, will have an effect on heat transfer. Some gases are great insulators while some will be better conductors. A cost/benefit analysis of the vessel materials, salts, and gases will have to be performed taking into account the wide variety of factors—from cost to neutron economy to thermal properties and chemical concerns.

12.2 Core Design

The core was modeled as a solution of circulating flibe in this simulation. The core itself will contain a fuel matrix as well, which was not modeled. Initial assessments assume coated-particle fuel with a graphite-matrix. However, future designs are looking ahead to newer materials like Silicon carbide cladding. Moreover, the choice of primary coolants is not set. Flibe is a starting point based on its extensive use in previous reactor experiments. However, other primary coolants such as NaF-ZrF_4 are possibilities, which have different characteristics. Many of the initial possibilities and feasibility of exploration and design of the core characteristics are beginning in earnest as discussed in Reference [25].

12.3 Volumetric heat source/heat fluxes imposed

The amount of decay heat input is another variable. Coupled with the numerous geometry and core design uncertainties, this adds to the complexity of determining peak temperatures and the accident sequence. Initial designs call for power outputs between 200 and 500 MW_{th} [7, Apdx I.]. However, in the long-term much higher power levels are likely. This model used a base volumetric heat source (5×10^7 W/m^3). This equates to a 1047 MW thermal output for the entire (360°) core. Clearly, raising or lowering the magnitude of the power density (and thus decay heat energy input) will have a significant effect on any accident scenario.

12.4 Turbulence modeling

12.4.1 High Rayleigh Number Convective Turbulence

Free convective flow modeling remains a challenge even with today's computational models. Recent experimental studies of free convection between vertical differentially heated plates shows that there are still many phenomena that are not well understood or captured by any widely-available models. For "basic" cases of differentially heated elements in a symmetric box, 3-dimensional simulations with Rayleigh numbers greater than 10^9 are only able to be modeled using Direct Numerical Simulations (DNS) and Large Eddy Simulations (LES). These types of simulations are phenomenally computationally intensive, and are only able to be performed for very small geometries over limited time periods.

Models that are commercially available, such as STAR-CCM+, make extensive use of Reynolds-Averaged Navier-Stokes (RANS) models. This is a statistical approach to solving the turbulence problem. Unfortunately, RANS predictions deviate significantly from the

experimental and analytic data from direct numerical simulation [4]. This is especially true in symmetric geometries like a cube. However, the geometry of the FHR will work to the modeler's advantage in part of the FHR. In the free convection of the air along the FHR buffer vessel, the model is likely to capture the dominant effects of the airflow because the heated air must flow up and it is constrained by the FHR vessel. As discussed in the earlier results section, the model will have trouble predicting free convective flow where the geometry does not force the movement, such as in the cavity directly above the buffer vessel.

12.5 Salt Melting

The melting salt will remain a large challenge to the FHR event sequence. The spatial and time distribution of the heat flux will likely affect the way the salt melts. The no-radiation (convection only) case showed the the convective current will transport the heat to the top of the cavity and preferentially distribute heat to the top of the BDBA salt column. Depending on how much heat reaches the remainder (lower parts) of the BDBA salt column and the time distribution of the spatial flux, the melting salt might "pool" on the top of the BDBA salt column and prevent the rest of lower portion from actually melting.

On the other hand, a significantly different flux distribution as seen in the radiation case would have a different effect. Here, the hottest temperatures in the BDBA salt are near the center of the vertical BDBA column since the view factors between the hot steel buffer vessel and "cold" steel liner are nearly parallel–allowing for maximum radiation heat transfer. If this were the case seen, then the melting would start here, and the heat would rise to the colder top boundaries, causing much more efficient melting of the BDBA salt column than would likely be seen in the convection only case.

Capturing the time-varying geometrical distribution of heat flux into the salt is a nec-

essary first step in order to provide an accurate two-phase salt melting model. Once this heat flux is captured accurately, then the salt melting model will be valid. The two-phase "volume of fluid" method tracking of the liquid-solid interfaces is computationally intensive. Running an overall model with a two-phase salt melt will take a couple orders of magnitude longer for each case or iteration than will a single-phase model since the number of inner time steps and the physical time step must each be significantly more limiting than the single-phase case.

12.6 Radiation

Radiation is clearly going to assist in dissipating heat from the core to the steel liner. The issue is capturing the emissivity, absorptivity, transmissivity, and reflectivity of each of the metal materials as well as the buffer salt between two of the vessels. This is going to be highly dependent on the actual metal alloys used, the geometry (which will determine view factors), and the properties of the salt. Use of a *participating media* model will be required for the liquid salt, as radiation will not transparently flow through the salt as it will nearly do for (perfectly dry) air.

Spectral dependences on emissivity as well as the radiation coefficients (absorptivity, transmissivity, and reflectivity) introduces significant error in using the gray surface approach to radiation modeling. More discussion on what needs to be accomplished for radiation modeling is discussed in Chapter 14.

Chapter 13

Conclusions

The goal of this report is to study the feasibility of avoiding any large-scale radionuclide release by preventing fuel failure during a loss of all cooling systems in a beyond design basis accident. A key component to the FHR that makes this a possibility is the reactor's operation at *atmospheric pressure* with a large temperature difference from core to the surrounding environment. Because of its atmospheric pressure operation and use of liquid salts with nearly 1000° C between their melting and boiling points, this research shows that *it is possible to avoid fuel failure* by keeping the peak temperatures less than fuel failure and salt boiling point temperatures during a worse-case loss of all cooling systems.

13.1 Liquid Heat Sink

The use of liquid salt as a primary coolant and as a buffer allows for significant absorption of heat. The high volumetric heat capacities of liquid salt (J/m^3-K) allows a substantial amount of energy to be deposited from the fuel into the primary coolant and from the primary coolant into the liquid buffer with a modest rise in the actual core temperature. This *thermal inertia* buys the operator time where temperatures in the core rise at a

relatively slow rate during which the decay heat production is decaying exponentially–this is a very pronounced decay in the first hours following accident initiation.

13.2 Vessel Wall Temperature

The use of a thin-walled reactor vessel allows the outer surface of the vessel to operate at a very high temperature. The plots of vessel temperature and buffer temperature shown in the previous sections demonstrate that the thin-walled vessel operates at nearly the same temperature as the high-temperature buffer salt during a reactor accident. After the loss of insulation as described in Chapter 5, there is a marked acceleration of heat loss because the vessel is at a high temperature while the steel liner is hundreds of degrees lower in temperature. This is in contrast to current reactors where the vessel wall remains relatively cool.

13.3 Radiation

Radiation heat transport is significant in preventing fuel failure during a beyond design basis accident. The first attempt at modeling some of the effects of radiation on FHR heat transport as described in Section 11.3 shows that peak temperatures are significantly lower than in cases relying solely on convection and conduction. Furthermore, radiation heat transport between metal surfaces will drive the liner temperature up much faster. This reduces—from 78 to 22 hours between the no radiation and high emissivity radiation cases—the time required to reach the constant temperature liquidus boundary of the BDBA salt and the time required to melt enough BDBA salt into the cavity to aid in liquid convection heat transfer.

Table 13.1 shows the component temperatures at the most critical times in each case's

Temperature (° C)	Convective Air (Large Cavity)	Convective Air & Circulating Salt (1m Annular Air Gap)	With Radiation ($\epsilon = 0.3$)
Core	1395	1294	932
Buffer	1327	1260	789
Buffer Vessel	1320	1253	779
Air	728	753	727
Liner	518	454	703
BDBA Salt	452	452	452
Time (sec)	1.6×10^6 (18.5 days)	1.25×10^6 (14.5 days)	93375 (26 hours)

Table 13.1: Peak System Temperatures at Critical Times with Varying Phenomena.

accident sequence. The first two columns show peak temperatures in cases if there was no radiation heat transfer: the first column is with the large air cavity and the second column is with the small air cavity. The final column is the radiation case with $\epsilon = 0.3$ from Section 11.3. Recall from Figure 9.7 that the peak system temperatures in the base case occur at 1.6×10^6 seconds, which equates to 18.5 days. In the smaller air cavity case, by referencing Figure 10.3, one sees the highest temperatures at the time when the BDBA salt begins to significantly melt at 1.25×10^6 seconds (14.5 days) as discussed in Chapter 10. In the radiation case, the peak core temperature is reached early, but due to radiation heat transport, the steel liner continues to heat, as does the air, buffer, and outer vessel until the BDBA salt becomes a constant temperature boundary as in Figure 11.3. This occurs at $t = 93375$ seconds, or 26 hours.

Radiation will also significantly assist in degrading and/or failing the insulation. Since surface-to-surface radiation exchange between metals with parallel view factors is shown to be high, the temperature of the insulation is expected to rise quickly during a beyond design basis accident. This will greatly accelerate the temperature rise of the insulation thereby allowing it to reach a Curie point or fusible link melting temperature quickly. This is required to realize the high ΔT described in Section 13.2 to drive heat from the core.

Note the core temperature differences in each of the cases presented in Table 13.1. Radiation heat transfer has the potential to lower peak temperatures by hundreds of degrees Celsius. Recall that fuel failure is expected to occur at nearly 1650° C. The primary coolant is expected to boil around 1450° C. As long as the coolant remains liquid—that is, remains under 1450° C—large-scale fuel failure should not occur. In the radiation case, peak core temperatures barely rise over 930° C in the simulations presented with the 1047 MW_{th} core design. This could allow for a significant a power increase while still preventing fuel failure in a worst-case accident scenario.

Last, radiation drastically changes the melting dynamics of the BDBA salt. If considering only *convective* air flow, salt starts melting near the top of the silo. With radiation, salt starts melting at the midpoint. Furthermore, the temperature gradient in the BDBA salt is expected to be minimal (refer to Figure 11.5(b)), so that the BDBA salt should start melting nearly uniformly throughout its volume. This is significant in that it will prevent "pooling" in one location of the salt or other unanticipated melting behaviors that prevent the salt from fully melting into the cavity. Moreover, liquifying the salt nearly uniformly will create natural circulation currents that transport heat upward in the salt column and in the cavity that it fills.

13.4 BDBA Heat Sink

The BDBA salt, modeled in this report as FLiNaK, is a large heat sink. During the initial part of the beyond design basis accident, any heat that conducts through the steel liner to this BDBA salt will cause its temperature to rise. However, upon reaching the liquidus temperature, this structure of BDBA salt acts as a constant temperature boundary for a *long* period of time–until enough energy is input to overcome the heat of fusion. This places an *upper limit* on the outer temperature of the steel liner, and keeps the ΔT between

the hot FHR outer vessel and the BDBA salt as large as possible to drive heat away from the core.

Furthermore, the BDBA salt acts as a even more prolific heat sink if and when enough energy is input to the salt to melt the salt in enough quantity to contact the FHR vessel. This was modeled in the 4m air cavity case. When this occurs, not only is there a constant temperature boundary at the outer radius of the BDBA salt, but there is now liquid convection between the FHR vessel and the steel liner. Since the steel liner is kept at a temperature near the BDBA salt liquidus temperature (due to the constant temperature boundary), the circulating BDBA salt in the cavity will lower the temperature of the vessel, which, in turn, will lower and mitigate the peak temperature in the core.

13.5 Upward Heat Transport to Atmosphere

Although convective air currents are shown to transport a limited amount of heat, the convection of air from the buffer vessel is preferentially upward as illustrated in Figure 9.5(a). This is why the temperatures are hotter in the upper regions of the FHR as shown in Figure 11.5(a). The radiation case does show the same behavior as seen in Figure 11.4. The upward transport of heat greatly aids in heat conduction to the environment. The upper boundary is modeled as 1 meter of concrete (the silo) on the top of which is a *constant temperature* boundary at 300 K (25° C) which is standard atmospheric temperature. This is much less resistance than transporting through a couple inches of steel to a higher temperature boundary (at BDBA salt liquidus temperature) that is experienced in the radial transport of heat.

13.6 Concrete Temperatures and Behavior

With the BDBA salt held at a constant temperature once it reaches its liquidus temperature, the concrete silo's inner radius will also be subject to the same temperature boundary condition. If this persists for a long period with no silo cooling system in operation, then a temperature profile as seen in Figure 6.7 would be realized. Temperatures in the concrete could approach 300° or even 400° C.

Although concrete temperature profiles were modeled in this report, the physical behavior of the concrete was not. High concrete temperatures could result in catastrophic failure of the silo or generation of gaseous byproducts. This will require careful thought on concrete selection and design. This is covered in more detail in Section 14.5.

13.7 Design Space

While this is a first comprehensive review showing the Fluoride Salt Cooled High Temperature Reactor's feasibility of preventing large scale fuel failure during a beyond design basis accident with *no* active cooling systems available, there are myriad unknown variables that have an effect on the system to remove decay heat. These are covered in Appendix D.

Chapter 14

Future Work

14.1 Radiation Heat Transport

The modeling indicates the dominant impact of radiation heat transport on peak fuel temperatures. This makes *better understanding of radiation heat transport* a high priority in the FHR.

A multiband thermal radiation model makes it possible to simulate diffuse and specular radiation that is dependent on wavelength or frequency. With this model, wavelength bands specify radiation properties of the media and surrounding surfaces. The number and extents of the bands are chosen to describe property variations with respect to wavelength. During the solution process, the governing radiation equations are solved for each defined band using the specified properties. The total radiation solution is then obtained by integrating (summing) the solutions from each of the individual bands.

Future work will need to analyze the spectral dependence of emissivity, absorptivity, reflectivity, and transmissivity of the metal surfaces as well as the surrounding components (like the concrete silo) and the air and salt solutions. Since these coefficients are dependent

on temperatures, materials, material quality and finish, and geometry, much of this analysis and experimentation will need to occur in the latter stages of FHR design. This is especially true if using oxidized metal surfaces, which are known to have large spectral dependencies.

In some cases, thermal radiation can occur only as a surface phenomenon. The media separating the surfaces (such as dry air) is transparent to thermal radiation. However, other applications require consideration of the participating media. This term refers to media lying *between* the radiating surfaces that can absorb, emit, and/or scatter thermal radiation.

The buffer salt is expected to fill the space between the core vessel and the buffer vessel. This must be modeled as a participating media, as the salt will be a semi-transparent media with respect to radiation energy transfer. This is a complicated problem, as it depends on the configuration of the salt, the purity of the salt, and the temperatures at which it is operating. During an accident, temperatures will be rapidly changing, and depending on the accident sequence, chemical makeup could change because of high temperature decomposition or introduction of impurities due to high temperature phenomena such as localized vessel failure. Future work will include understanding the effect of all the salt fluids on radiation transfer.

14.2 Convective Air Circulation

It is still widely acknowledged that adequate models capturing the turbulence effects of high-Rayleigh number flows are not available [4]. High Rayleigh number flows are associated with strong natural convection, and are considered any flow for which $Ra > 10^9$. Appendix A shows that many of the Rayleigh numbers in the FHR beyond design basis accident scenario are near 10^{11}. Until more accurate and/or more computationally permissive simulation capability of natural convection flows is available, experimentation using a

scaled FHR mockup will be required to quantitatively demonstrate more accurate natural convection phenomena.

14.3 BDBA Salt Selection

The economic viability and system performance depends on the salt. This study used a fluoride salt with known properties; however, this is an expensive option. A detailed study is required to determine the optimum salt. Recent work on advanced high-temperature (700° C) solar collectors may provide candidate salts [27].

14.4 BDBA Salt Melting: Two-Phase Interface Tracking

Accurate multi-phase phenomena tracking is extremely difficult as discussed in Section 6.4. This report assumed an outer constant temperature boundary until the BDBA salt average temperature reached its liquidus temperature, then assumed a constant temperature boundary on the outside of the liner. Finally, when the energy input into the BDBA was sufficient to melt a significant portion of the salt, the FHR was modeled with a vessel immersed in the circulating, melted BDBA salt. Future simulations and/or experiments will need to track the temperatures during the dynamic process of the FHR air/gas cavity filling with BDBA salt, as this will be a slow, steady process. Temperature distributions in the vessel and core should be monitored, as lower temperatures may exist in the lower regions when the BDBA salt has filled the bottom of the cavity, but has not affected the top portions, for instance.

14.5 Concrete Modeling and Selection

With a constant temperature boundary on the inner radius of the concrete silo of a few hundred degrees Celsius, the silo will rise significantly in temperature over a long period of time if no cooling is provided to it. Since this will have an effect on the silo and the surrounding components—including the BDBA salt structure—it is imperative to select a concrete that can best withstand high temperatures.

Fortunately, high temperature concrete that can withstand harsh high-temperature environments is in use in industries such as steel manufacturing. Controlling the aggregate—which is the majority of the material in concrete—gas generation can be greatly mitigated. Use of granite and volcanic aggregate, for instance, does not generate gas. In this case, gas is generated only in the cement (the minority constituent). Furthermore, steam curing of concrete in prefabricated silo sections is a promising option to remove excess water from the cement.

14.6 Integrated Model

This work is an initial examination of a BDBA system that provides an understanding of the important physical effects and design parameters. It is not a fully integrated model. Much additional work will be required to develop the data and required design tools for a realistic design.

14.7 Experimental Validation of Models

The uncertainties in radiation heat transfer, two-phase salt melting dynamics, and determining air heat transfer coefficients under high Rayleigh-number natural convection flows

makes experimental work desirable. Fortunately, it should be possible to carry out a scaled experiment to verify radiation heat transfer and natural convection dynamics. Such a setup does not involve nuclear radiation. It could be carried out with existing power sources and heating capabilities in existing university laboratories. It should be feasible to determine experimental correlations of the modes of heat transfer realized and ultimately demonstrate that the BDBA heat removal system can safely remove expected decay heat loads. Proving this capability for a relatively low investment with existing laboratories and equipment will then extend to a full scale experimental apparatus in the long term.

Appendix A

Validating the STAR-CCM+ Analysis with No Radiation

From the ANS decay heat curve, one can find the total heat input into the core. For the first 400 seconds:

$$E_{\text{core,400 s}} = \int_0^{400} -6.15 \times 10^{-3} \log(t_s)\, \mathrm{d}t = 11.801 \cdot P_{100\%} \tag{A.1}$$

Then from 400 seconds through 4×10^5 seconds:

$$E = \int_{400}^{t} 1.41 \times 10^{-1}\, t'^{(-0.285)}\, \mathrm{d}t' = 0.197\, t^{(0.714)}\Big|_{400}^{t} \cdot P_{100\%} \tag{A.2}$$

Region	Volume (m^3)	Outer Surface Area (m^2)
Core	0.773	1.83
Core Vessel	0.095	1.95
Buffer	9.96	9.24
Steel Vessel	0.46	9.49
Air	57.49	22.9
Liner	1.15	10.8
BDBA Salt	10.8	24.8

Table A.1: Surface Areas and Volumes of the Modeled FHR.

For the modeled 15° section of the FHR in STAR-CCM+, the regions have the surface

area and the volume listed in Table A.1.

The properties listed in Table A.2 for the salts at 700°C is also pertinent:

Salt	Density ρ (kg/m^3)	Specific Heat Capacity (J/kg-K)	Volumetric Heat Capacity ($J/kg\text{-}m^3$)
flinak	2019	1620	3.27×10^6
flibe	1921	2380	4.57×10^6

Table A.2: Heat Capacity of Salts.

Since the geometry of the core and buffer salt tank is a cylinder (with a very small portion being a hemispherical head at the bottom), a simplified approximation of the thermal resistance (and average heat flux) can be approximated by using a cylindrical approach starting with the one-dimensional heat equation (by ignoring the upward heat flow):

$$\frac{1}{r}\frac{d}{dr}\left(kr\frac{dT}{dr}\right) = 0 \tag{A.3}$$

Fourier's law is used to determine the energy conducted across a cylindrical surface:

$$q_r = -KA\frac{dT}{dr} = -k(2\pi rL)\frac{dT}{dr} \tag{A.4}$$

Assuming a constant k in any material, integrating Equation A.3 twice and combining with Fourier's law results in the heat transfer rate and the heat flux:

$$q_r = \frac{(2\pi Lk)(\Delta T)}{\ln(r_2/r_1)} \tag{A.5}$$

$$q_r'' = \frac{k\Delta T}{r\ln(r_2/r_1)} \tag{A.6}$$

	Core Vessel	Buffer	Buffer Vessel	Air Cavity	Steel Liner
Outer (r_2) (m)	1.0	2.95	3	6	6.05
Inner (r_1) (m)	0.95	1.0	2.95	3	6
Conductive Heat Flux (W/m^2)	292 ΔT	0.277 ΔT	297 ΔT	0.02 ΔT	300 Δ T

Table A.3: Radii of and Heat Tlux Through FHR Components.

The appropriate radii and heat flux for the different parts of the FHR are listed in Table A.3:

In addition to conduction through the surfaces, heat transfer will be aided by convection from the fluid salts to the solid vessels. As discussed in section 8.3, the free convection correlations for turbulent free convection (i.e. Rayleigh numbers over 10^9) are not well established. Use of correlations that are accepted in the engineering community [1, p. 605] for Rayleigh numbers under 10^9 are used to make a first approximation of convective heat transfer. As the Rayleigh number increases, the convective flow will transition into a fully turbulent region, which should significantly increase the convective heat transfer along the vessels.

Convection heat transfer is calculated by using an overall heat transfer coefficient for a surface. This is approximated using the *Nusselt number* and the following correlation:

$$\overline{Nu}_L = \frac{\overline{h}L}{k} \tag{A.7}$$

where the overbar indicates the average conditions over the surface. The difficulty lies in approximating the Nusselt number. For forced convection there are numerous correlations that are used depending on conditions [1, 29]. For free convection with laminar flow (Rayleigh numbers $\leq 10^9$) the following correlation is recommended by Churchill and Chu [2]:

$$\overline{Nu}_L = \left(0.825 + \frac{0.387\,\mathrm{Ra}_L^{1/6}}{\left[1 + (0.492/\mathrm{Pr})^{9/16}\right]^{8/27}} \right)^2 \tag{A.8}$$

The Rayleigh number is the product of the Grashof number and the Prandtl number for free convection flows

$$\mathrm{Ra}_L = \mathrm{Gr}_l\mathrm{Pr} = \frac{g\beta(T_s - T_\infty)L^3}{\nu\alpha} \tag{A.9}$$

where α is the thermal diffusivity discussed in Section 2.2 and is equal to $k/\rho c_p$ (m^2/s). Treating the convective flow as heated vertical plates, the Rayleigh number for each convective interface and the corresponding Nusselt number can be calculated. There are five major convective interfaces being modeled as seen in Figure A.1

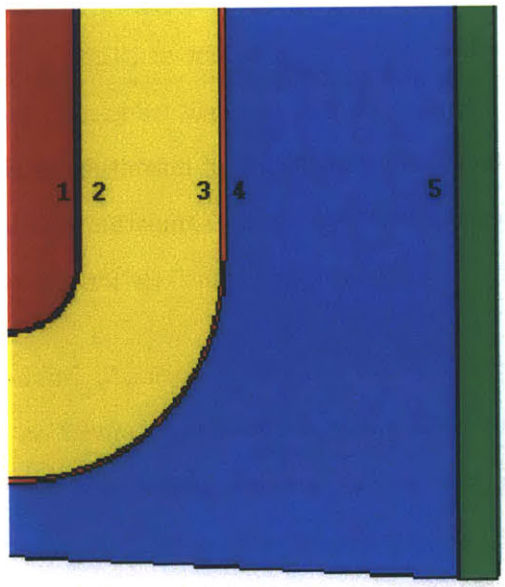

Figure A.1: Convective Interface Boundaries.

Although free convection correlations can not be trusted above 10^9, the calculated values should be the minimum heat transfer coefficient since turbulent heat transfer is

Fluid	k (W/m-k)	ν (m^2/sec)	α (m^2/sec)	Pr ($=\nu/\alpha$)
Flibe	1.0	2.88×10^{-6}	2.19×10^{-7}	13.2
Flinak	0.68	1.44×10^{-6}	1.83×10^{-7}	7.9
Air	0.07	1.22×10^{-4}	1.69×10^{-4}	0.72

Table A.4: Thermophysical Properties of the FHR Fluids.

Part	L_{heated} (m)	Ra	Nu	h (W/m^2-K)
1	6	8.8×10^{10}	652	109
2	6	2.1×10^{11}	843	95
3	10.6	2.3×10^{11}	870	56
4	10.6	3.3×10^{11}	777	4.9
5	14.6	1.1×10^{11}	546	2.5

Table A.5: Heated Lengths and Free Convection Nusselt Numbers (Properties at 700° C).

expected at higher Rayleigh numbers. The heat transfer coefficient is plotted for the air/FHR steel vessel interface in the base case in Figure 9.6. The agreement between the simulation-based average heat transfer coefficient and the correlation based heat transfer coefficient are in the same region. The plotted heat transfer coefficient of approximately 1.3 W/m^2-K from Figure 9.6 is of the same order of magnitude as the predicted 4.9 W/m^2-K using the discussed correlations. However, the simulation also has high-Rayleigh number errors, since correlations are not developed extensively for this type of flow.

Equivalent Conductivity The Russian academician M. Mikheyev proposed a numerical method using an equivalent conductivity for natural convection flows in finite spaces. He stated that heat transfer processes in enclosed finite spaces are complex, and that makes it "practically impossible to elaborate the appropriate laws governing the variation of the heat transfer coefficient separately for the heating and cooling processes" that one would see due to the hot and cold vertical plates.

Mikheyev instead uses a concept of *equivalent thermal conductivity.* He stated that

$$k_{eq} = \epsilon k. \tag{A.10}$$

In other words, an effective thermal conductivity in a natural convection system will allow a heat flux calculation using conductive thermal resistance principles. His work is detailed in Reference [19]. The important relation for comparison is

$$\epsilon = 0.18(Gr \cdot Pr)^{0.25} \tag{A.11}$$

That is, the effective thermal conductivity k_{eq} is a function of the the tabulated thermal conductivity times and fourth root of the Rayleigh number.

For the base case with the 6m radius air gap (and a 3m gap annular distance), recall from Table 9.1 the temperatures of the steel vessel and steel liner are 1023° C and 522° C, respectively, for a ΔT across the gap of 500° C. The air is at 953K, so its volumetric expansion coefficient, β, is 1/973 K. The equivalent thermal conductivity for air in the 3 m gap using the correlation proposed by Mikheyev is

$$Gr = \frac{\beta g \delta^3 \Delta T}{\nu^2} = \frac{9.81 \cdot 3^3 \cdot 500}{953(1.22 \times 10^{-4})^2} = 9.33 \times 10^9 \tag{A.12}$$

$$Ra = Gr\,Pr = 9.33 \times 10^9 (0.72) = 6.7 \times 10^9 \tag{A.13}$$

$$\epsilon = 0.18(6.7 \times 10^9)^{0.25} = 51.5 \tag{A.14}$$

$$k_{eff} = 51.5(0.067\,\text{W/m-K}) = 3.45\,\text{W/m-K} \tag{A.15}$$

Then, for the 3m annular gap, the heat flux at $t = 281190$ seconds (78 hours) as seen in Figure 9.7(a) should be

$$q'' = \frac{k_{eff}}{\delta_{\text{gap}}}\Delta T = \frac{3.45\,\text{W/m-K}}{3\,\text{m}}(500^\circ\,\text{C}) = 575\,\text{W/m}^2 \tag{A.16}$$

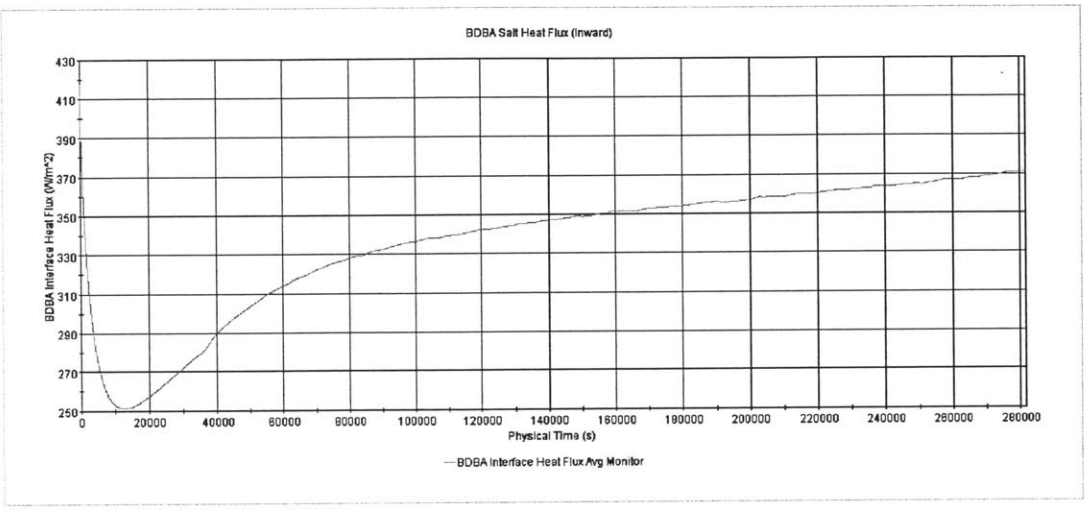

Figure A.2: Heat Flux Into the BDBA Salt in the Base (6m Air Cavity Radius) Case with No Radiation.

This completely different approach to approximating heat transfer in an enclosed space with natural convection flow shows the same level of agreement as correlating the heat transfer coefficient with a Nusselt number correlation in the previous paragraphs. The calculated value using Mikheyev's method is 575 W/m^2 through the air gap into the BDBA salt; the STAR-CCM+ model predicts just higher than 370 W/m^2 at the same point in time in Figure A.2 In agreement with today's literature that states capturing free convection effects with $Ra > 10^9$ is difficult, Mikheyev states that capturing all the effects is nearly impossible [19, p. 82]. However, this approach shows that the simulated results of convection and correlation are in the approximate range that would be expected by the simplistic calculations shown to be reasonably accurate by Mikheyev.

Summary All three major heat transfer mechanisms—conduction, convection, and radiation—are taking place during a BDBA in the FHR. It is well-known in the thermal-hydraulics community that capturing many free convection flows remains a significant challenge. Correlations that are established—from the most recent Nusselt-number correlations to the older equivalent thermal conductivity methods—show that the simulated results are within the expected ranges of heat transfer capability. Clearly, this report shows that radiation is the dominant heat transfer mode and drives the BDBA sequence. Further work required for both the natural convection and FHR radiation is discussed in Chapter 14.

Appendix B

Validating the STAR-CCM+ Conduction Model

A large part of the heat transfer model for the beyond design basis accident (BDBA) is the conduction of heat through the (mainly) concrete silo. In order to have reasonable confidence in the conduction results, the conduction model of the software should be validated against a known test case.

B.1 Validating a 1-D Time-Varying Heat Conduction Case

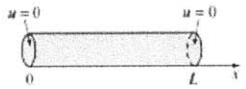

Figure B.1: Temperatures in a Rod of length L [33].

Consider a rod of lenth L with an initial temperature $f(x)$ throughout and whose ends are held at temperature zero for all time $t > 0$. If the rod shown in Figure B.1 satisfies the assumptions listed here:

- The flow of heat within the rod takes place only in the x-direction.

- The lateral, or curved, surface of the rod is insulated; that is, no heat escapes from the surface.
- No heat is being generated within the rod.
- The rod is homogeneous; that is, its mass per unit volume ρ is constant.
- The specific heat γ and thermal conductivity k of the material of the rods are constants.

then the temperature $u(x,t)$ in the rod is determined from the boundary-value problem [33]:

$$k\frac{\partial^2 u}{\partial x^2} = \frac{\partial u}{\partial t}, \quad 0 < x < L, \quad t > 0 \tag{B.1}$$

$$u(0,t) = 0, \quad u(L,t) = 0, \quad t > 0 \tag{B.2}$$

$$u(x,0) = f(x), \quad 0 < x < L \tag{B.3}$$

Solving the Model

To start, use the product $u(x,t) = X(x)T(t)$ to separate the variables in (B.1). Then, if $-\lambda$ is the separation constant, the two equalities

$$\frac{X''}{X} = \frac{T}{kT} = -\lambda \tag{B.4}$$

lead to the ordinary differential equations

$$X'' + \lambda X = 0 \tag{B.5}$$

$$T' + k\lambda T = 0 \tag{B.6}$$

Before solving (B.5), note that the boundary conditions (B.2) applied to $u(x,t) = X(x)T(t)$ are

$$u(0,t) = X(0)T(t) = 0 \quad \text{and} \quad u(L,t) = X(L)T(t) = 0.$$

Since it makes sense to expect that $T(t) \neq 0$ for all t, the foregoing equalities hold only if $X(0) = 0$ and $X(L) = 0$. These homogeneous boundary conditions together with the homogeneous differential equation (B.5) constitute a regular Sturm-Liouville problem:

$$X'' + \lambda X = 0, \quad X(0) = 0, \quad X(L) = 0 \tag{B.7}$$

The solution of this boundary value problem is given by

$$X(X) = c_1 \cos(\alpha x) + c_2 \sin(\alpha x) \tag{B.8}$$

When $X(0) = 0$ is applied to Equation B.8, $c_1 = 0$ and $X(x) = c_2 \sin(\alpha x)$. The second boundary condition then implies that $X(L) = c_2 \sin(\alpha x) = 0$. To obtain a non-trivial solution, $c_2 \neq 0$ and $sin\, \alpha L = 0$. The last equation is satisfied when $\alpha L = n\pi$ or $\alpha = n\pi/L$. Hence, (B.7) possesses nontrivial solutions when $\lambda_n = \alpha_n^2 \pi^2 / L^2$, $n = 1, 2, 3, \ldots$. These values of λ are the **eigenvalues** of the problem; the **eigenfunctions** are

$$X(x) = c_2 \sin\left(\frac{n\pi}{L} x\right), \quad n = 1, 2, 3, \ldots \tag{B.9}$$

From (B.6), $T(t) = c_3 e^{-k(n^2\pi^2/L^2)t}$, so

$$u_n = X(x)T(t) = A_n e^{-k(n^2\pi^2/L^2)t} \sin\left(\frac{n\pi}{L} x\right), \tag{B.10}$$

where the constant $c_2 c_3$ has been replaced by A_n. Each of the product functions $u_n(x,t)$

given in (B.10) is a particular solution of the partial differential equation (B.1), and each $u_n(x,t)$ satisfies both boundary conditions (B.2) as well. However, for (B.10) to satisfy the initial condition (B.3), one would have to choose the coefficient A_n in such a manner that

$$u_n(x,0) = f(x) = A_n \sin \frac{n\pi}{L}x. \tag{B.11}$$

By the superposition principle, the function $u(x,t) = \sum_{n=1}^{\infty} u_n$ or

$$u(x,t) = \sum_{n=1}^{\infty} A_n e^{-k(n^2\pi^2/L^2)t} \sin \frac{n\pi}{L}x \tag{B.12}$$

must also, although formally, satisfy equation (B.1) and the conditions in (B.2). Substituting $t = 0$ into (B.12) implies that

$$u(x,0) = f(x) = \sum_{n=1}^{\infty} A_n \sin \frac{n\pi}{L}x.$$

This last expression is a half-range expansion of f in a sine series. It follows that

$$A_n = \frac{2}{L}\int_0^L f(x) \sin \frac{n\pi}{L}x \, dx. \tag{B.13}$$

The solution of the boundary-value problem described in (B.1), (B.2), and (B.3) is given by the infinite series

$$u(x,t) = \frac{2}{L}\sum_{n=1}^{\infty}\left(\int_0^L f(x) \sin \frac{n\pi}{L}x \, dx\right) e^{-k(n^2\pi^2/L^2)t} \sin \frac{n\pi}{L}x \tag{B.14}$$

If the initial temperature us $u(x,0) = 100, L = \pi$, and $k = 1$, the coefficients of (B.13) are given by

$$A_n = \frac{200}{\pi}\left[\frac{(1-(-1)^n)}{n}\right]$$

and (B.14) is

$$u(x,t) = \frac{200}{\pi} \sum_{n=1}^{\infty} \left[\frac{(1-(-1)^n)}{n} \right] e^{-n^2 t} \sin nx \tag{B.15}$$

Validating the solution

To verify that STAR-CCM+ models conduction accurately a 2 dimensional heat rod of 3.14 meters length and 0.1 meters heigh was constructed and meshed. The thermal conductivity of the solid was set to 1 W/m-K, and the results are plotted in Figure B.2
The solution is plotted analytically in Figure B.3 using a MATLAB script to evaluate the temperature distribution of Equation B.15.

There is excellent agreement with the STAR-CCM+ results and the MATLAB script, which validates the use of STAR-CCM+ computational fluid dynamics modeling through solid surfaces of known constant thermal conductivities, such as the steel liners and vessels used in the FHR.

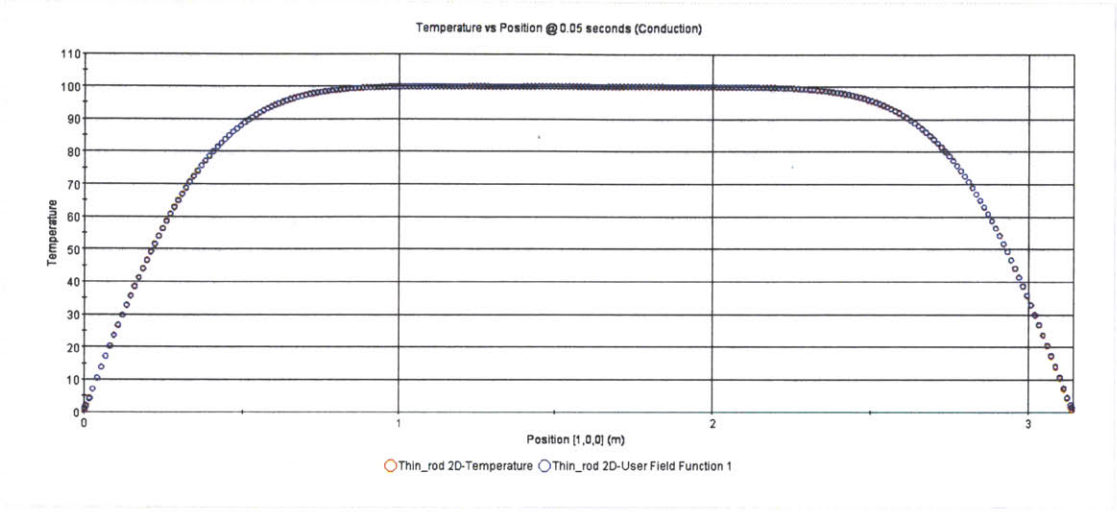

(a) t=0.05 sec

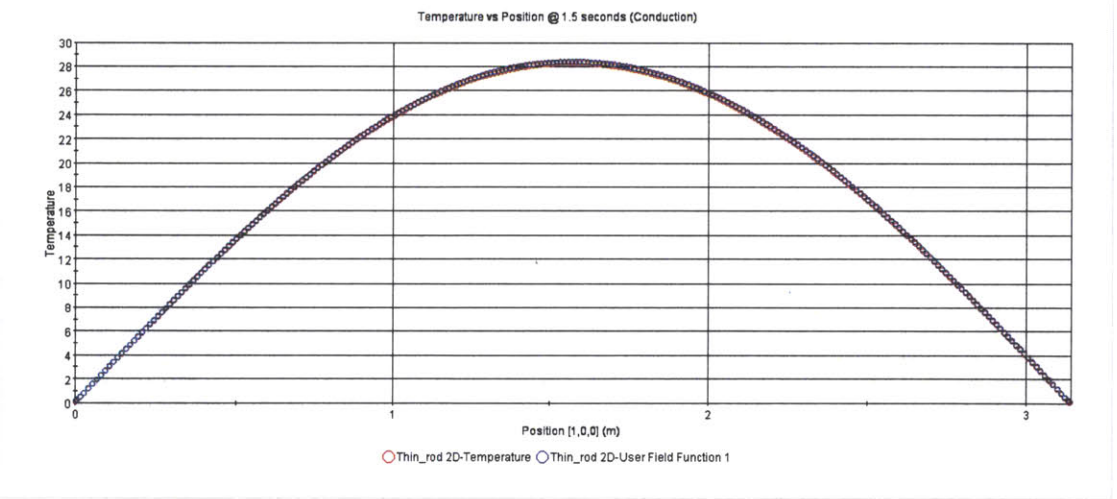

(b) t=1.5 sec

Figure B.2: Temperature Distribution in a Thin Rod vs Position for Varying t.

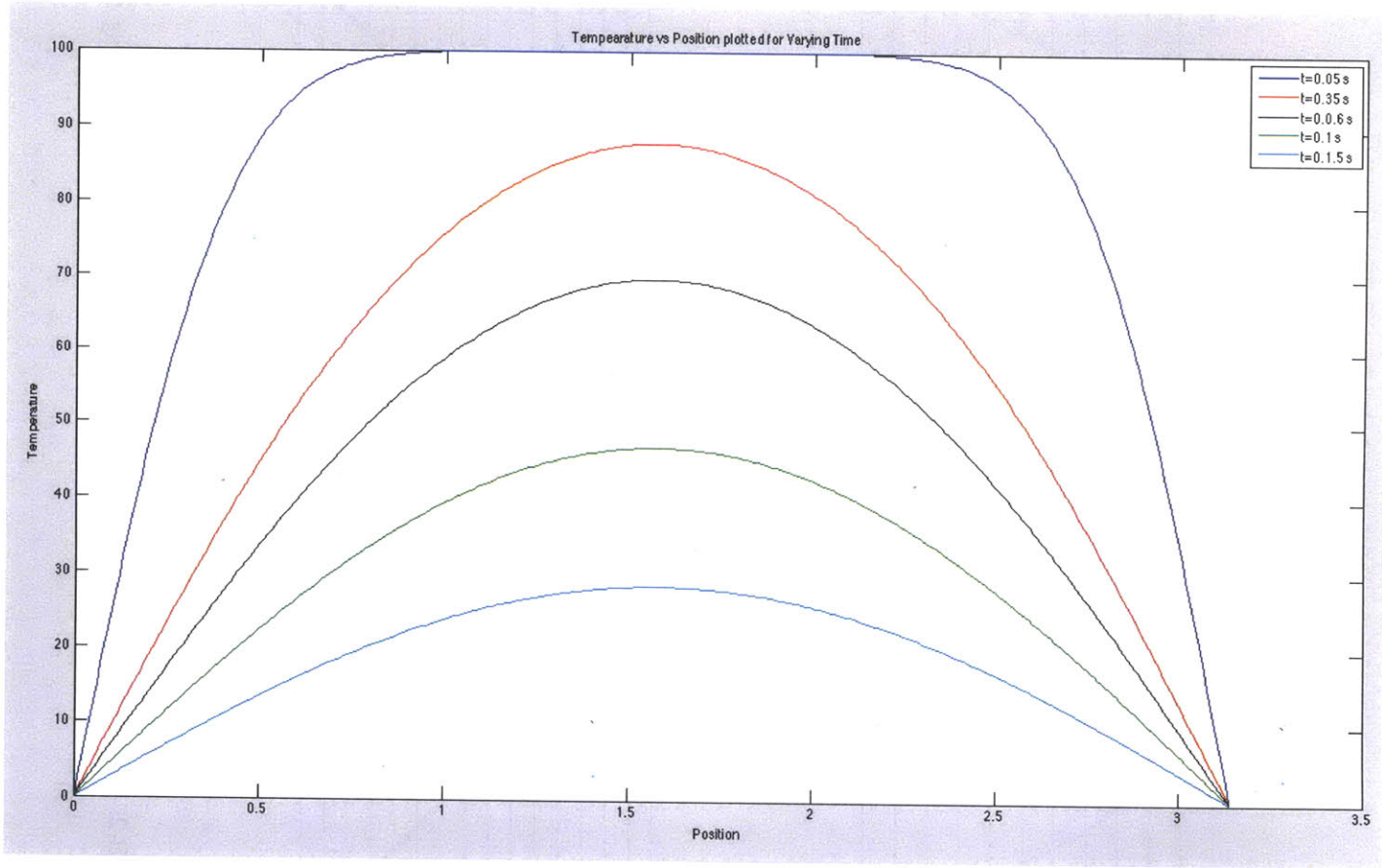

Figure B.3: Positional Temperature Distribution in a Thin Rod.

Appendix C

Creating and Validating the Total Energy Input in STAR-CCM+

An important phenomenon to monitor in the FHR beyond design basis accident scenario is the total energy input into the BDBA salt upon reaching its liquidus temperature. With knowledge of its latent heat of fusion and knowledge of the energy input into the BDBA salt, it is possible to determine the amount of salt that melts. This is essential to evaluate when the FHR vessel comes into contact with the liquid BDBA salt and aids the heat transfer from vessel to the outer dimensions of the FHR.

STAR-CCM+ does not integrate many functions with time. A modeler can easily monitor a quantity such as heat flux over time and see a heat flux plot as in Figure 9.9. STAR-CCM+ is also set up to integrate quantities with respect to space. For example, performing a surface integral of the Heat Flux will give the total heat rate (in Watts) entering a surface. Likewise, a volumetric heat source (W/m^3) can be integrated using STAR-CCM+'s volume integral function to find the total heat source (Watts) in the core at any given time.

In order to make a rigorous evaluation of total energy (not heat rate) in Joules that cross a boundary or enter a volume, an integral with respect to time must be created by

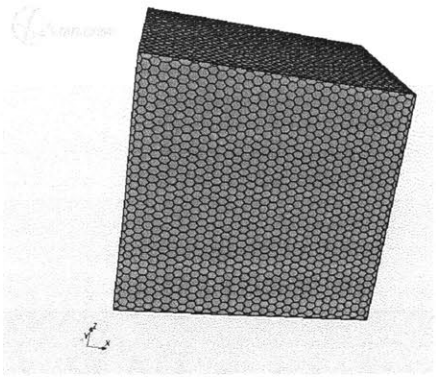

Figure C.1: A 2 meter Cube.

the user. This is done using a test case. A cube with side 2 meters was constructed for a case that can be evaluated analytically as in Figure C.1.

All boundaries are set as adiabatic boundaries with the exception of one square face of 2 meter length. The heat flux was fixed on this face and linearly time-varying with the function $q''_{\text{in, face}} = 100t$. The system was evaluated for 360 seconds.

The heat flux and total heat rate were calculated using STAR-CCM+'s functions of *surface average* and *surface integral* of the heat flux across the boundary. Though the heat flux was set as $100t$ W/m^2 for the entire face, in the FHR, vertical temperature distributions will ensure that the heat flux varies with the vertical coordinate. STAR-CCM+ is able to total the entire heat rate (by summing heat flux in each mesh volume and multiplying it by the surface area) and dividing by the total surface area. The surface integral, then, is the summation of heat flux on a mesh surface multiplied by the mesh surface area and summed for the entire mesh on a surface. These are illustrated for this test case in Figure C.2. Note that the values are negative because it is heat into the boundary; this is the convention used in the STAR-CCM+ software.

The issue arises in determining the total energy input into the cube. With heat entering

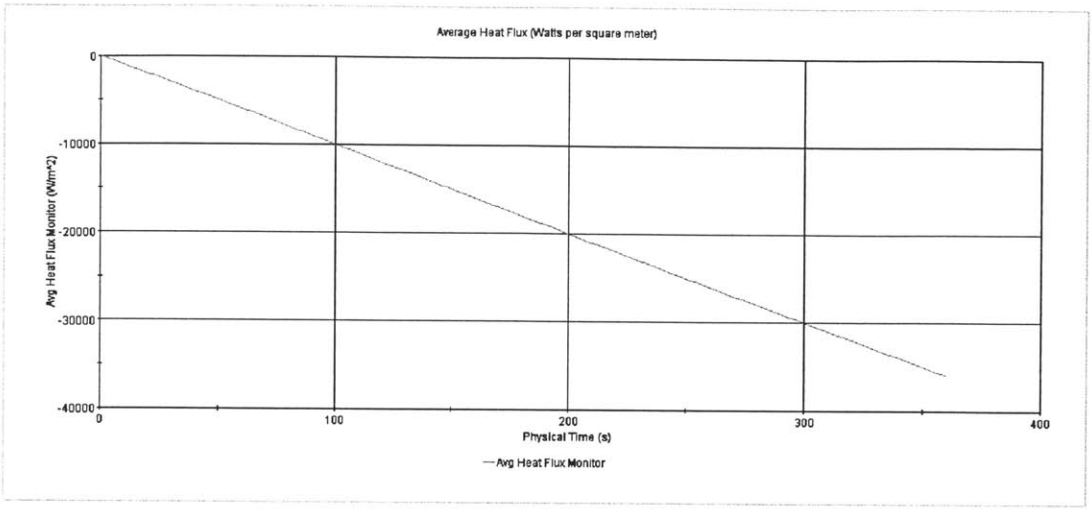

(a) Average Heat Flux

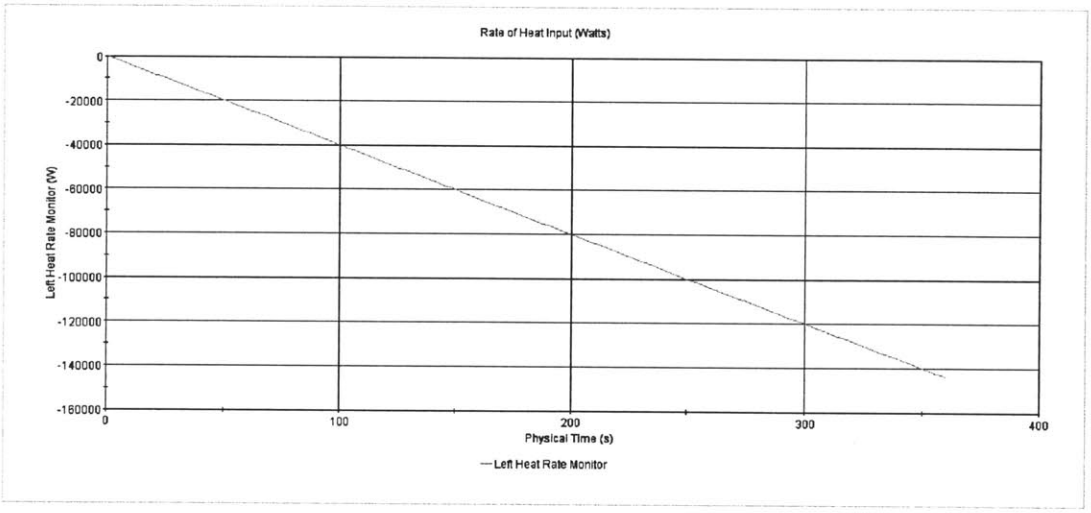

(b) Average Heat Rate

Figure C.2: Average Heat Flux and Rate in the 4m^2 test case.

only through one surface, and a known heat flux of $100t$ W/m^2, the heat rate and the total energy in can be determined analytically:

$$q'' = 100t\,\mathrm{W/m^2} \tag{C.1}$$

$$q = \int_A q''\,\mathrm{d}A = 100t\,\mathrm{W/m^2}(4\,\mathrm{m^2}) = 400t\,\mathrm{W} \tag{C.2}$$

$$E_{in} = \int_{t_o}^{t_f} q\,\mathrm{dt'} = \int_0^t 400t'\,\mathrm{d}t' = 200t^2\,\mathrm{J} \tag{C.3}$$

This is accomplished in STAR-CCM+ manually by the user. A monitor is created of the heat rate (in Watts) through the surface by performing a surface integral of the Heat Flux, which is a primitive field function built into the modeling package. This creates a report which the software will track. The next step is for the modeler to *create* a field function of the energy that is input in each discrete time step. This is accomplished by making a field function with the following syntax:

```
$HeatRateReport * $TimeStep
```

Then a summation of the energy input in each time step must be performed using the *field sum* monitor option in the software package. This sums the energy input in each time step. Finally, by creating a field function of the field sum, the user has built into the software an integral with respect to time of the heat rate, and the result is the total energy input into a surface; likewise, the same can be done with volume functions for a volumetric heat source.

The results of the energy input monitor are shown in Figure C.3 for both the STAR-CCM+ calculated energy input (through the field functions) drawn in a solid red line and in analytical format. The analytical values are determined by using a MATLAB file for Equation C.3, saving the results as a comma separated value table, and importing the data into the STAR-CCM+ modeling software.

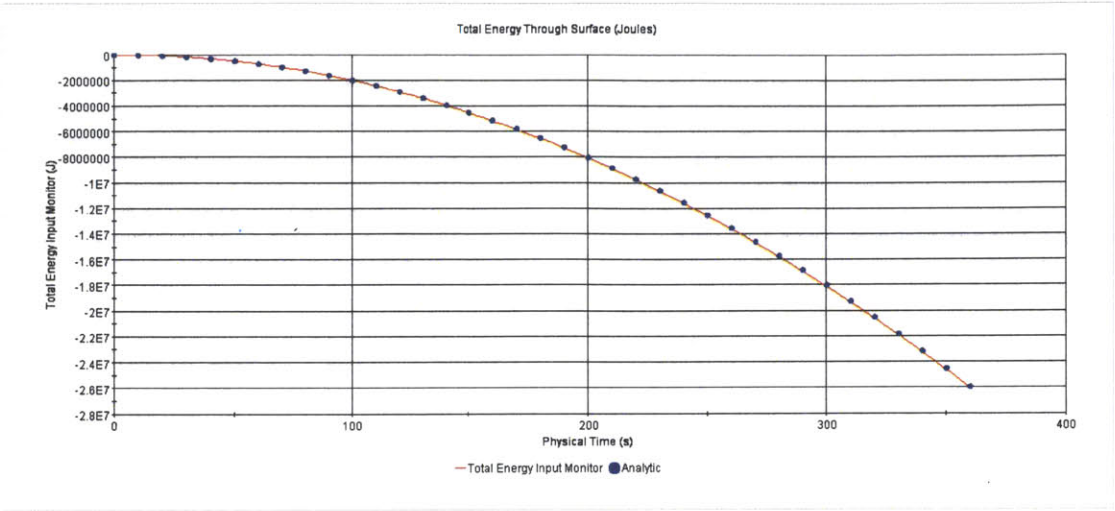

Figure C.3: Total Energy Input for the Test Case.

Finally, to ensure that the field sum monitor works to calculate the energy input regardless of the time step size, the test case presented has a varying time step size. That is, it is run with a 1 second time step for the first 180 seconds of simulation, and a 2 second time step for the remainder of the case. The graph of Figure C.3 shows that the energy input curve is a smooth curve that follows the analytic solution regardless of the time step.

Appendix D

FHR Design Space

This report was the first comprehensive look at the FHR's ability to prevent fuel failure in a complete reactor accident. Since the FHR design is in its nascent stages, many (reasonable) assumptions were made to examine if preventing a large scale radionuclide release is even feasible. While this report shows that keeping all temperatures less than fuel failure is a reasonable assumption–at least with the modest power generating capacity assumed in this report—the design space of the FHR is large and many factors will have an effect on the BDBA scenario.

D.1 Silo Thickness

A one meter thick concrete silo was modeled surrounding the FHR. The material was modeled as Portland cement. The thickness of the silo directly affects the thermal resistance to conduction from the air cavity to the upper atmosphere and from the steel liner and BDBA salt to the surrounding Earth.

D.2 Vessel Thicknesses and Materials

A steel vessel of 5 cm (approximately 2 inches) was modeled surrounding the flibe primary coolant in the core and the FLiNaK buffer salt. A 5 cm thick steel liner was also modeled surrounding the air cavity on the inside of the BDBA salt. Use of thin vessels and liners allows the ΔT across the vessel to be minimal. This will allow the outer surface of the FHR vessel to be as hot as possible in order to set up the largest possible temperature gradient between the vessel and the steel liner. Thicker vessels will cause more resistance the thermal conduction, and will cause some thermal fatigue due to temperature gradients within the vessel.

The material used will have two effects on the BDBA system. The material's thermal conductivity directly affects its ability to conduct heat through the vessel. The material's strength properties will determine how thick the vessel needs to be to withstand any stresses developed within the system. Weaker materials will require thicker vessels, and more resistance to heat transfer.

D.3 Gas Cavity

A gas cavity surrounds the FHR vessel. This cavity nominally has a *large* thermal resistance during normal operation. It is desirable to operate the FHR as hot as possible with minimal losses to the environment. This gap minimizes heat transfer to the outer surfaces. Furthermore, the outer surface is lined with layers of insulation to prevent heat transfer during normal operation.

D.3.1 Size

The difference between the 6m and 4m air cavity cases provides insight into the dynamics of changing this gas cavity. Increasing the size of the gap will prolong the time until the BDBA salt reaches its liquidus temperature. It will absorb more heat within the cavity. However, due to the low volumetric heat capacity of air, this is detrimental. In Section 9.1, peak core temperatures of 1400° C were observed. Compare this to the peak temperatures nearer 1300° C seen in Figure 10.3 in Section 10. Reducing the size of the outer radius of the annular air gap has positive effects in the overall BDBA scenario.

D.3.2 Contents

This report used air in the gap. It may be worthwhile to explore alternative gases to fill this gap. There is a tradeoff between low thermal conductivity—desired during normal operation—and higher thermal conductivity which would be desired during a beyond design basis accident. Furthermore, air is easiest to obtain; any other gases would incur additional costs. Meanwhile, radiation is so much more dominant of an effect that pursuing increased gas conductivity is not likely to be worthwhile endeavor.

D.4 BDBA Salt

This analysis modeled the frozen BDBA salt location outside the steel liner and inside the concrete silo as illustrated in Figure 4.1. With the BDBA salt interfacing with the silo cooling system, the actual temperature of the frozen salt should be near atmospheric temperature under normal design operating conditions. Since this accident model assumed complete silo cooling failure and a complete loss of insulation the starting temperature for the BDBA salt was chosen as 300° C. However, more complex models will need to include

the insulation failure and a BDBA salt starting temperature near 25° C that commences with silo cooling in normal operating status. In this case, the amount of heat removed to the BDBA salt is actually *greater* than modeled; the models within this report are conservative.

The BDBA salt could alternatively be designed between the insulation and steel liner (refer to Figure 4.1) with the cooling jacket outside the steel liner between the liner and the concrete silo. In this case, the outer liner would be kept near 25° C, and the BDBA salt would melt faster during a BDBA since no heat would need to conduct through the steel liner to reach the BDBA salt. This would also allow the BDBA salt to be a warm thermal mass that reduces the risk of accidental freezing of the salt coolant in the reactor vessel; furthermore, it could serve as a blast barrier for the silo and silo cooling system in a really bad accident—preserving critical cooling. On the other hand, normal operating temperature of the BDBA salt would be much hotter than if it was located outside the liner; it would be much closer to melting during normal operation, especially during a local overheating situation.

D.5 Radiation

The material properties with respect to radiation will have a significant impact on the beyond design basis accident analysis.

D.5.1 Emissivity Control

Based on the tabulated data of emissivities for 316 Stainless Steel and Concrete in Reference [1], constant values were assumed at the 700° C temperature. However, emissivities change with temperature. There is also the possibility of finishing the metal materials with a coating or altering their properties to change emissivities as well as reflectivity and

absorptivity to more desirable values. Emissivity control (or manipulation) will be a factor the designer can use to obtain desirable heat transfer characteristics.

D.5.2 Transmissivity of Buffer Salt and Gas

There will be radiation heat exchange between the core and the outer vessel as well as between the outer vessel to the steel liner. In between the core and the FHR outer vessel is the semi-transparent buffer salt. The selection of this salt and the chemical makeup and concentrations of any impurities contained within this salt will affect the transmissivity. The designer will affect the radiation heat transfer aspect of the accident scenario through chemistry control and salt selection.

D.6 Core

A base core was loosely designed by the author based on a current pebble bed reactor. The design of the core (refer to Figure 2.1) is a tall, narrow core vessel. Changing the parameters of the core greatly affects the core dynamics upon the initiation of a beyond design basis accident.

D.6.1 Surface to Area Ratio

The tall narrow core design (6 meter tall with a 1 meter radius) has a favorable surface to area ratio for *decay heat removal.* Reducing the height of the vessel while keeping the core volume constant (by increasing the radius) reduces the surface area to volume ratio. This is good for neutron economy. An efficient design will want to minimize this ratio. However, during a beyond design basis accident, a larger surface area to volume ratio will maximize the area over which the generated decay heat is transferred *out of the core* and

into the surrounding buffer. Altering the geometry of the core has a significant effect on the peak core temperatures and the ΔT between the core and the buffer salt.

D.6.2 Power Output

The power output of the core affects the peak temperatures in the core. Increasing the power reduces the margin to coolant boiling temperature—and thus reduces the margin to fuel failure. The designer can alter the core power output to obtain desirable margins to fuel failure.

D.7 Buffer

The buffer salt surrounding the core is an integral part of the FHR thermal inertia concept of the beyond design basis accident scenario. The nominal design of the buffer salt is to use an inexpensive salt so the FHR will not be cost-limited in buffer salt quantity.

D.7.1 Geometry

Manipulating the geometry of the buffer salt tank affects the volume of the salt. This affects the overall temperature rise of the buffer salt—and can mitigate the peak temperature in the core. If large amounts of buffer salt are used, the buffer can absorb more energy per degree of temperature rise.

D.7.2 Fluid

The selection of buffer salt fluid has a two-pronged effect: (1) heat capacity and (2) boiling point. Each salt has a different density and heat capacity. Salt choice affects overall volumetric heat capacity. Likewise, each salt has a unique boiling point. Once the buffer salt boils, it no longer can carry heat by liquid convective heat transfer. Keeping the buffer

salt in a one-phase liquid state is a crucial requirement of the beyond design basis accident sequence design.

D.8 Design Space Conclusions

The designer has a plethora of options available to affect the heat transfer capabilities of the FHR in a beyond design basis accident. Geometries of each component, including their surface to volume ratios and amount of fluid they can hold, will greatly affect the system response. Core power output and material selection provide even more options. This reports does show that a beyond design basis accident is survivable with a 1047 MW core assuming planned insulation failure. Manipulation of the variables within this section will allow the designer to change the core power rating and achieve the same (safe) result.

Bibliography

[1] T. L. Bergman, D. P. DeWitt, F. P. Incropera, and A. S. Lavine. *Fundamentals of Heat and Mass Transfer.* John Wiley & Sons, 7th edition, 2011.

[2] S. W. Churchill and H. S. Chu. Correlation equations for laminar and turbulent free convection from a vertical plate. *International Journal of Heat and Mass Transfer*, 18:1323–1329, 1975.

[3] D. Curtis and C. W. Forsberg. Fluoride-salt-cooled high-temperature reactor market strategy with peak electricity and process heat. In *2013 Proceedings of International Congress on Advances in Nuclear Power Plants*, Jeju Island, Korea, 14–18 April 2013. American Nuclear Society.

[4] A. Dehbi, M. Aksouh, and J. Kalilainen. 2D RANS and LES simulations of turbulent flow inside a differentially heated cavity. In *The 15th International Topical Meeting on Nuclear Reactor Thermal-Hydraulics*, Pisa, Italy, 12–17 May 2013. American Nuclear Society.

[5] J. H. Ferziger and M. Perić. *Computational Methods for Fluid Dynamics.* Springer, 3rd edition, 2002.

[6] C. W. Forsberg. Designing the advanced high-temperature reactor for low radionuclide releases in beyond-design basis accidents. In *2008 International Congress on Advances in Nuclear Power Plants (ICAPP '08)*, Anaheim, California, June 8–12 2008. American Nuclear Society, La Grange Park, Illinois.

[7] C. W. Forsberg, L. Hu, T. A. Peterson, and K. Sridharan. Fluoride-salt-cooled high-temperature reactors (FHRs) for power and process heat. Technical Report MIT-ANP-147, Center for Advanced Nuclear Energy Systems, Massachusetts Institute of Technology; Cambridge, MA, January 2013.

[8] C. W. Forsberg, P. F. Peterson, and P. S. Pickard. Molten-salt-cooled advanced high-temperature reactor. *Nuclear Technology*, 144:289–302, December, 2003.

[9] P. Gierszewski, B. Mikic, and N. Todreas. Property correlations for lithium, sodium, helium, flibe, and water in fusion reactor applications. Technical Report PFC-RR-80-12, Fusion Blanket and Structures Group, Massachusetts Institute of Technology; Cambridge, MA, August 1980.

[10] Transco Products Inc. Metal reflective insulation. "http://www.transcoproducts.com/metal_reflective_insulation.htm., 14 January 2013.

[11] ASM International. ASM AISI type 316 material data sheet. *Engineering Properties of Steel*, 1982.

[12] ASM International. Stainless and heat-resisting steels. *Engineering Properties of Steel*, 1982.

[13] R. Juvinall and K. Marshek. *Fundamentals of Machine Component Design.* John Wiley & Sons, 3rd edition, 2000.

[14] Brookhaven National Laboratory. Conducting-insulating materials reveal their secrets. News Release 02-44, Brookhaven National Laboratory, 5 June 2002.

[15] D. R. Lide. *CRC Handbook of Chemistry and Physics.* CRC Press, Boca Raton, Florida, 85th edition, 2004.

[16] D. D. Lisowski, S. M. Albiston, A. Tokuhiro, M. H. Anderson, and M. L. Corradini. Results from a scaled reactor cavity cooling system with water at steady state. In *2012 Proceedings of International Congress on Advances in Nuclear Power Plants*, Chicago, Illinois, June 24–28 2012. American Nuclear Society, La Grange Park, Illinois.

[17] A. Maragh, M. J. Minck, and C. W. Forsberg. Preventing large radionuclide releases during severe accidents in fluoride-salt-cooled high-temperature reactors. In *2012 American Nuclear Society Annual Meeting Transactions*, volume 107, pages 904–906, San Diego, California, November 11-15 2012. American Nuclear Society, La Grange Park, Illinois.

[18] E. Megyesy. *Pressure Vessel Handbook.* Pressure Vessel Publishing, Tulsa, Oklahoma, 12th edition, 2001.

[19] M. Mikheyev. *Fundamentals of Heat Transfer.* Peace Publishers, Unknown Year. Translated from Russian and Printed in the USSR.

[20] D. Moss. *Pressure Vessel Design Manual.* Gulf Professional Publishing, Boston, Massachusetts, 3rd edition, 2004.

[21] L. H. Norris and W. C. Reynolds. Turbulent channel flow with a moving wavy boundary. Technical Report FM-10, Stanford University Department of Mechanical Engineering, 1975.

[22] Omega. Emissivity of common materials. "http://www.omega.com/literature/transactions/volume1/emissivitya.html, 17 August 2013.

[23] K. R. Rao. *Companion Guide to the ASME Boiler & Pressure Vessel Code.* ASME Press, New York, New York, 3rd edition, 2009.

[24] W. Ren, G. Muralidharan, D. F. Wilson, and D. E. Holcomb. Considerations of alloy n for fluoride salt-cooled high-temperature reactor applications. In *ASME 2011 Pressure Vessels and Piping Conference*, Baltimore, Maryland, July 17–21 2011. American Society of Mechanical Engineers.

[25] J. Richard, M. P. Short, S. Don, R. R. Romatoski, L.W. Hu, and Forsberg C. W. Preliminary design of a prismatic core fluoride salt-cooled high temperature test reactor (fhtr). In *2013 Proceedings of International Congress on Advances in Nuclear Power Plants*, Jeju Island, Korea, 14–18 April 2013. American Nuclear Society.

[26] M. P. Short, R. G. Ballinger, and C. Forsberg. Bi-metallic composites to raise peak temperatures of the fluoride-salt-cooled high-temperature reactor (FHR). In *2013 Transactions of the American Nuclear Society*, volume 108, pages 350–352, Atlanta, Georgia, 16–20 June 2013. American Nuclear Society.

[27] A. H. Slocum, D. S. Codd, J. Buongiorno, C. Forsberg, T. McKrell, J. Nave, C. Papanicolas, A. Ghobeity, C. J. Noone, S. Passerini, F. Rojas, and A. Mitsos. Concentrated solar power on demand. *Solar Energy*, 85:1519–1529, 2011.

[28] M. Takamatsu, T. Sekine, T. Aoyama, M. Uchida, and S. Kotake. Demonstration of control rod holding stability of the self-actuated shutdown system in joyo for enhancement of fast reactor inherent safety. *Journal of Nuclear Science and Technology*, 44(3):511–517, 2007.

[29] N. E. Todreas and M. S. Kazimi. *Nuclear Systems.* CRC Press, 2nd edition, 2012.

[30] D. P. Williams. Assessment of candidate molten salt coolants for the ngnp/nhi heat-transfer loop. 2006/69, Oak Ridge National Laboratory, June 2006.

[31] M. Wolfstein. The velocity and temperature distribution in one-dimensional flow with turbulence augmentation and pressure gradient. *International Journal of Heat and Mass Transfer*, 12:301–318, 1969.

[32] W. Xu, Q. Chen, and F. T. M. Nieuwstadt. A new turbulence model for near-wall natural convection. *International Journal of Heat and Mass Transfer*, 41:3161–3176, 1998.

[33] D. G. Zill and M. R. Cullen. *Differential Equations with Boundary-Value Problems.* Brooks/Cole, United States, 5th edition, 2001.